REPORT DOCUMENTATION PAGE

Form Approved
OMB No. 0704-0188

Public reporting burden for this collection of information is estimated to average 1 hour per response, including the time for reviewing instructions, searching existing data sources, gathering and maintaining the data needed, and completing and reviewing the collection of information. Send comments regarding this burden estimate or any other aspect of this collection of information, including suggestions for reducing this burden, to Washington Headquarters Services, Directorate for Information Operations and Reports, 1215 Jefferson Davis Highway, Suite 1204, Arlington, VA 22202-4302, and to the Office of Management and Budget, Paperwork Reduction Project (0704-0188), Washington, DC 20503.

1. AGENCY USE ONLY *(Leave blank)*

2. REPORT DATE
25.Jun.02

3. REPORT TYPE AND DATES COVERED
THESIS

4. TITLE AND SUBTITLE
BEAM-FILLING CORRECTION VARIABILITY IN EMISSION BASED PASSIVE MICROWAVE RAINFALL RETRIEVALS

5. FUNDING NUMBERS

6. AUTHOR(S)
CAPT POYNER PHILIP D

7. PERFORMING ORGANIZATION NAME(S) AND ADDRESS(ES)
COLORADO STATE UNIVERSITY

8. PERFORMING ORGANIZATION REPORT NUMBER
CI02-143

9. SPONSORING/MONITORING AGENCY NAME(S) AND ADDRESS(ES)
THE DEPARTMENT OF THE AIR FORCE
AFIT/CIA, BLDG 125
2950 P STREET
WPAFB OH 45433

10. SPONSORING/MONITORING AGENCY REPORT NUMBER

11. SUPPLEMENTARY NOTES

12a. DISTRIBUTION AVAILABILITY STATEMENT
Unlimited distribution
In Accordance With AFI 35-205/AFIT Sup 1

12b. DISTRIBUTION CODE

13. ABSTRACT *(Maximum 200 words)*

20020702 032

14. SUBJECT TERMS

15. NUMBER OF PAGES
99

16. PRICE CODE

17. SECURITY CLASSIFICATION OF REPORT

18. SECURITY CLASSIFICATION OF THIS PAGE

19. SECURITY CLASSIFICATION OF ABSTRACT

20. LIMITATION OF ABSTRACT

COLORADO STATE UNIVERSITY

May 17, 2002

WE HEREBY RECOMMEND THAT THE THESIS PREPARED UNDER OUR SUPERVISION BY PHILIP D. POYNER ENTITLED BEAM-FILLING CORRECTION VARIABILITY IN EMISSION-BASED PASSIVE MICROWAVE RAINFALL RETRIEVALS BE ACCEPTED AS FULFILLING IN PART REQUIREMENTS FOR THE DEGREE OF MASTER OF SCIENCE.

Committee on Graduate Work

Advisor

Department Head

Thesis

Beam-Filling Correction Variability in Emission-Based Passive Microwave Rainfall Retrievals

Submitted by

Philip D. Poyner

Department of Atmospheric Science

In partial fulfillment of the requirements

for the degree of Master of Science

Colorado State University

Fort Collins, Colorado

Summer 2002

Abstract

Beam-Filling Correction Variability in Emission-Based Passive Microwave Rainfall Retrievals

With the threat of global warming looming over the world's population, it is of paramount importance that both the cause and effect of this phenomenon be identified correctly. Global Climate Models (GCMs) attempt to predict the future, so validating the physical assumptions in these models becomes critical. However, it has been found that these models disagree with current observations, particularly those related to global precipitation variability. Without a proper prediction of that variability, its contribution to the energy balance (through the release of latent heat) will not be correctly accounted for. This contribution would then be improperly attributed to some other component of the energy cycle, diminishing our ability to establish cause and effect.

An additional problem exists in that validation of the hydrological cycle in GCMs is accomplished using primarily space-borne passive microwave sensor observations. Rainfall retrievals from those sensors suffer from their own inaccuracies, and the question must be posed as to whether the observations are correct and the GCMs wrong, or visa versa. One of the major sources of error in the observations is the so-called

beam-filling error, caused by variations in rainfall inhomogeneity within the relatively coarse resolutions of today's sensors. Due to past limitations in information about rainfall inhomogeneity, the correction for this error has been set as a constant in rainfall retrievals. Information from the recently launched Tropical Rainfall Measuring Mission Precipitation Radar makes it possible to map global beam-filling corrections in a more realistic manner. This study shows that this correction is not a constant, as previously assumed, and varies on both a regional and temporal scale.

When the beam-filling correction variability is taken into account, emission-based rainfall algorithms and resulting rainfall estimates should be more accurate. This work has been performed and the rainfall products have been corrected for this source of uncertainty. Results show significant changes in regional rainfall distributions, but little change in the global rainfall variability. As such, the current improvements to the rainfall products eliminate a significant uncertainty, and allow us to have more confidence that discrepancies between GCMs and observations are not due to faulty observations.

Capt. Philip D. Poyner

Department of Atmospheric Science

Colorado State University

Fort Collins, CO, 80523

Summer 2002

Acknowledgements

I would like to thank my advisor, Dr. Kummerow, for his guidance, direction, and support throughout the course of this research. I would also like to thank my other committee members, Dr. Rutledge and Dr. Ramirez, for their advice and for taking the time to serve on my committee.

I would like to express appreciation to the entire Kummerow Research group for their help in bringing together the different aspects of this project. In particular, I would like to thank Dr. Morales for his help with the computer programming, Dr. Shin for his insight into statistics, Dr. Berg for his knowledge of climate variability, and Sean Miner, who always seemed to know the answers to questions I had about coursework. Thanks also to Paul Hein and Walt Petersen, for access to high-resolution radar data and help in getting the information I needed.

Acknowledgement should also be made to the Air Force Institute of Technology's Civilian Institute program, which funded my time here.

Finally, I'd like to thank my wife, [redacted] for all her support, and for believing in me even when I had a hard time doing so myself.

Disclaimer

The views expressed in this article are those of the author and do not reflect the official policy or position of the United States Air Force, Department of Defense, or the United States Government.

Table of Contents

Chapter		Page
1	**Introduction**	1
2	**Space-Based Passive Microwave Sensing and the Beam-Filling Error**	8
	2.1 Historical Perspective	10
	2.2 Algorithm Physical Basis	14
	2.3 Instantaneous Ocean Rainfall Algorithms	24
	2.4 The Beam-Filling Error Described	26
	2.5 Beam-Filling Corrections and the TMI Algorithm	29
3	**Project Description**	31
	3.1 The Eddington Approximation RTE	31
	3.2 The Atmospheric Profile	34
	3.3 Methodology	36
4	**Beam-Filling Correction Climatology**	43
	4.1 Beam-Filling Correction Curves	43
	4.2 Global Beam-Filling Correction Climatology Results	46
5	**Sensitivity Studies**	52
	5.1 Effect of Ice Content on Model Results	52
	5.2 Ability of the 4-km Resolution Data to Capture the Full Rainfall Inhomogeneity	53
6	**Summary and Conclusions**	58
	Bibliography	67
Appendix A	**Monthly Beam-Filling Correction Maps**	70

List of Figures

Figure		Page
1.1	Variations in the Earth's surface temperature.	2
1.2	The energy balance of the Earth and atmosphere system. The incoming solar radiation is taken to be 100 units.	3
1.3	Precipitation patterns during the El Niño of 1997 and La Niña of 1993.	6
2.1	NIMBUS-5.	11
2.2	SSM/I.	12
2.3	TRMM Microwave Imager.	13
2.4	Reflectivity of typical ocean and land surfaces as a function of incidence angle for both horizontal and vertical polarizations.	16
2.5	Global brightness temperature composite from SSM/I 19 GHz, horizontal polarization data on November 7, 1996.	16
2.6	Computed brightness temperatures as a function of rainfall rate for selected frequencies.	20
2.7	Moments of the drop size distribution (F_{RR} and F_{ABS}) and a volume-weighted Marshall Palmer distribution ($D^3N(D)$), $G(\rho)$, for a 10 mm/hr rain rate as a function of the drop diameter.	24
2.8	Homogeneous FOV temperature-rain rate relation (red curve) vs. heterogeneous FOV temperature-rain rate relation (blue dots).	27
2.9	Homogeneous FOV.	27
2.10	Actual heterogeneous FOV with legend.	28
3.1	Rainfall map from TRMM showing the west and east Pacific boxes.	36

4.1	Beam-filling correction to inhomogeneity parameter relationship.	44
4.2	Beam-filling correction as a function of inhomogeneity parameter and rain rate. Lines represent the best polynomial fit to the data.	45
4.3	January-February-March 1998 beam-filling correction (color) and total rainfall in mm (circle size).	47
4.4	April-May-June 1998 beam-filling correction (color) and total rainfall in mm (circle size).	47
4.5	July-August-September 1998bBeam-filling correction (color) and total rainfall in mm (circle size).	47
4.6	October-November-December 1998 beam-filling correction (color) and total rainfall in mm (circle size).	48
4.7	January-February-March 1999 beam-filling correction (color) and total rainfall in mm (circle size).	48
4.8	April-May-June 1999 beam-filling correction (color) and total rainfall in mm (circle size).	48
4.9	July-August-September 1999 beam-filling correction (color) and total rainfall in mm (circle size).	49
4.10	October-November-December 1999 beam-filling correction (color) and total rainfall in mm (circle size).	49
4.11	January-February-March 2000 beam-filling correction (color) and total rainfall in mm (circle size).	49
4.12	April-May-June 2000 beam-filling correction (color) and total rainfall in mm (circle size).	50
4.13	July-August-September 2000 beam-filling correction (color) and total rainfall in mm (circle size).	50
4.14	October-November-December 2000 beam-filling correction (color) and total rainfall in mm (circle size).	50
4.15	January-February-March 2001 beam-filling correction (color) and total rainfall in mm (circle size).	51
5.1	Beam-filling correction to inhomogeneity parameter relationship, with changing ice content.	53

5.2	Correlation between inhomogeneity parameters calculated at high and low resolution for Wallops Island, March and April 2001.	55
5.3	Correlation between inhomogeneity parameters calculated at high and low resolution for Wallops Island, March and April 2001 and TRMM/LBA, January and February 1999.	56
6.1	Relationship between actual beam-filling corrections and over/underestimation of rainfall by TMI vs. PR	60
6.2	Precipitation deviation from the mean (normalized to 3 mm/day).	61
6.3	Precipitation deviation from the mean vs. beam-filling correction deviation from the mean (%).	62
6.4	West Pacific precipitation mean (mm/day).	63
6.5	East Pacific precipitation mean (mm/day).	64
6.6	Beam-filling correction vs. Convective rain fraction for Apr-Jun 1998.	64
A.1	January 1998 beam-filling correction (color) and total rainfall in mm (circle size).	71
A.2	February 1998 beam-filling correction (color) and total rainfall in mm (circle size).	71
A.3	March 1998 beam-filling correction (color) and total rainfall in mm (circle size).	71
A.4	April 1998 beam-filling correction (color) and total rainfall in mm (circle size).	72
A.5	May 1998 beam-filling correction (color) and total rainfall in mm (circle size).	72
A.6	June 1998 beam-filling correction (color) and total rainfall in mm (circle size).	72
A.7	July 1998 beam-filling correction (color) and total rainfall in mm (circle size).	73
A.8	August 1998 beam-filling correction (color) and total rainfall in mm (circle size).	73

A.9 September 1998 beam-filling correction (color) and total rainfall in mm (circle size) 73

A.10 October 1998 beam-filling correction (color) and total rainfall in mm (circle size). 74

A.11 November 1998 beam-filling correction (color) and total rainfall in mm (circle size). 74

A.12 December 1998 beam-filling correction (color) and total rainfall in mm (circle size). 74

A.13 January 1999 beam-filling correction (color) and total rainfall in mm (circle size). 75

A.14 February 1999 beam-filling correction (color) and total rainfall in mm (circle size). 75

A.15 March 1999 beam-filling correction (color) and total rainfall in mm (circle size). 75

A.16 April 1999 beam-filling correction (color) and total rainfall in mm (circle size). 76

A.17 May 1999 beam-filling correction (color) and total rainfall in mm (circle size). 76

A.18 June 1999 beam-filling correction (color) and total rainfall in mm (circle size). 76

A.19 July 1999 beam-filling correction (color) and total rainfall in mm (circle size) 77

A.20 August 1999 beam-filling correction (color) and total rainfall in mm (circle size). 77

A.21 September 1999 beam-filling correction (color) and total rainfall in mm (circle size). 77

A.22 October 1999 beam-filling correction (color) and total rainfall in mm (circle size). 78

A.23 November 1999 beam-filling correction (color) and total rainfall in mm (circle size). 78

A.24 December 1999 beam-filling correction (color) and total rainfall in mm (circle size). 78

A.25 January 2000 beam-filling correction (color) and total rainfall in mm (circle size). 79

A.26 February 2000 beam-filling correction (color) and total rainfall in mm (circle size). 79

A.27 March 2000 beam-filling correction (color) and total rainfall in mm (circle size). 79

A.28 April 2000 beam-filling correction (color) and total rainfall in mm (circle size). 80

A.29 May 2000 beam-filling correction (color) and total rainfall in mm (circle size). 80

A.30 June 2000 beam-filling correction (color) and total rainfall in mm (circle size). 80

A.31 July 2000 beam-filling correction (color) and total rainfall in mm (circle size). 81

A.32 August 2000 beam-filling correction (color) and total rainfall in mm (circle size). 81

A.33 September 2000 beam-filling correction (color) and total rainfall in mm (circle size). 81

A.34 October 2000 beam-filling correction (color) and total rainfall in mm (circle size). 82

A.35 November 2000 beam-filling correction (color) and total rainfall in mm (circle size). 82

A.36 December 2000 beam-filling correction (color) and total rainfall in mm (circle size). 82

A.37 January 2001 beam-filling correction (color) and total rainfall in mm (circle size). 83

A.38 February 2001 beam-filling correction (color) and total rainfall in mm (circle size). 83

A.39 March 2001 beam-filling correction (color) and total rainfall in mm (circle size). 83

A.40 April 2001 beam-filling correction (color) and total rainfall in mm (circle size). 84

A.41 May 2001 beam-filling correction (color) and total rainfall in mm (circle size). 84

A.42 June 2001 beam-filling correction (color) and total rainfall in mm (circle size). 84

A.43 July 2001 beam-filling correction (color) and total rainfall in mm (circle size). 85

A.44 August 2001 beam-filling correction (color) and total rainfall in mm (circle size). 85

List of Tables

Table		Page
3.1	Beam-filling corrections (0-6 mm/hr).	38
3.2	Beam-filling corrections (6-13 mm/hr).	39
3.3	Beam-filling corrections (13-20 mm/hr).	39
3.4	Beam-filling corrections (20-27 mm/hr).	40
3.5	Beam-filling corrections (27-34 mm/hr).	40
3.6	Beam-filling corrections (34-41 mm/hr).	41
3.7	Beam-filling corrections (41-48 mm/hr).	41
3.8	Beam-filling corrections (48-55 mm/hr).	42
3.9	Beam-filling corrections (55-60 mm/hr).	42

Chapter 1

Introduction

Considerable attention has recently been focused on questions related to "global warming"; what are its causes, which of those causes are anthropogenic in nature, and how will it affect our future here on Earth? Since the mid-1970's the temperature of the Earth's surface has been rising, as can be seen in Figure 1.1 (IPCC Report, 2001). However, the question still remains unanswered as to whether this warming is due to natural climate variability or as the result of a cause and effect relationship with increasing CO_2. In a dry atmosphere, increasing CO_2 levels would lead to global warming. The Earth's hydrologic cycle tends to make this conclusion less certain. Water vapor is thought to increase with warmer temperatures, and that could lead to an enhanced greenhouse effect. On the other hand, the formation of clouds would reflect larger amounts of the incoming solar radiation back to space, which in turn would lead to planetary cooling.

In order to determine whether anthropogenic sources are the cause of surface warming in any sort of definitive way, Global Climate Models must be used and their results verified. A simple way to do this is to initialize the model some time in the past,

increase the carbon dioxide concurrent with observed increases, and see how well it predicts the current atmospheric parameters. If the model as a result of the CO_2 increase correctly predicts atmospheric parameters as they are observed, then global warming could be linked directly to carbon dioxide increases. If not, then the problem requires more study.

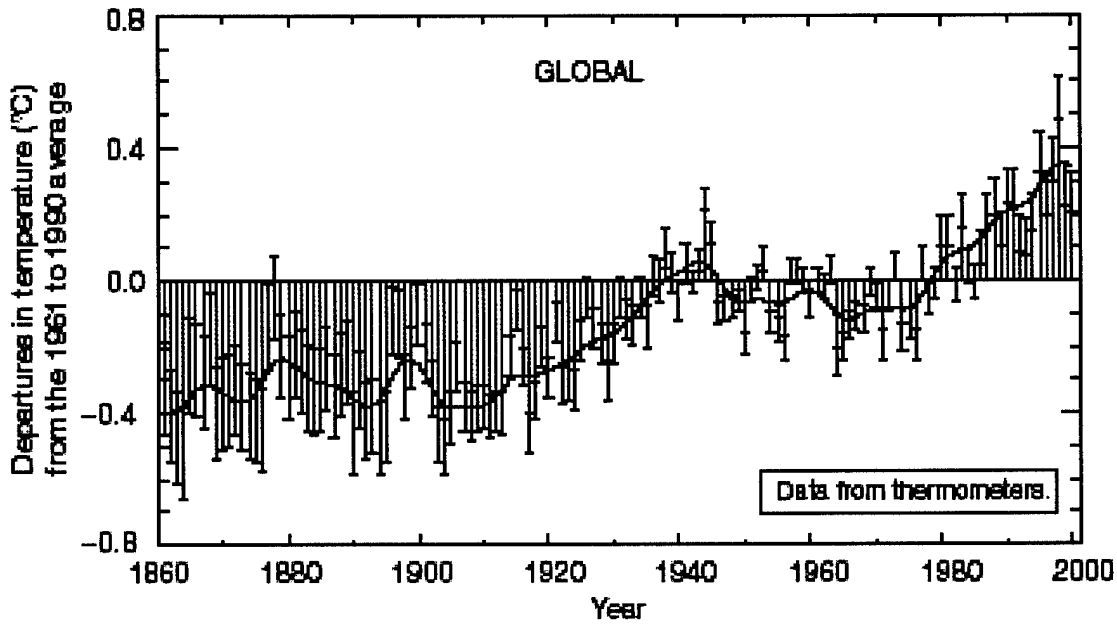

Figure 1.1: Variations in the Earth's surface temperature.

Until recently, the predictive variable of interest has been surface temperature. The ability of these models to reproduce the temperature curve seen in Figure 1.1 has increased confidence in their accuracy. However, correct prediction of surface temperature is not enough. Figure 1.2 shows that there are many components to the energy balance that can affect the surface temperature. These must also be accounted for, as the components must balance in order to keep the net energy fluxes in equilibrium.

The left-hand side of the figure shows the contribution due to solar radiation (short-wave radiation), while the right-hand side shows the transfer of energy from the surface and within the atmosphere (long-wave radiation). The surface temperature is determined by the amount of net flux that is received at the surface. An increase in the net flux can come from changes in incoming solar radiation, changes in the downward flux of long-wave radiation from the atmosphere or from changes in latent and sensible heating. Flux calculations show that without latent heating, the atmosphere would be cooling at a rate of 2° Celsius per day (with a concurrent heating of the surface). In order to establish cause and effect through a Global Climate Model (GCM), it is not enough to just predict temperature accurately. Precipitation must be predicted correctly as well.

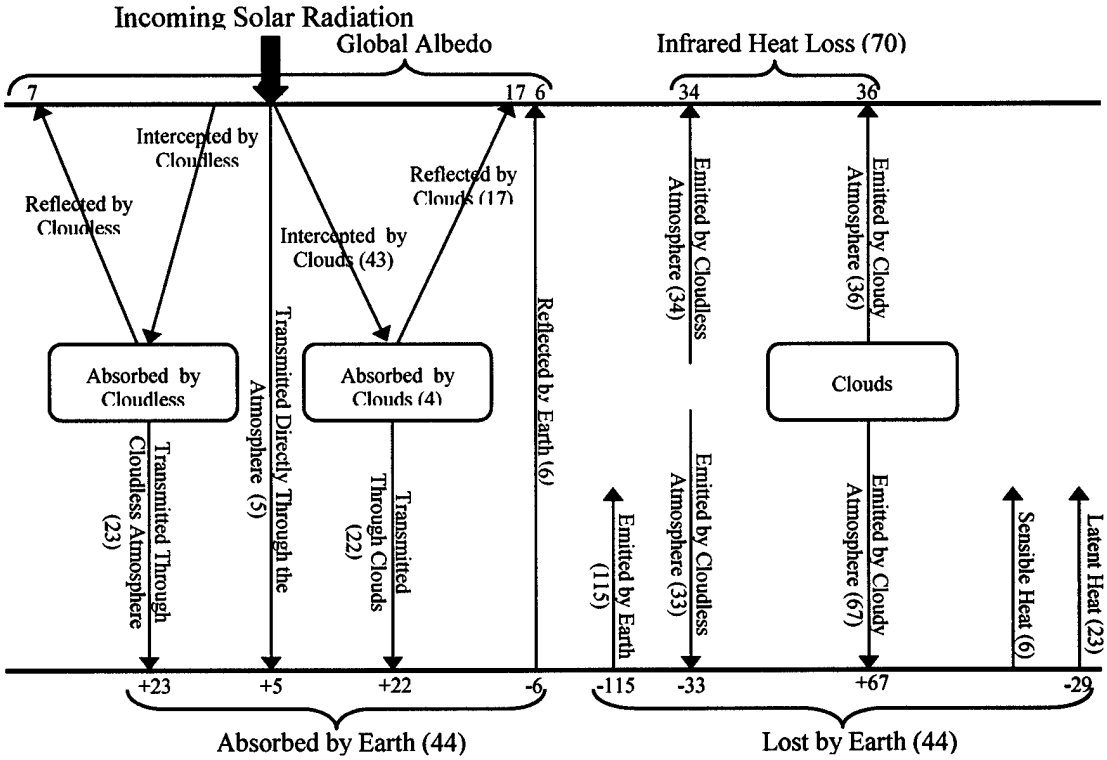

Figure 1.2: The energy balance of the Earth and atmosphere system. The incoming solar radiation is taken to be 100 units.

Recent studies by Soden, 2000, have led to the conclusion that GCMs poorly predict rainfall variability, which is the deviation from the mean rain rate. While surface temperatures, outgoing long-wave radiation and water vapor were predicted accurately by the models in that study, precipitation and the downward flux of long-wave radiation were not. Interannual variability of the observed rainfall in that study was approximately 10% of the global mean, while the models showed only 1-2% variability. The study led to the conclusion that either GCMs perform poorly (in which case they must be improved), or current observations are not accurate enough to properly quantify rainfall variability. If the former is true, then GCMs predictions of other components of the energy balance are likely to be poor, and the physical processes within these GCMs must be improved before cause and effect conclusions can be drawn.

Some components in the energy budget shown in Figure 1.2 are easily measured, while some are not. Incoming solar and outgoing long wave radiation, for instance, is well known from satellite data. We can accurately measure atmospheric constituents that impact the energy balance, such as temperature and water vapor. However, other parts of the radiation budget are more difficult to measure and are potential sources of error. Amongst those are the measurements of downward long-wave energy flux and latent heating. Latent heating occurs when atmospheric water changes phase, specifically from vapor to liquid. As the condensation and precipitation processes occur, heat is released into the atmosphere. Latent heating is impossible to measure directly, but the net condensation is equal to the amount of rain occurring, and that rain can be measured. Variations in latent heating are therefore directly related to variations in the global precipitation.

This immediately leads to the problem of how accurately the rainfall component of the energy balance can be measured, and how much confidence we have in those observations.

Measurements of latent heating are valuable for reasons beyond their contributions to our understanding of the Earth's energy budget. Large-scale rainfall patterns and their associated latent heat release in the Tropics affect global circulation, as can be seen during El Niño and La Niña events (Figure 1.3). Even if the energy budget were not a concern, accurate measurements of rainfall are still needed. Rainfall variability has an effect on the biosphere, including humans. Patterns of drought alternating with periods of flooding may cause problems in industrial nations, but they can be devastating to developing countries. So, the knowledge of rainfall patterns and rainfall amounts are not only important in the scientific arena, but are also important to those concerned with making socio-political policy decisions. Policy makers require those variations not only be properly observed but also, as stated earlier, properly predicted by GCMs.

The focus of this study is on the issue of rainfall inhomogeneity within the passive microwave sensors field-of-view, which is the largest source of uncertainty in passive microwave retrievals. This inhomogeneity is the result of variations in atmospheric instability, moisture content, and forcing (which produces the lift that cools the moisture to the point of condensation) across an area of interest. Areas of high instability and strong forcing will tend to produce convective clouds, with greater rainfall intensities, while areas of low instability and weak forcing tend to produce stratiform clouds, with uniform weak intensities. While details are covered in Chapter 2, inhomogeneity at the sub-resolution level causes a retrieval to underestimate rainfall rates. This error is

commonly referred to as the beam-filling error. In order to compensate for this error, retrieval schemes apply a beam-filling correction. Unfortunately, current retrievals apply the same correction across the entire globe, which would assume a common inhomogeneity. Unless inhomogeneity is a highly universal quantity, this would tend to cause either an under- or overestimation of rain rates, depending on where that correction was applied. Use of this technique was driven primarily by a lack of data available that

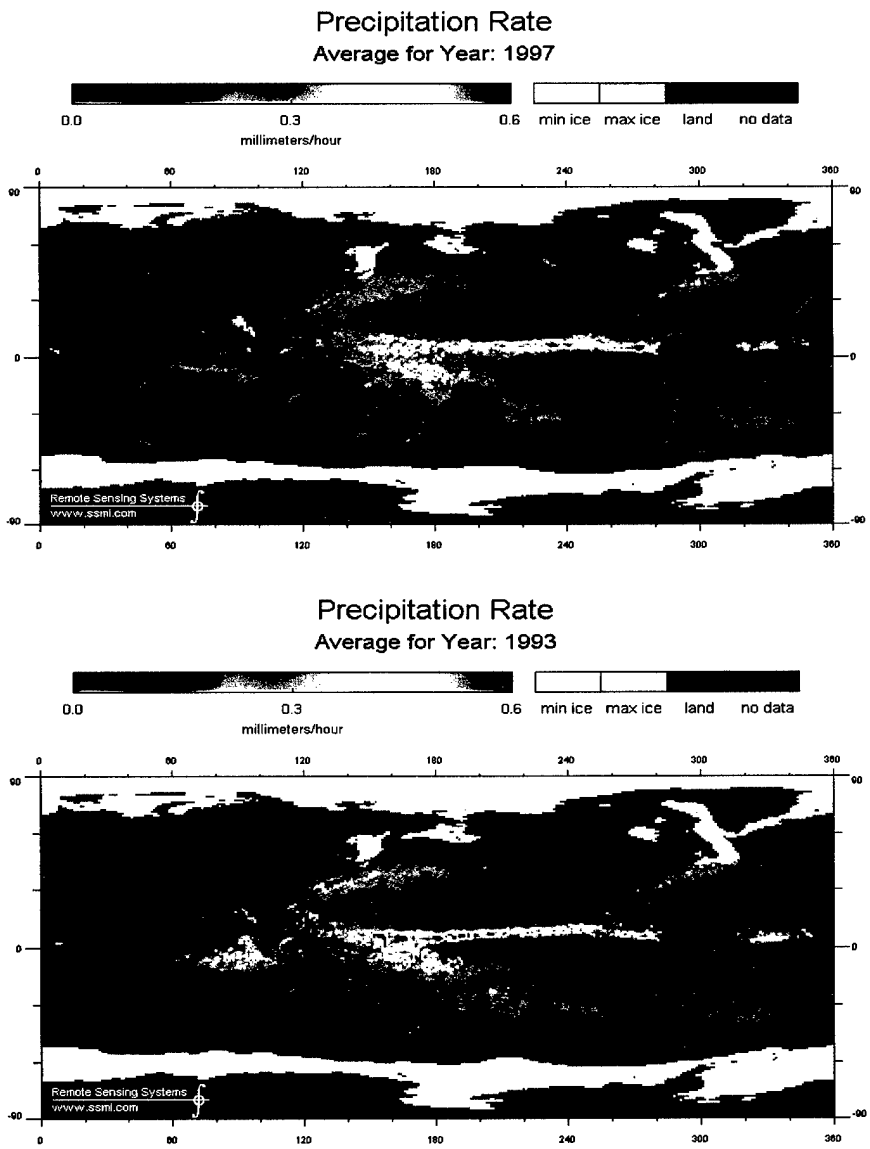

Figure 1.3: Precipitation patterns during the El Niño of 1997 and La Niña of 1993.

would allow for anything else, but with the advent of high-resolution space-borne radar we have the data to estimate better correction factors. If inhomogeneities could be determined globally, and if a correction could be determined for each level of inhomogeneity and mean rain rate, a climatology of beam-filling corrections could be developed. This climatogy could be used during post-analysis to produce rainfall estimates without these biases and thus closer to reality than those currently available. Once those new rainfall rates were developed, a more realistic measure of latent heating would naturally follow.

In the following chapters, new and more accurate beam-filling corrections will be presented, which will compensate for the effects of field-of-view inhomogeneity on rainfall retrievals. Chapter 2 begins with an overview of the beam-filling error, including a description of the error and a brief history of rainfall retrieval from passive microwave sensors. The method by which the error is dealt with today and the problems stemming from using current methods follows from that. In Chapter 3, the project is described and details are provided regarding the tools used and procedures taken in the actual computation of the beam-filling correction. Chapter 4 shows the resulting relationship between rainfall inhomogeneity and beam-filling correction, and presents monthly maps of beam-filling corrections from January 1998 through August 2001. A brief sensitivity study is included in Chapter 5, where the effects of changes in ice content on the results at the 19 GHz channel and the ability of the resolution of the 4-km radar data to properly account for all inhomogeneity at sub-resolution scales will be shown. Finally, conclusions are presented and their implications on observed rainfall and latent heating variability is discussed.

Chapter 2

Space-Based Passive Microwave Sensing and the Beam-Filling Error

Since the invention of weather radar and through the 1960s only two rainfall measuring methods were available, neither of which produced the quality or coverage of data needed. A global meso-network of rain gauges would have been cost prohibitive, politically unrealistic, subject to measurement errors, and still wouldn't have measured rainfall over the oceans. A global surface radar network would have suffered from the same problems and would also have required a calibration standard that seems impossible to achieve even today. The advent of space-based sensors provided the only realistic way of tackling these problems. Infrared (IR) sensors were the first used, but could only view cloud top. IR sensors were followed by microwave radiometers, which could penetrate through the entire depth of the rain cloud. Radar was launched by the National Aeronautics and Space Administration (NASA) in 1997, but there was not enough data from it to produce the rainfall baseline needed, and radar retrievals themselves contained uncertainties. This left passive microwave retrievals as the most workable method of measuring rainfall on a global scale.

A passive microwave sensor's ability to measure rainfall depends on the strong emission of liquid drops, which offers a strong contrast to radiometrically cold ocean surfaces at these wavelengths (Wilheit, *et al.*, 1977). Passive microwave retrievals are a significant step forward from previous infrared rainfall measurement techniques, which use empirical relationships between cloud top properties and rainfall to produce their rainfall estimates. Some IR techniques relate cloud cover and type to rain rate. Others relate reflected solar brightness to rain rates. The most successful IR scheme relates cloud top temperatures to areas of large radar echoes. Current microwave physical models, on the other hand, produce a retrieved rainfall derived from a theoretical relationship between brightness temperature and rain rate based on detailed cloud property assumptions (Kummerow, 1998). Each one of these properties can be isolated and their effect on the retrieval and retrieval error can be tested more easily than empirically derived brightness temperature to rainfall rate relations.

Rainfall measurements from passive microwave sensors do come with their own set of problems, most related to the previously mentioned cloud property assumptions. The radiative-transfer models that relate rainfall to observed microwave radiances, for instance, produce poor results if the cloud properties are poorly described or accounted for. Amongst these properties are the drop-size distribution, the height of the freezing level and its effect on the ice particle distribution, ice particle shape and size, and the amount of rainfall inhomogeneity within the sensor's field-of-view.

2.1 Historical Perspective

Microwave rainfall estimation development advanced along lines laid out well before algorithms reached maturity, something it has in common with many developments in satellite remote sensing of the atmosphere. Early retrieval techniques operated on the assumption that a single parameter could be derived directly from a visible (VIS) or infrared (IR) satellite channel, and then used to estimate a single rainfall parameter related to rain rate or rain accumulation. Such a view prevailed since the VIS and IR channels could only describe the appearance or temperature of the cloud top, and the penetrating spectral channels in the centimeter-millimeter microwave spectrum were not yet available. Rainfall estimation tended to be viewed as a problem in transforming a single input VIS or IR measurement to a single rainfall parameter. Because this VIS-IR heritage, and because the first microwave radiometers were single frequency instruments, the first passive microwave retrieval algorithms continued along the lines of the VIS-IR techniques. The first radiometer, Nimbus 5's (Figure 2.1) Electrically Scanning Microwave Radiometer (ESMR-5), received radiation emitted by earth and its atmosphere in a 250 MHz bandwidth centered at 19.35 GHz (Wilheit, *et al.*, 1977). It had a spatial resolution of 25 km at nadir and scanned a swath of 2500 km from a 1100-km near-polar sun-synchronous orbit. Using this sensor (or data from the later ESMR-6 with it's 37 GHz channel), early algorithms proposed by Wilheit *et al.* (1977), Weinman and Guetter (1977), Rodgers *et al.* (1979), and Jung (1980) were designed to estimate a single rainfall parameter from a single spectral measurement through idealized brightness temperature-rain rate relationships.

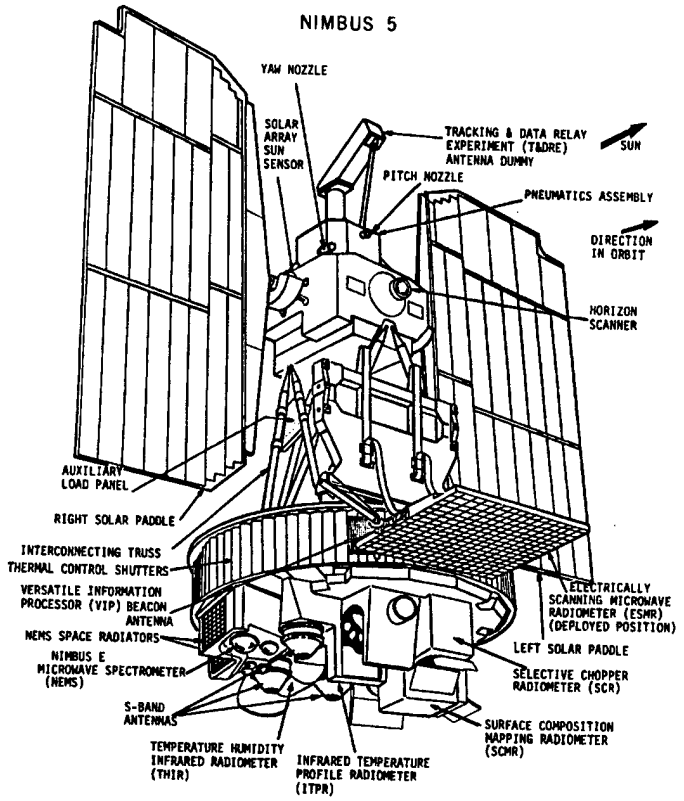

Figure 2.1: NIMBUS-5.

The first passive microwave radiometer capable of measuring more than one frequency was the Nimbus 7 Scanning Multichannel Microwave Radiometer (SMMR) launched in 1987. With this instrument, a new class of multichannel algorithms could be developed in which different frequencies could detect rain and ice concentrations at different levels within a precipitating cloud. This created the possibility for inversion-type schemes designed to retrieve some type of vector describing the rain profile. In reality, only the study by Olson (1989), well after SMMR was launched, was directly aimed at exploiting the multifrequency SMMR information in a rainfall retrieval algorithm. A study by Kummerow *et al.* (1989) focused on wider applications, but was limited to an examination of aircraft measurements. Not until Special Sensor Microwave

Imager (SSM/I) (Figure 2.2) measurements obtained from the Defense Meteorological Satellite Program (DMSP) platforms became available (Hollinger *et al.*, 1990), were true multifrequency precipitation retrievals developed (Smith *et al.,* 1994; Mugnai *et al.,* 1993; Kummerow and Giglio, 1994). This sensor measured frequencies at 19.35, 22.235, 37, and 85.5 GHz. The spatial resolution varied from 69 X 43 km at 19.35 GHz to 15 X 13 km at 85.5 GHz. A swath width of 1400 km is scanned from an 833-km sun-synchronous orbit.

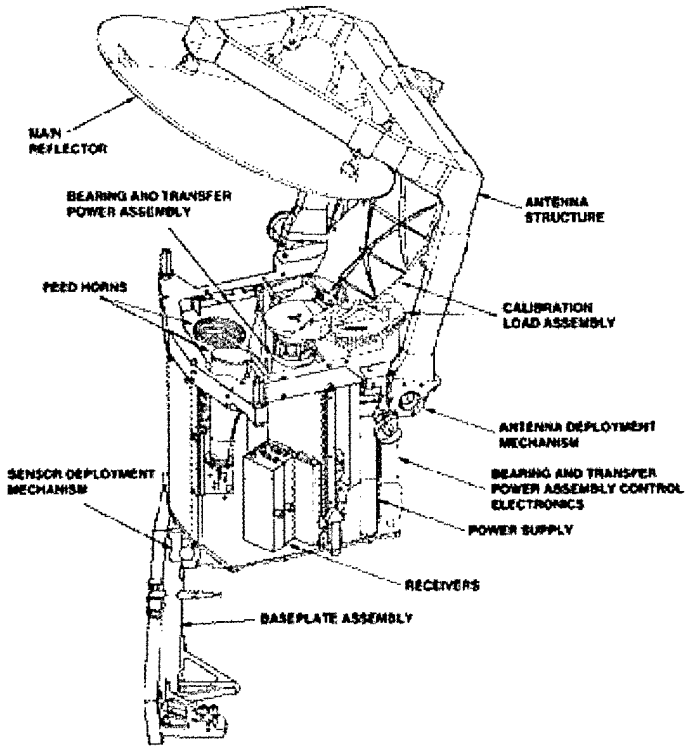

Figure 2.2: SSM/I.

The Tropical Rainfall Measuring Mission (TRMM) was launched in 1997. On board it carried a passive microwave radiometer very similar to SSM/I, the TRMM Microwave Imager (TMI) (Figure 2.3). It measures the same frequencies as SSM/I, with the addition

of a 10.65 GHz frequency. In addition, it carried the Precipitation Radar (PR) that provides an independent means to verify rainfall measured by the TMI. It is data from TMI and PR that were used in this study (specifically data from the horizontally polarized 19 GHz channel). One of the advantages TMI data have over similar data from SSM/I stems simply from the fact that TRMM flies at 350 km, as opposed to DMSP, which is at 833 km. Observed objects must be physically separated at least one beamwidth to be resolved individually, which is what defines resolution. Although the beamwidths of SSM/I and TMI are virtually the same in degrees, the scan geometry resulting from a lower altitude ensures that the physical area covered by the beam is smaller with TMI than SSM/I. This leads to a higher resolution. Due to its lower altitude TMI resolutions vary from 63 km X 37 km at 10.65 GHz to 7 km X 5 km at 85.5 GHz. Having both the PR and TMI sensors on the same platform has led to further study of the assumptions contained in the PR and TMI retrievals, given the fact that the sensors have produced different rainfall totals for a given location and time.

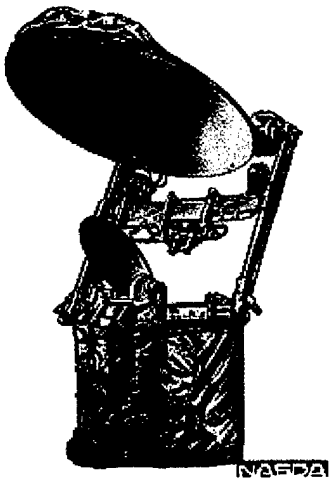

Figure 2.3: TRMM Microwave Imager.

2.2 Algorithm Physical Basis

Radiative transfer theory forms the basis of passive microwave remote sensing techniques. In an atmosphere that is absorbing and/or scattering microwave radiation, the radiance is determined by the Equation of Radiative Transfer (RTE) (Chandrashekar, 1960), which can be written as:

$$\frac{dI(\theta,\phi)}{ds} = A + S \tag{2.1}$$

where: $A = k_{abs}\{B_\lambda(T) - I(\theta,\phi)\}$ and $S = k_{sca}\{\int P(\theta,\phi;\theta',\phi')I(\theta,\phi')d\Omega' - I(\theta,\phi)\}$, $I((\theta,\phi)$ is the radiance in the direction specified by the polar angles, θ and ϕ, s is distance in the θ, ϕ direction, k_{abs} is the absorption coefficient and k_{sca} is the scattering coefficient. $P(\theta,\phi;\theta',\phi')$, the phase function, shows the probability of scattering from a direction specified by θ', ϕ' to a direction θ, ϕ.

When the RTE is organized this way absorption and emission are represented by the term A. The loss of radiance due to scattering out of the beam and the gain of radiance due to the scattering of diffuse radiance travelling in other directions into the beam, with no net change in the total radiation, are represented by the term S.

The long wavelengths of microwave radiation allows for the use of the Rayleigh-Jeans approximation, $B(\lambda,T) \propto \lambda^{-4}T$, which defines a brightness temperature, Tb, accordingly. The RTE can then be rewritten as:

$$\frac{dTb(\theta,\phi)}{ds} = A_{RJ} + S_{RJ} \tag{2.2}$$

where: $A_{RJ} = k_{abs}\{T - Tb(\theta,\phi)\}$ and $S_{RJ} = k_{sca}\{\int P(\theta,\phi;\theta',\phi')Tb(\theta',\phi')d\Omega' - Tb(\theta,\phi)\}$.

If there were no scattering, the RTE could be directly integrated. However, when scattering is introduced, the problem becomes more difficult to solve. Upon study of the scattering term in Eqns. (2.1) and (2.2), it can be seen that computing the radiance at any one angle requires knowledge of the radiance at every angle. This study will make use of the Eddington approximation developed by Kummerow (1993). Kummerow showed that errors of these approximations at microwave frequencies are commonly only about a few degrees Kelvin. Reverse Monte Carlo methods, which require more computing capacity, are also available to solve three-dimensional radiative transfer problems at microwave frequencies (Roberti *et al.*, 1994).

The radiance, or brightness temperature (Tb), measured by the satellite depends upon the radiance emitted by the surface as well as the downwelling radiance reflected from the surface. At a given wavelength (Chandrashekar, 1960), if a radiance, I, is incident on a surface with a reflectivity, r, and a temperature Ts, the radiance of the reflected beam, $I_\lambda(0)$ is given by:

$$I_\lambda(0) = r\, I_\lambda(0) + \varepsilon B_\lambda(Ts) \tag{2.3}$$

where $B_\lambda(Ts)$ is the blackbody radiance (Planck function) for a wavelength, λ, and a temperature Ts. ε is the emissivity of the surface. The emissivity and the reflectivity of the surface (the Second Law of Thermodynamics requires that $r + \varepsilon = 1$) are described by the Fresnel relations, (Jackson, 1962), as determined by the view angle, the polarization and the complex index of refraction of the surface matter. Emissivity is low for oceans and high for land areas.

In Figure 2.4, typical emissivities for ocean and land regions are depicted. For both regions the upper curve is for the horizontal polarization and the lower for vertical

polarization. A typical land area is computed for complex index of refraction of 2 + 0.1i, which assumes a moderately dry soil. For this study, ocean regions are computed for a 19.35 GHz frequency and a 298 K temperature. The considerable difference in reflectivities between land and ocean is what makes land areas so obvious in Figure 2.5.

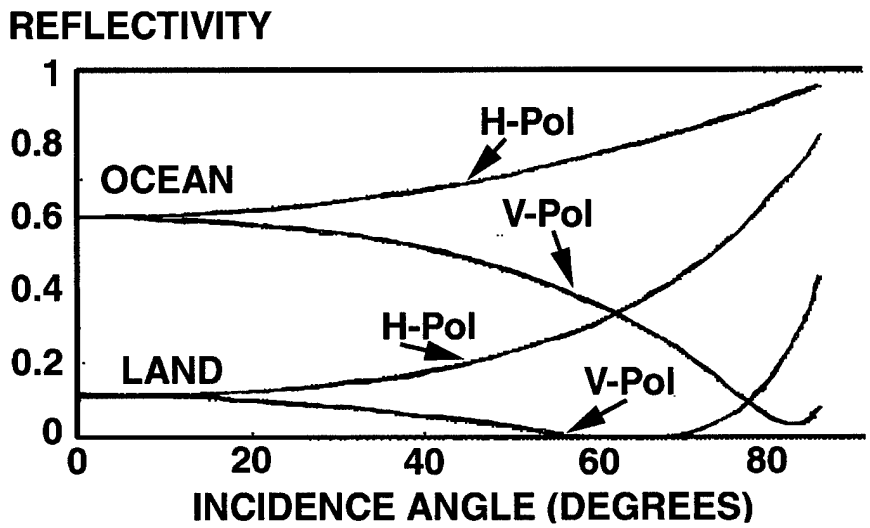

Figure 2.4: Reflectivity of typical ocean and land surfaces as a function of incidence angle for both horizontal and vertical polarizations.

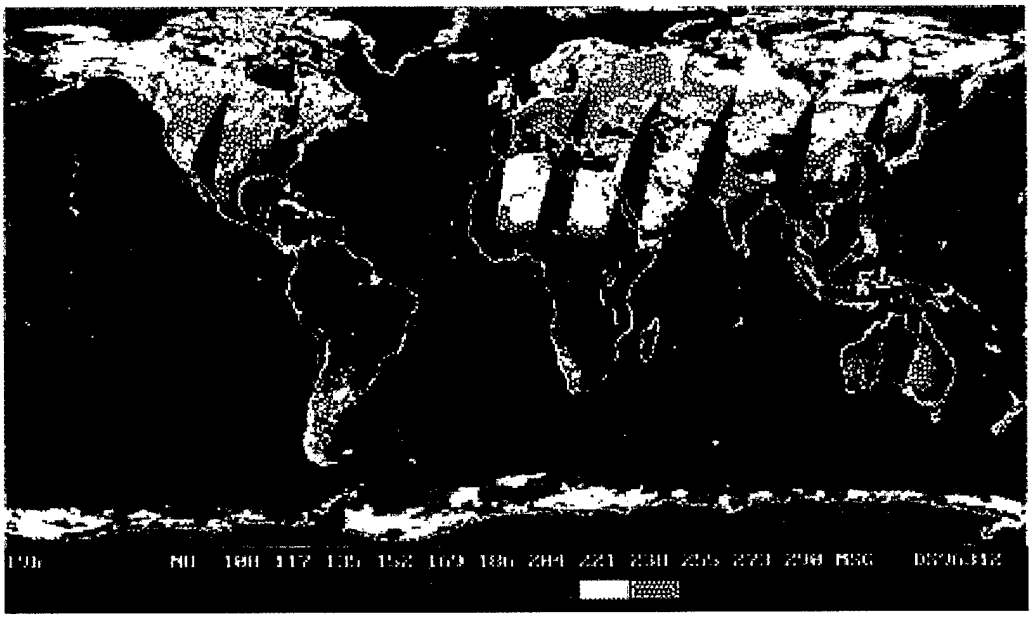

Figure 2.5: Global brightness temperature composite from SSM/I 19 GHz, horizontal polarization data on November 7, 1996.

Although everything written to this point provides details of the solution to the RTE, it may be useful to gain a feel into the behavior of the solutions. The simplest solution to conceptualize is the "Reverse Monte-Carlo" solution, and thus it will be used here. Picture the radiometer as a transmitter sending photons into the atmosphere of which you wish to compute the brightness temperature. As each photon passes through the atmosphere, it has a probability of being absorbed or scattered and, if scattered, a probability distribution of angles. A random number generator can be used to decide what happens to the photon in accordance with these probabilities as it travels through each increment of the atmosphere. Quite a number of photons are tracked from the transmitter into the atmosphere until they are absorbed. The atmospheric temperature at the point of absorption is determined and averaged for all the photons. With scattering, there is some probability that photons will scatter out of the atmosphere and into space. This is equivalent to being absorbed by the 2.7 K cosmic background. Using a generalization of Kirchoff's law, the average temperature where the protons are absorbed should be the brightness temperature that a radiometer would observe.

Three atmospheric constituents in the troposphere act as important absorbers: water vapor, liquid water and molecular oxygen. Frequencies where absorption due to molecular oxygen is important (roughly 50 to 70 GHz and near 119 GHz) are used for temperature sounding as oxygen is well distributed in the atmosphere. In rainfall retrievals, which operate at frequencies well removed from the oxygen absorption lines, absorption due to molecular oxygen is therefore a minor correction that needs to be quantitatively correct, but is not necessary for this conceptual understanding.

Nonprecipitating cloud particles are approximately 50 μm or less in diameter, and thus much smaller than the wavelength of microwave radiation (about 1 mm). Therefore, the Rayleigh approximation (Gunn and East, 1954) can be used. The absorption coefficient is then proportional to the diameter cubed, and the scattering coefficient is so small in comparison that it can be neglected. With the absorption coefficient being proportional to the cube of the diameter, it is also proportional to the volume and mass of the drops. The microwave absorption coefficient of a cloud will therefore be proportional to the mass density of the water contained in that cloud, independent of the size distribution of the droplets.

Raining clouds typically have greater liquid water content than nonraining clouds, and with a distribution of much larger drops. The larger size of the raindrops increases their absorption per unit mass. It will also cause enough scattering, such that its contribution should not be ignored. The theory of scattering and absorption by dielectric spheres was first discussed by Mie (1908), and applied to rain and clouds by Gunn and East (1954). These computations are well understood, despite being mathematically complicated. Introducing ice above the freezing level significantly increases the importance of scattering. Although the scattering cross section of an ice sphere is comparable to that of a liquid sphere of the same size, the absorption cross section disappears. In our conceptual model, if the ice layer above the liquid hydrometeors is thick, a photon will have many opportunities to scatter out of the atmosphere before being absorbed. For wavelengths of a few millimeters or less, scattering by ice particles with densities and sizes more characteristic of rain can produce extremely low brightness

temperatures. These low brightness temperatures do not depend on the background and can be used to indicate rain over either land or ocean.

A radiative transfer model for a typical rainfall cloud was given by Wilheit *et al.* (1977). A Marshall Palmer (M-P) distribution (Marshall and Palmer, 1948) of raindrops was assumed from the surface up to the freezing level (0°C isotherm). A standard lapse rate of 6.5 K/km was used and the relative humidity was assumed to be 80% at the surface, increased linearly to 100% at the freezing level, and remained at 100% above that. These assumptions couple the freezing level, the surface temperature and the precipitable water. By selecting any one of them the other two will be determined for the purposes of the model. In addition to the M-P distribution of raindrops, an arbitrary nonprecipitating cloud layer containing 0.5 g/m^3 of cloud liquid water was assumed in the 0.5 km just below the freezing level. In reality the relationship between suspended cloud liquid water and precipitating water droplets would actually change over the life of a storm.

Figure 2.6 shows the results of computations based on this study's model for frequencies of 6.6, 10.7, 19.35, 37 and 86.5 GHz with a view angle of 54° for an ocean background. The computations were made for two freezing levels as indicated in the figure. Only the horizontal polarizations calculated are shown; the vertically polarized brightness temperature is always equal to or greater than the corresponding horizontally polarized temperature for a given freezing level. For all frequencies the brightness temperature increases towards a maximum and then drops off as rainfall rates continue to increase.

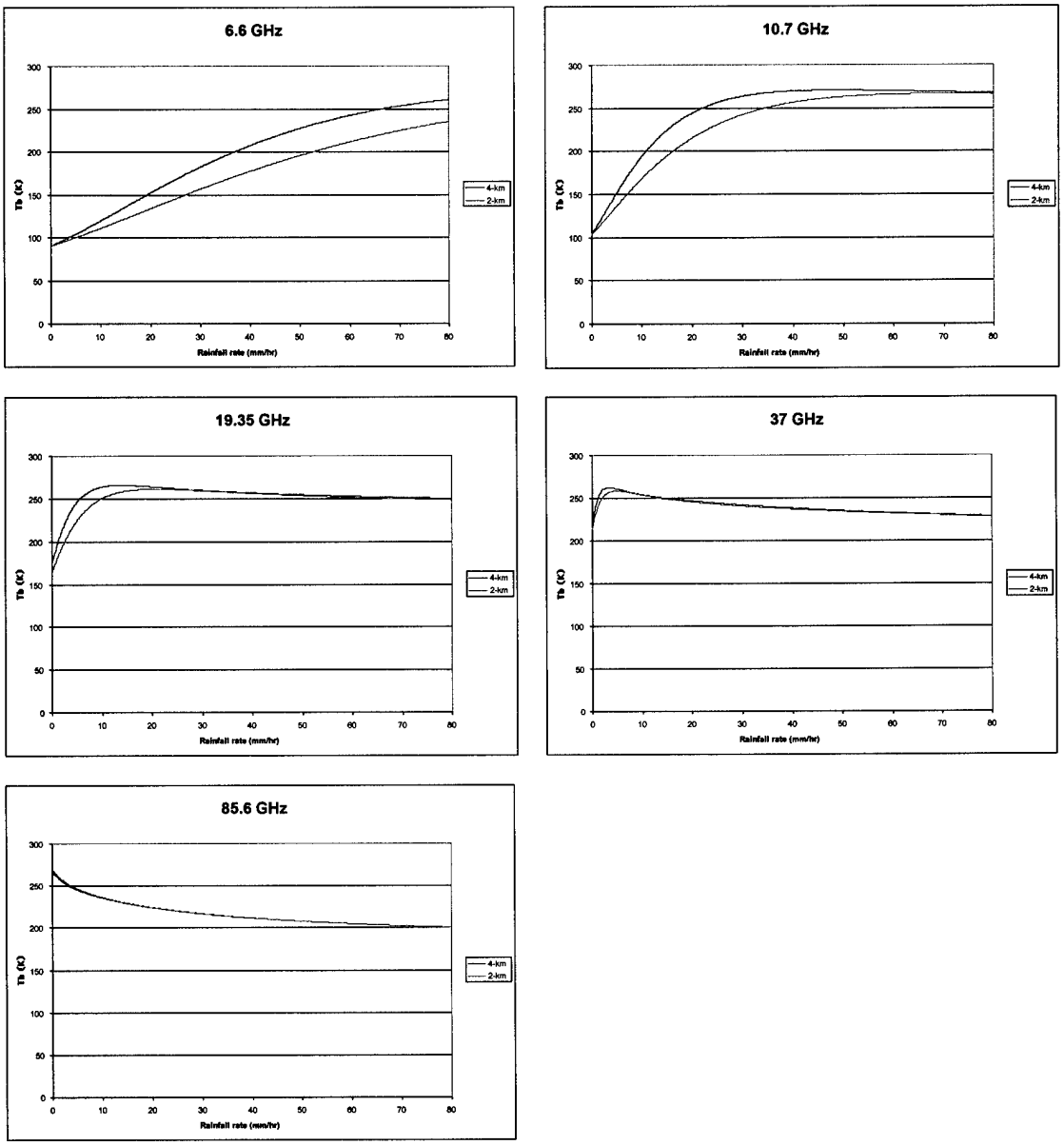

Figure 2.6: Computed brightness temperatures as a function of rainfall rate for selected frequencies.

The curves are conceptually similar in the range of rainfall rates for which the curve increases (emission region) and the range for which the curves are decreasing (scattering region). The 19.35 GHz curve with a 4-km freezing level may be used as an example. Brightness temperature increases rapidly with rain rates between 1 to 7 mm/hr. It reaches

a maximum near 265 K and then decreases slowly as rain rates increase. In the increasing part of the curve, the absorption and emission processes dominate. As rain rates continue to increase, the atmosphere becomes nearly opaque, and increasing absorption has little effect. However, the scattering term continues to increase. Using the Monte-Carlo model concept, consider a photon sent into the atmosphere. It is most likely to be absorbed at a temperature of (or slightly higher than) 273 K. However, it has some probability of being scattered out of the atmosphere back to space, *i.e.,* to be absorbed at a temperature of 2.7 K. This small amount of scattering will slightly lower the average temperature at which the photons are absorbed, and produce a lower observed brightness temperature.

Curves for different freezing levels in this brightness temperature versus rain rate (*Tb-R*) relationship all separate at low rain rates. The most noticeable separation can be seen at 6.6 GHz, where the Tb varies by almost 35 K at 50 mm/hr. As the freezing layer is lowered, the liquid water content possible in an atmospheric column decreases. This separation in the curves is caused by the contribution of liquid water content, which absorbs and emits strongly at this low frequency, to the brightness temperatures.

The 89 GHz rainfall rate/brightness temperature relationships shown in Figure 2.6 displays similar behavior (absorbing and scattering regimes) as at 10.7 GHz. However, because absorption and scattering coefficients are much larger at 89 GHz, the *Tb* to rainfall relation reaches saturation at much lower rainfall rates. For rainfall rates greater than 1 mm/hr, the relationship decreases monotonically. This is the scattering regime previously discussed.

In the computations resulting in Figure 2.6, the brightness temperature at low frequencies is predominantly a function of the total absorption (in Eqn. 2.3), with scattering being only a minor correction. This is particularly true where the *Tb-R* relationship increases. Observations in this range could be considered a measure of the absorption coefficient, k_{abs}, assuming the thickness of the absorbing layer is known. The ascending portion of the R-T relationship over ocean is called the emission (or absorption) regime for rainfall measurements. The rain rate follows from the absorption coefficient suggested by the measurements. The descending portion of the R-T relationship can be considered a measure of the scattering coefficient, k_{sca}. This regime is called the scattering regime. With frozen hydrometeors being more efficient scatterers of microwave radiation than liquid hydrometeors, the scattering regime is most sensitive to the frozen hydrometeors. Due to the high emissivity of land backgrounds, only scattering signatures present any real information over land. The rainfall rate over land must be inferred from the ice scattering signature, and cannot be derived directly from the emission signal from raindrops.

The absorption coefficient, k_{abs}, and the scattering coefficient, k_{sca}, can be written as an integral over the drop size distribution. Rain rate, as long as we ignore updrafts and downdrafts and subcloud layer evaporation of rain drops, can be expressed as:

$$R = \int V(D)(\pi D^3/6)N(D)dD \qquad (2.4)$$

where $V(D)$ is the fall speed of the drops as a function of diameter, D, (Foot and duToit, 1969), $N(D)$ is the number density of drops with diameters between D and $D + dD$; and the volume of a drop of diameter D is $\pi D^3/6$.

Radar does have the disadvantage of being highly sensitive to drop size distribution, a characteristic not shared by radiometers operating in the absorption regime. This sensitivity is fairly easy to show. Generally, many parameters could be expressed as $P_i=F_i[D^3N(D)]dD$, where F_i is a generic function, the specific form of which depends on the desired parameter P_i. Choosing to group the D^3 factor with the drop size distribution for graphical clarity produces a volume-weighted drop size distribution. The factor for rain rate F_{RR} becomes $\pi V(D)/6$. The factor for absorption coefficient, F_{ABS}, is then proportional to the ratio of the Mie absorption to the Rayleigh absorption because of the D^3 factor grouped with $N(D)$.

As most ground-based radars operate at frequencies below about 6 GHz, raindrops fall within the Rayleigh regime resulting in a backscatter coefficient proportional to D^6. Since a factor of D^3 is grouped with $N(D)$, F_{BS} is proportional to D^3. F_{RR} and F_{ABS} for 19.35 GHz are shown in Figure 2.7. $D^3N(D)$ is also given for a Marshall-Palmer distribution at 10 mm/hr. Although M-P distributions are unique for any particular rain rate, actual drop size distributions can vary a great deal for that rain rate. As long as $D^3N(D)$ is large, F_{RR} and F_{ABS} are similar. Because of this, small changes in N will have a proportional effect on the rain rate and the absorption coefficient. It can then be assumed that an absorption coefficient measurement is almost equivalent to a rain rate measurement independent of the details of the drop size distribution. On the other hand, a typical radar backscatter measurement, F_{BS}, is a very different moment from the rain rate; the largest drops in the distribution dominate it. F_{BS} would be presented as a cubic curve in this representation. Radar backscatter measurements for a given rain rate are very sensitive to the details of the drop size distribution that generated the given rain rate.

This is one of the primary problems in the use of ground-based radars in the measurement of rainfall intensity. However, if radars are used to provide an attenuation measurement (Atlas and Ulbrich, 1978) they have the same characteristic as the radiometric measurement (a lack of sensitivity to the DSD).

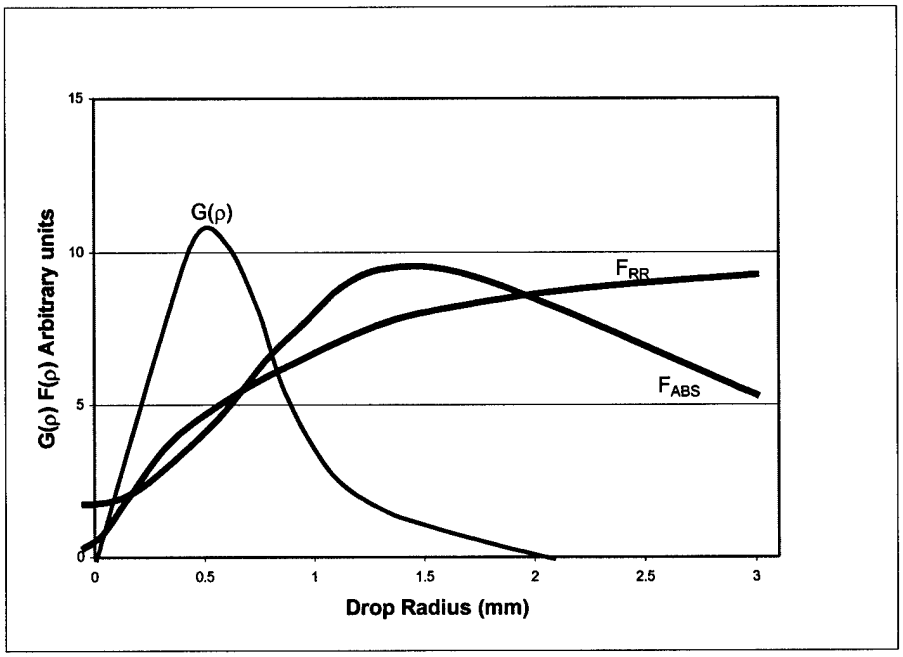

Figure 2.7: Moments of the drop size distribution (F_{RR} and F_{ABS}) and a volume-weighted Marshall Palmer distribution ($D^3N(D)$), $G(\rho)$, for a 10mm/hr rain rate as a function of the drop diameter.

2.3 Instantaneous Ocean Rainfall Algorithms

Using RTEs, a brightness temperature, *Tb,* can be calculated, given a temperature, water vapor and hydrometeor profile. An example of such a computation through a simulated atmospheric profile described by Wilheit *et al.*, (1977) was shown in Figure 2.6. From that profile, an inversion procedure is needed so that given a brightness temperature *Tb*, a rainfall rate, *R*, can be acquired. It might be suggested that simply inverting the curves shown in Figure 2.6 would suffice, since the double valued nature of

the relations is easily resolved by a combination of two or more channels. However, the relations derived in Figure 2.6 are applicable only to the cloud structure particular to this study. Although this study concentrates on rainfall retrievals based on the Wilheit *et al.*'s technique, there are alternative retrievals available. Irrespective of the final form of the inversion, however, they all suffer from a common set of uncertainties. Wilheit (1986) categorized these errors into four types:

a) Sampling. Sensors measure instantaneous rain rates, while integrated rainfall over some period of time is a more desired quantity. Since the integral can only be estimated on a statistical basis, the number and distribution of samples is very important. Because of the low number of sensors, the total number of passes over any given location is low. Due to the variability of rain, and the existence of diurnal rain cycles in many areas, there is a potential for errors. Further study regarding the scope of sampling error for TRMM specifically has found it to be less than 10% of the mean for rainfall averaged over a 500 by 500 km area (Bell, *et al.*, 1990).

b) Inhomogeneity. This is the beam-filling problem that is described in detail in the next section.

c) Details of the transfer function. Although the transfer function that relates microwave emission to rain rate is well understood, the details must be considered. These details are the assumptions that are built into the retrieval models. They include the rain layer thickness, the water-vapor dependence of the brightness temperature (dependent on the freezing level in the model), and the drop size distribution.

d) Scattering regime. Modeling of the scattering-dominated regimes is not well understood. Ice is currently modeled as an ensemble of spheres, while ice particle

shapes in actual rainstorms are more varied. The distribution of ice particles for a given rain rate is unknown, and are not unique. Because of this an empirical relation between scattering and rain rate is still used.

2.4 The Beam-Filling Error Described

Nonuniform rain rates within a field of view (FOV) and a nonlinear rain rate-microwave brightness temperature relation lead to a bias in the estimation of areal average rain rate from space-borne microwave measurements (Chiu, *et al.*, 1990). The nonlinear nature of the temperature-rain rate relationship is easily seen by graphing the homogeneous FOV curve (See Figure 2.8, red curve). As the FOV becomes more heterogeneous, this temperature-rain rate curve will move to the right of the homogeneous curve (See Figure 2.8, blue dots). In this particular figure, the amount of inhomogeneity is expressed by dividing the FOV rain rate standard deviations by the mean rain rates (a value that will be referred to as the "inhomogeneity parameter" in this study). The reason for this "shift" is easily demonstrated.

Figure 2.9 shows a FOV that approximates the TRMM TMI passive microwave sensor at 19 GHz (20-km resolution vs. the actual 23-km resolution). The sensor detects the average brightness temperature from the area (208 K in this example), and the retrieval uses the temperature-rain rate relation (Figure 2.8) to derive a rain rate based on average temperature. In this manner, we derive a rain rate for the scene of 1.8 mm/hr. However, if we use the resolution of the TRMM PR (4 km X 4 km) and observe a more detailed view of the scene, the results change, although the average brightness temperature remains the same (Figure 2.10).

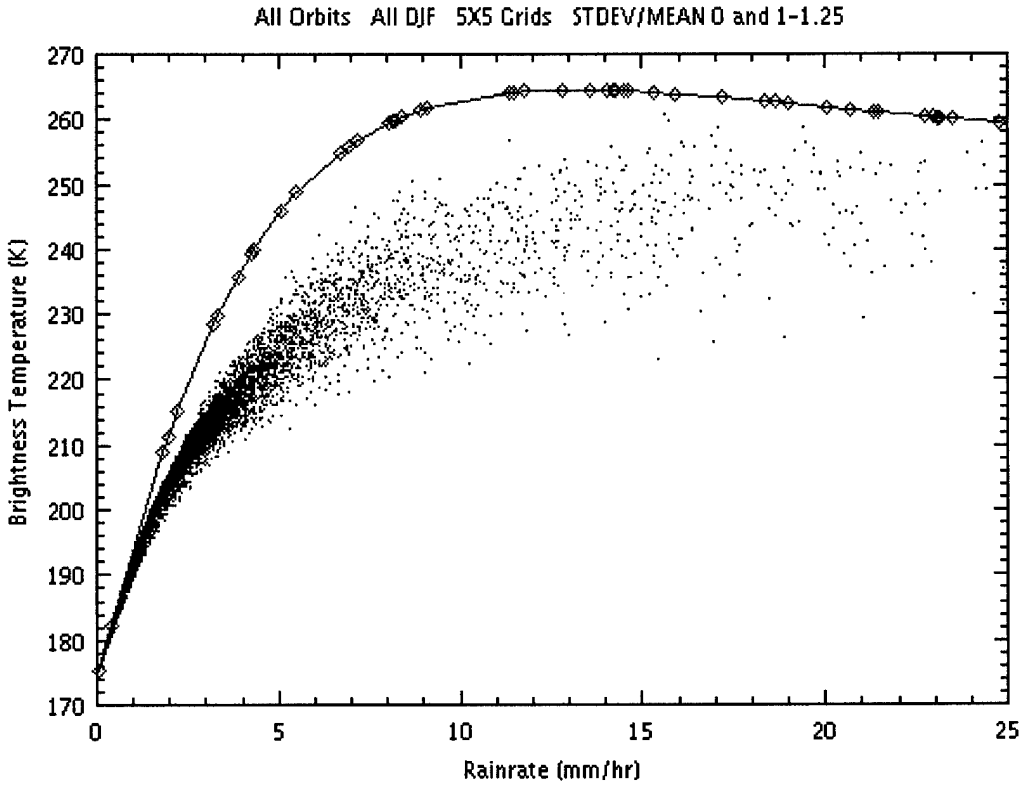

Figure 2.8: Homogeneous FOV temperature-rain rate relation (red curve) vs. heterogeneous FOV temperature-rain rate relation (blue dots).

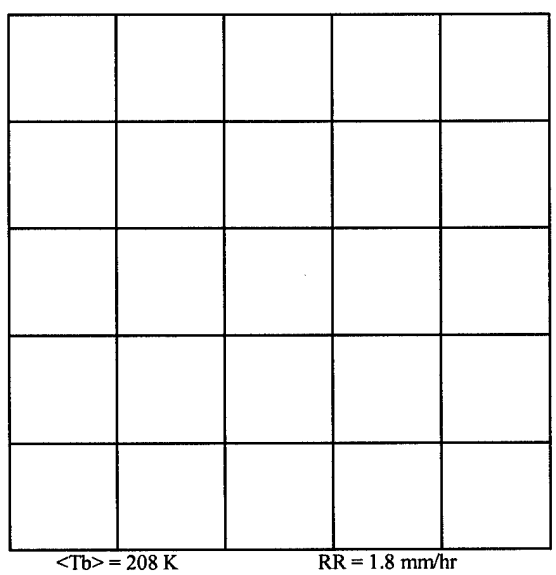

Figure 2.9: Homogeneous FOV

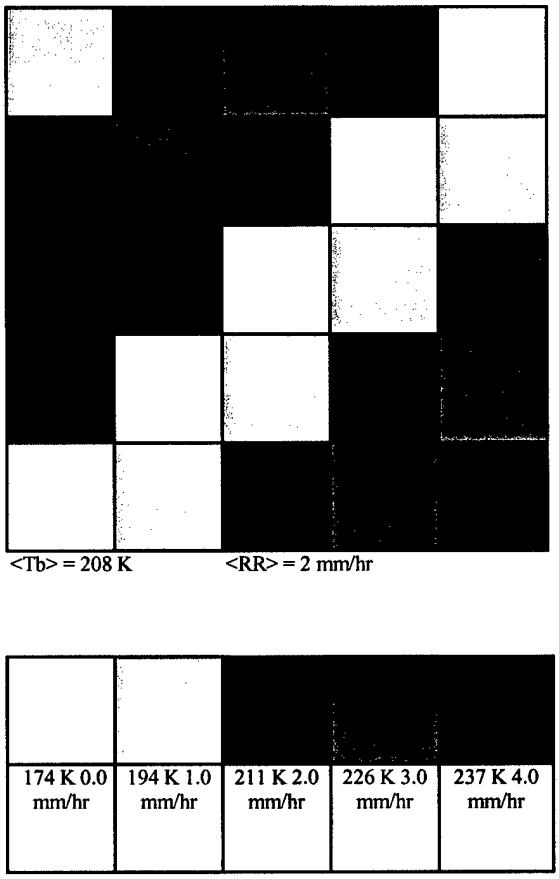

Figure 2.10: Actual heterogeneous FOV with legend

Using the temperature-rain rate relation to derive rain rates for each TRMM PR grid box, and then averaging those rain rates to acquire an average rain rate for the entire scene yields 2.0 mm/hr. Because the TRMM TMI doesn't observe the heterogeneity at the subresolution scales of this scene, it will underestimate the average rain rate by approximately 0.2 mm/hr (10%) in this case. The rain rate acquired from the passive microwave sensor would require a correction (multiplying the result by 1.1) to raise it to the actual rain rate. This correction is referred to as the beam-filling correction.

2.5 Beam-Filling Corrections and the TMI Algorithm

The approach taken to correct for the beam-filling error has been to make the assumption that inhomogeneity was constant around the globe. Much of the data used to calculate this constant bias came from the GARP Atlantic Tropical Experiment (GATE) radar data sets. Austin and Geotis (1978) concluded that the average error at the 25-km resolution was approximately a factor of 2. Chiu *et al.* (1990) published a more detailed analysis, and concluded rainfall was underestimated by a factor of 1.43, 1.64, 1.72 at resolutions of 10, 25, and 40-km, respectively (Wilheit, *et al.*, 1991). These results could then be extrapolated to the resolution of any of the passive microwave sensors in use.

Wang (1996) described a method by which airborne radar data was used to drive a simulation that would derive beam-filling corrections based on freezing level height and footprint size. Using this method, he determined the average beam-filling correction at the 20 km X 20 km footprint size of the TMI 19.35 GHz frequency for a 4-km freezing level to be 1.585. This is the type of correction that is now applied to the monthly estimates of rainfall produced by the TRMM level 3 rain algorithm (product 3A11 in the TRMM data system).

While it is known that rainfall inhomogeneity and thus the beam-filling correction would have regional and temporal variations, there was no data available to treat this problem in such a manner. One of the advantages of TRMM carrying both active and passive sensors for detecting rainfall is that the PR can measure rainfall with a 4-km resolution for time periods identical to the TMI scans. Using those PR measurements, it is possible to estimate the variability of rainfall within a 20 km TMI FOV and to distinguish the regional variabilities. Using TRMM PR data, it is possible to map out this

variability and the changes required to the beam-filling corrections in order to compensate for it.

This brings us to the heart of the problem involved in using a constant correction across the entire globe. If an area has rainfall that is more homogeneous than the average, retrieved rainfall will be overestimated because the beam-filling correction is too large. The exact opposite will occur in areas that are more heterogeneous. Regional rainfall studies of rainfall behavior could lead to incorrect conclusions if the regional differences in rainfall inhomogeneity are not accounted for. From a global perspective, even if the current value for the beam-filling correction were correct, large-scale variations that might be associated with ENSO events studied by Soden would not be properly captured. Global effects on latent heating in the tropics would be poorly described, as the actual amounts of latent heating calculated from TMI rainfall estimates would suffer from the same tendencies. If we require the highest degree of accuracy possible, a better scheme to compensate for the beam-filling error is needed. Now that TRMM PR data is available, the current approach of using a universal correction for the beam-filling error can be improved upon.

Chapter 3

Project Description

3.1 The Eddington Approximation RTE

Due to the large number of radiative transfer calculations required by this project, there was a need to use a fast, yet accurate, RTE. The Eddington RTE meets those requirements. A study of the accuracy of this model was completed by Kummerow (1993). An explanation of the Eddington approximation is included in that paper.

In a plane parallel medium, the equation describing the transfer of monochromatic radiation at frequency ν is given by:

$$\cos\theta \, dI_\nu(z, \theta, \phi)/dz = -k_\nu(z) \, [I_\nu(z, \theta, \phi) - J_\nu(z, \theta, \phi)] \tag{3.1}$$

where $I_\nu(z, \theta, \phi)$ is the radiance at height z, propagating in the direction of θ, ϕ; k_ν is the extinction coefficient of the medium, and $J_\nu(z, \theta, \phi)$ is the source function given by:

$$J_\nu(z, \theta, \phi) = [1 - a_\nu(z)]B_\nu[T(z)] + a_\nu(z)/4\pi \int_0^{2\pi}\int_{-1}^{+1} P_\nu(\theta, \phi; \theta', \phi') \bullet I_\nu(z, \theta', \phi') d(\cos\theta') d\phi' \tag{3.2}$$

where $a_\nu(z)$ is the albedo for single scattering, $T(z)$ is the temperature of the medium, $B_\nu[T(z)]$ is the Planck function at frequency ν and temperature $T(z)$, and $P_\nu(\theta, \phi; \theta', \phi')$ is the phase function for scattering of radiation from direction θ, ϕ into θ', ϕ'. In the microwave portion of the spectrum at tropospheric temperatures, the Planck function is linearly dependent on temperature. Because of that, it is common to replace $B_\nu[T(z)]$ with $T(z)$, which implies that radiances must be interpreted as brightness temperatures rather than as power per unit area.

In the plane parallel Eddington approximation, radiances can be expanded into a series of Legendre and associated Legendre functions:

$$I(z, \theta, \phi) = I_0(z) + I_1(z)\cos\theta + \ldots \tag{3.3}$$

By terminating the series in this way, the phase function can also be expanded in Legendre polynomials:

$$P(\cos\vartheta)\sum_{l=0}^{N}\omega_l P_l(\cos\vartheta) = 1 + \omega_l \cos\vartheta + \ldots \tag{3.4}$$

where ϑ is the angle from θ', ϕ' to θ, ϕ. The source function $J(z, \theta, \phi)$ can be then written as:

$$J(z, \theta, \phi) = [1 - a(z)]T(z) + a(z)[I_0(z) + g(z)I_1(z)\cos\theta] \tag{3.5}$$

where the asymmetry factor g is given by $g = \omega_1/3$.

An approach used by Wu and Weinman (1984) used Eqns. (3.1) through (3.5) to obtain a pair of first order equations for I_0 and I_1:

$$dI_0(z)/dz = -k(z)[1 - a(z)g(z)]I_1(z) \tag{3.6a}$$

$$dI_1(z)/dz = -3k(z)[1 - a(z)][I_0(z) - T(z)] \tag{3.6b}$$

The atmosphere is divided into 2n + 1 levels in this solution. Eqns. (3.6a) and (3.6b) are rewritten in finite difference form and the solution is acquired numerically.

In order to calculate the radiation leaving the top of the atmosphere, it is necessary to define z_0 as the surface and z_n as the top of the atmosphere, with average layer values between 1 and n. Azimuthal dependence could come into the radiative transfer problem from three different sources: external, anisotropic sources of radiation, horizontally finite clouds, or azimuthal dependence of the surface reflectivity. As none of these cases will be considered here, the ϕ dependence in Eqn. (3.1) is unnecessary. For a Lambertian surface, and with no ϕ dependence, the radiances measured at the top of the first layer would be given by:

$$I(z_1, \theta) = \varepsilon T_s \exp[-k_1(z_1 - z_0)/\cos\theta] + 2/\pi \int_0^{\pi/2} (1 - \varepsilon)$$

$$\bullet I(z_0, \theta')\exp[-k_1(z_1 - z_0)/\cos\theta] \cos\theta' d\theta'$$

$$+ \int_0^{z_1} J_1(z, \theta)\, k_1 \exp[-k_1(z_1 - z)/\cos\theta] dz/\cos\theta \qquad (3.7a)$$

where ε is emissivity, T_s is the temperature of the surface, and $I(z_0, -\theta)$ will be defined in Eqn. (3.8). The surface contribution to the upwelling radiance is found in the first term of (3.7a). The contribution of the downwelling radiance reflected by the surface is in the second term. The last term is the contribution of radiation within the layer propagating upwards. Radiation emerging from layers above that first layer may be calculated using the recursive relation:

$$I(z_n,\theta) = I(z_{n-1},\theta)\exp[-k_n(z_n - z_{n-1})/\cos\theta] + \int_{z_{n-1}}^{z_n} J_n(z,\theta)k_n \exp[-k_n(z_n - z)/\cos\theta]dz/\cos\theta \tag{3.7b}$$

The downwelling radiance $I(z_0, -\theta)$ from Eqn. (3.7a) can also be found from a recursive relation. At the top of the atmosphere, $I(z_0, -\theta)$ is simply the background cosmic temperature of 2.7 K. Lower layers could then be calculated from:

$$I(z_{n-1},-\theta) = I(z_n,-\theta)\exp[-k_{n-1}(z_{n-1} - z_n)/\cos(-\theta)] + \int_{z_n}^{z_{n-1}} J_{n-1}(z,-\theta)k_{n-1} \exp[-k_{n-1}(z_{n-1} - z)/\cos(-\theta)]dz/\cos(-\theta) \tag{3.8}$$

Kummerow (1993) compared the Eddington approximation to an eight-stream discrete ordinate model, and found that differences were generally small. When multilayered cloud hydrometeor profiles were used, the differences never exceeded 3 K over the entire microwave spectrum of frequencies. The models also agreed to within 0.2 K when scattering constituents were not present. This is important to the study, because scattering is rarely important at the 19.35 GHz frequency considered in this study. Therefore, it was determined that the small increase in accuracy from using discrete ordinate or Monte Carlo solutions could be sacrificed in favor of faster calculations.

3.2 The Atmospheric Profile

Before the upwelling radiance can be computed, the surface properties and atmospheric constituents must be fully specified. The surface parameters include the surface skin temperature (BTEMP), the ambient temperature of the surface layer (LYRTEMP(0)), the height above the surface of the bottom of the lowest computational layer (ZHT(0)), and the wind speed over water at the surface (WIND). The parameters

concerning computational layers above the surface include the height of the top of the layer (ZHT(N)), the temperature at the top of each layer (ZTEMP(N)), the average relative humidity of each layer (RELHUM(N)), the average cloud liquid water content (CLW(N)), and the average liquid (RAINL(N))and ice (RAINI(N)) rainfall rates within each layer.

This study used a simple three-layer model. The surface skin temperature and layer temperature were set at 298 K, the height of the first layer above the surface at 0 km, and the surface winds as calm. The three atmospheric layers were set at top heights of 4, 6, and 8 km. ZTEMP dropped from 272 K at the lowest layer, to 262 K in the middle layer, and to 248 K at the highest layer. Relative humidities were set at 90% and cloud liquid water at 0.1 g/cm^3 for all layers.

This leaves RAINL and RAINI as the only remaining free variables. The surface rain rate was used as the RAINL in the lowest atmospheric layer, with RAINI being set at 0.0 for that layer. Ratios of the RAINL of the lowest level were used to get the values of RAINL and RAINI at higher layers. RAINL(2), the middle layer, was set as 25% of RAINL(1), while RAINI(2) being set to 1.25 X RAINL(2). In the top layer, RAINL(3) was set at 3.125% of RAINL(1), and RAINI(3) was set to 6.0 X RAINL(3).

As can now be seen, the only true free variable is RAINL(1), which is set by the surface rain rate. In this manner surface rain rates can be input into the model, and the resulting output would be a corresponding brightness temperature. In order to speed up the calculations used later in the study, a lookup table was developed for rain rates varying from 0 to 300 mm/hr at 0.01 mm/hr intervals.

3.3 Methodology

Three years of PR data covering December, January, and February of 1997-1998, 1998-1999, and 1999-2000 over the East and West Pacific (see boxes in Figure 3.1) were used to develop mean beam-filling corrections. These data provide an ample sample size to determine the necessary statistics, which are then applied to a 3-year time series for the TRMM TMI coverage area.

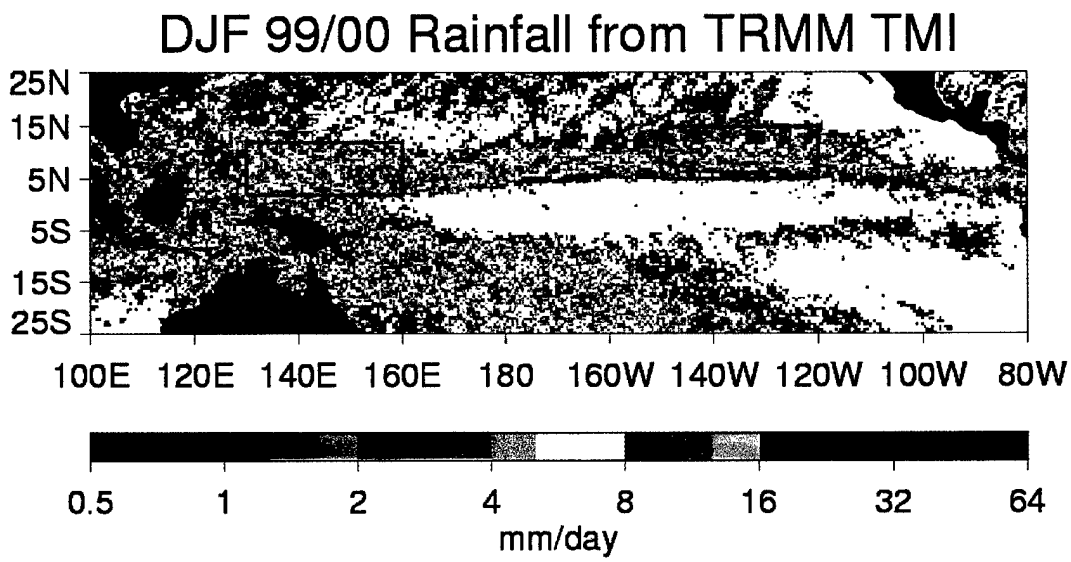

Figure 3.1 Rainfall map from TRMM showing the west and east Pacific boxes.

A program was developed that would ingest this 4-km resolution data, group it into 20-km grid boxes (5X5 pixels), and using the lookup table generated by the Eddington RTE, produce values of mean rain rate (<RR>)

$$< RR >= \sum_{n-1}^{25} RR_n / 25 \tag{3.9}$$

standard deviation (σ_{RR})

$$\sigma_{RR} = \left[\frac{1}{25-1} \sum_{n=1}^{25} (RR_n - < RR >)^2 \right]^{0.5} \tag{3.10}$$

average brightness temperatures for the 5 X 5 pixel box

$$<Tb>=\sum_{n=1}^{25} Tb_n / 25 \tag{3.11}$$

and the plane parallel rain rate based on *<Tb> (RRPP).* The program did include a screening function that removed all nonraining 5 X 5 groups of pixels, so that they would not be considered in the next step of the procedure. The output was a table listing mean rain rate, average *Tb*, plane parallel rain rate from average *Tb*, and the $\sigma_{RR}/<RR>$ (the inhomogeneity parameter) for each grid box.

Once the values had been calculated for the entire nine months of data (410,000 groups of 5 X 5 grid boxes), it was initially thought that a bias could be calculated as a function of the inhomogeneity parameter alone. As will be seen in the next chapter, the curve of bias vs. inhomogeneity was poorly behaved. The curve generally did not follow the expected trend of larger beam-filling correction with increasing inhomogeneity. However, when the bias was calculated as a function of mean rain rate and inhomogeneity parameter, this no longer occurred. With over 90% of all rain at PR resolution occurring at rates lower than 10 mm/hr, the curves developed from the lower rain rates behaved as expected. The details of this will be covered in the next chapter.

The calculation of the beam-filling bias as a function of mean rain rate and inhomogeneity was fairly straightforward. Having developed the tables mentioned in the previous section, the data were then segregated by mean rain rate in 1-mm/hr increments. The data for each rain rate increment was then further segregated by inhomogeneity parameter. The mean rate rates and plane parallel rain rates from the average Tbs were then summed for each group of data. Calculating the correction as a function of rain rate and inhomogeneity parameter was a simple matter of dividing the summations of rain

rates by the summations of the plane parallel rain rates for each group of data. This was done for rain rates varying from 1 mm/hr to 60 mm/hr (no rain rates over 60 mm/hr were seen during the nine month data period), and for inhomogeneity parameters of 0 to 4.9 (inhomogeneities above 4.9 are not possible as this constitutes the most variable rain, that in which only 1 in 25 pixels contain rain). The tables 3.1 through 3.9 show the results. Blanks in the table are mean rain rate and inhomogeneity combinations that did not occur in the data. The method used to "fill in the blanks" will be addressed in the next chapter.

Table 3.1 Beam-filling corrections (0-6 mm/hr).

σ_{RR}/RR	0 -1 mm/hr	1-2 mm/hr	2-3 mm/hr	3-4 mm/hr	4-5 mm/hr	5-6 mm/hr
0.125	1.002	1.007	1.014	1.023	1.033	1.041
0.375	1.005	1.024	1.050	1.076	1.099	1.124
0.625	1.011	1.057	1.116	1.175	1.232	1.291
0.875	1.021	1.106	1.218	1.328	1.440	1.536
1.125	1.035	1.177	1.358	1.533	1.688	1.809
1.375	1.053	1.274	1.524	1.757	1.960	2.152
1.625	1.081	1.380	1.707	1.996	2.213	2.415
1.875	1.115	1.493	1.916	2.206	2.450	2.757
2.125	1.144	1.632	2.162	2.545	2.830	3.092
2.375	1.167	1.785	2.399	2.837	3.000	3.368
2.625	1.199	1.930	2.661	3.171	3.390	3.928
2.875	1.191	2.102	2.908	3.461	4.155	3.700
3.125	1.264	2.310	3.244	4.013	4.014	4.871
3.375	1.178	2.557	3.545	4.018	4.844	3.877
3.625	1.214	2.795	4.038	4.773	5.879	5.541
3.875	1.284	3.101	4.296			
4.125	1.371	3.617	6.341	5.841		8.196
4.375	1.449	3.990	5.764			8.311
4.625	1.692	5.110	7.479			
4.875	1.084	6.236				

Table 3.2 Beam-filling corrections (6-13 mm/hr).

σ_{RR}/RR						
6-7 mm/hr	7-8 mm/hr	8-9 mm/hr	9-10 mm/hr	10-11 mm/hr	11-12 mm/hr	12-13 mm/hr
1.045	1.060	1.076	1.088	1.096	1.148	1.219
1.148	1.170	1.199	1.206	1.276	1.311	1.385
1.346	1.415	1.450	1.527	1.593	1.632	1.618
1.606	1.689	1.718	1.827	1.913	2.091	2.128
1.922	1.988	2.041	2.246	2.287	2.514	2.551
2.295	2.350	2.526	2.648	2.925	2.714	2.946
2.519	2.801	2.857	2.942	2.957	3.247	3.094
2.849	3.269	3.151	3.219	3.638	3.581	3.855
3.482	3.309	3.765	3.039	4.164	4.321	3.856
2.827	3.558	4.164	3.507	4.018		3.924
3.722	3.826	4.050	4.307	5.213	4.517	4.883
4.766	3.772	4.235	4.491	9.339		
3.309	4.415	4.827	4.656	6.277	5.161	7.119
6.978		4.388				
4.796			6.273	5.351	5.522	
	5.408					
	6.845					
	24.608					

Table 3.3 Beam-filling corrections (13-20 mm/hr).

σ_{RR}/RR						
13-14 mm/hr	14-15 mm/hr	15-16 mm/hr	16-17 mm/hr	17-18 mm/hr	18-19 mm/hr	19-20 mm/hr
1.269	1.372					
1.394	1.454	1.452	1.661	1.834	2.051	2.125
1.940	1.961	2.077	2.055	2.401	2.434	2.479
2.361	2.262	2.498	2.526	2.376	2.829	2.633
2.706	2.863	2.677	2.982	3.238	3.539	3.158
2.938	3.556	3.307	3.633	3.852	3.168	3.582
3.492	3.595	4.363	3.825	4.036	4.270	5.080
3.941	4.413	6.039	2.719	5.658	4.713	5.363
5.038	5.276	5.478	4.262	4.665	4.212	
3.514	7.785	5.374		3.930		
					14.340	
8.025		20.804	10.187			
7.353		10.253	12.069			

Table 3.4 Beam-filling corrections (20-27 mm/hr).

σ_{RR}/RR						
20 -21 mm/hr	21-22 mm/hr	22-23 mm/hr	23-24 mm/hr	24-25 mm/hr	25-26 mm/hr	26-27 mm/hr
2.421		2.422				
	2.645	3.288	2.934	3.507	3.292	3.339
3.317	2.617	3.524	3.030	4.342	2.921	3.994
3.872	3.992	4.444	4.241	4.697	4.363	4.826
3.470	4.433	4.660	4.622	5.796	5.130	5.033
4.610	3.547	5.661	5.064	4.646	3.748	
4.527	4.675	6.544		5.376	5.833	9.434
				8.421	4.628	8.426
	6.250		4.577			

Table 3.5 Beam-filling corrections (27-34 mm/hr).

σ_{RR}/RR						
27-28 mm/hr	28-29 mm/hr	29-30 mm/hr	30-31 mm/hr	31-32 mm/hr	32-33 mm/hr	33-34 mm/hr
3.279		3.575		3.878		
		3.700		4.324	4.095	
2.683	3.672	5.177	5.170	4.537	4.993	5.057
3.793	4.366	5.592	4.854	6.883	6.144	5.474
5.106	4.704	5.027	5.786		5.168	
6.941	5.440	6.992	6.689		7.900	
	17.674					12.993
	6.539			10.660		

Table 3.6 Beam-filling corrections (34-41 mm/hr).

σ_{RR}/RR						
34-35 mm/hr	35-36 mm/hr	36-37 mm/hr	37-38 mm/hr	38-39 mm/hr	39-40 mm/hr	40-41 mm/hr
4.734				5.082	5.332	6.131
5.327		5.153	5.400	6.601		6.002
5.669				6.965		
5.453		7.034			7.350	
7.825				17.394		

Table 3.7 Beam-filling corrections (41-48 mm/hr).

σ_{RR}/RR						
41-42 mm/hr	42-43 mm/hr	43-44 mm/hr	44-45 mm/hr	45-46 mm/hr	46-47 mm/hr	47-48 mm/hr
					7.560	
5.842	6.294				7.329	6.975
			6.843			
9.440						

Table 3.8 Beam-filling corrections (48-55 mm/hr).

σ_{RR}/RR						
48-49 mm/hr	49-50 mm/hr	50-51 mm/hr	51-52 mm/hr	52-53 mm/hr	53-54 mm/hr	54-55 mm/hr
	7.126					
7.498						

Table 3.9 Beam-filling corrections (55-60 mm/hr).

σ_{RR}/RR				
55-56 mm/hr	56-57 mm/hr	57-58 mm/hr	58-59 mm/hr	59-60 mm/hr
9.032		8.559		

Chapter 4

Beam-filling Correction Climatology

4.1 Beam-Filling Correction Curves

It was initially expected that a beam-filling correction could be applied as a function of the inhomogeneity parameter alone. This did not turn out to be the case. When beam-filling correction as a function of inhomogeneity was plotted, the curves did not behave as expected (Figure 4.1). According to previous research, as the inhomogeneity of the FOV increased, the beam-filling correction should have also increased.

The reason this didn't happen is fairly easy to explain. It was found that the vast majority of FOV's with moderate to high inhomogeneities tended to have lower mean rain rates. Referring back to Figure 2.8, it can be seen that at lower rain rates the difference between the heterogeneous and homogeneous FOV curves is very small. Thus, at lower rain rates the corrections are lower than at higher rain rates. If the sample size contained an overabundance of cases of moderate to high inhomogeneities with lower rain rates, it would skew the inhomogeneity/beam-filling correction relationship downward.

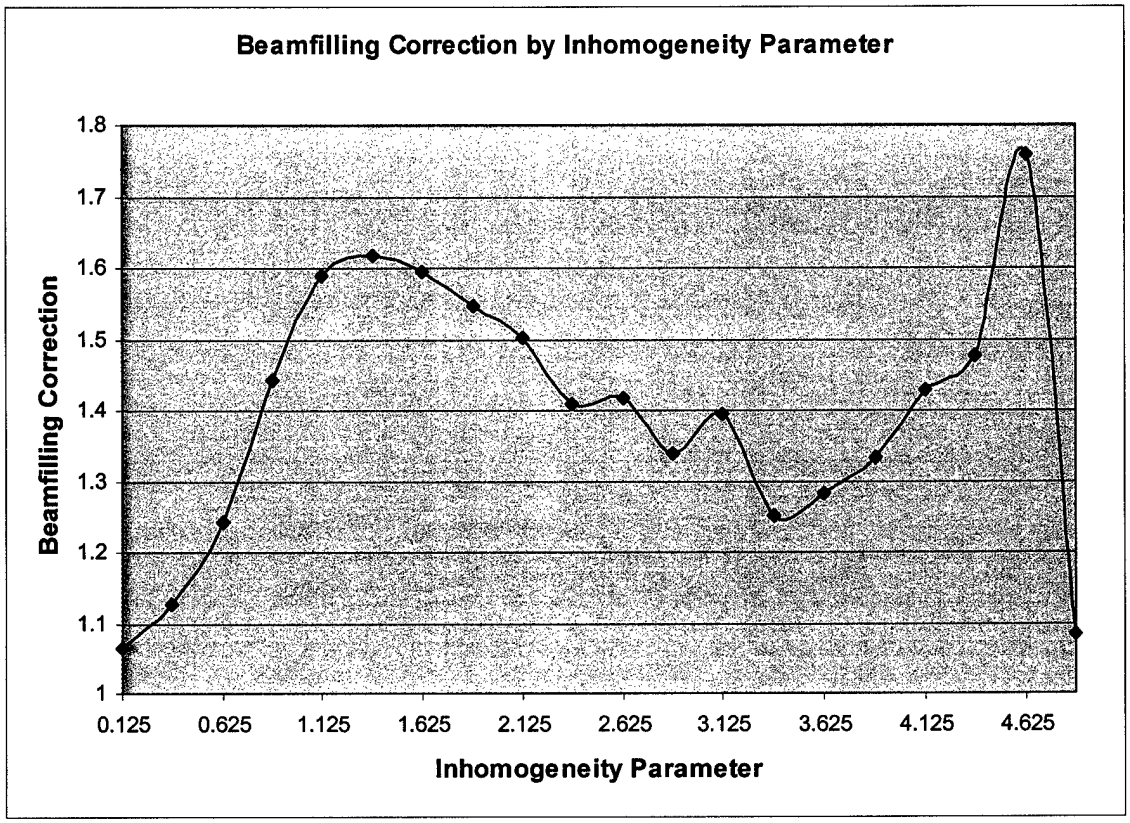

Figure 4.1 Beam-filling correction to inhomogeneity parameter relationship.

The solution to this problem was to make the applied beam-filling correction a function of both mean rain rate and inhomogeneity parameter. When this was done the curves fell in line with behavior that was originally expected, as can be seen in Figure 4.2. Although this figure does not show every rain rate and inhomogeneity parameter, the ones it does show account for over 80% of the world's rain at the 20 km FOV.

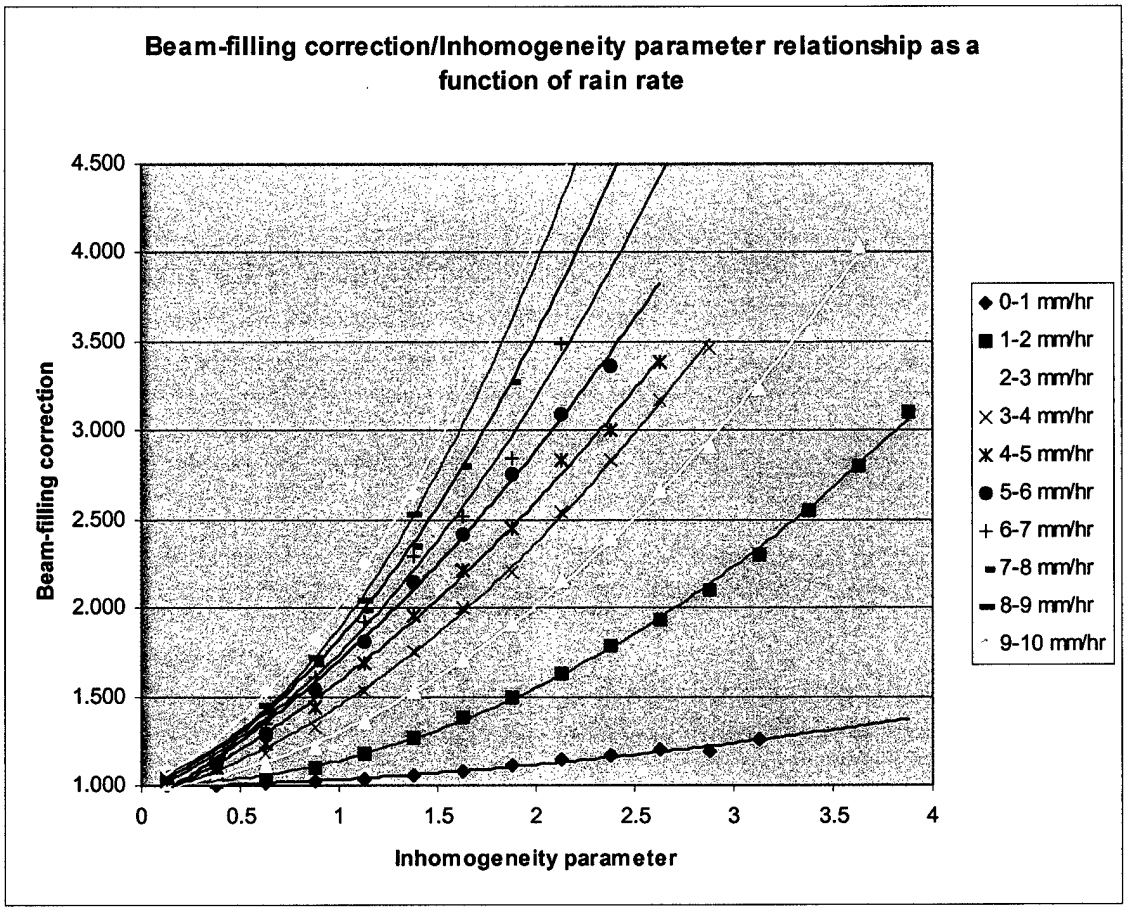

Figure 4.2: Beam-filling correction as a function of inhomogeneity parameter and rain rate. Lines represent the best polynomial fit to the data.

Once it was determined that a beam-filling correction applied as a function of rain rate and inhomogeneity parameter solved the problem presented by the predominance of low rain rate samples, the tables at the end of Chapter 3 were developed. As can be seen in those tables, there were combinations of rain rates and inhomogeneity parameters that did not occur in the nine months worth of data used. These areas in the tables were filled in using simple extrapolation. As these combinations don't occur often enough in nature to be statistically significant, it can be assumed that contributions due to those combinations will not affect the conclusions developed from this project.

4.2 Global Beam-Filling Climatology Results

The beam-filling correction tables and TRMM's 3A11 and 2A25 products were used to create the climatology maps. The 3A11 product contains monthly total rainfall amounts in 5-degree grid boxes, and is derived from TMI data. The 2A25 product contains instantaneous rain rates, and comes from the PR. The 2A25 data was collected in sets of 20 by 20-km grid boxes by month, and the mean inhomogeneity parameter and mean rain rate was calculated for each. The location of each box was rounded to the nearest degree of longitude and latitude. From these values, the applicable beam-filling correction, as computed from Tables 3.1-3.9, was applied. The corrections were then plotted against the information from the 3A11 product. This made it possible to see not only how beam-filling corrections vary, but also how this variation would affect monthly rainfall totals. The total rainfall is depicted as circles, and labeled in millimeters. The beam-filling correction is depicted by the colors and is unitless.

For display purposes, the data sets were adjusted to a 10-degree resolution, and averaged over 3-month periods for the sake of brevity (Figures 4.3 through 4.15). Monthly maps can be found in Appendix A. This resolution was the highest possible without causing clutter that would make portions of the maps illegible. By using a different display method, results could be depicted at the 1-degree resolution, if that level of detail were necessary for other applications.

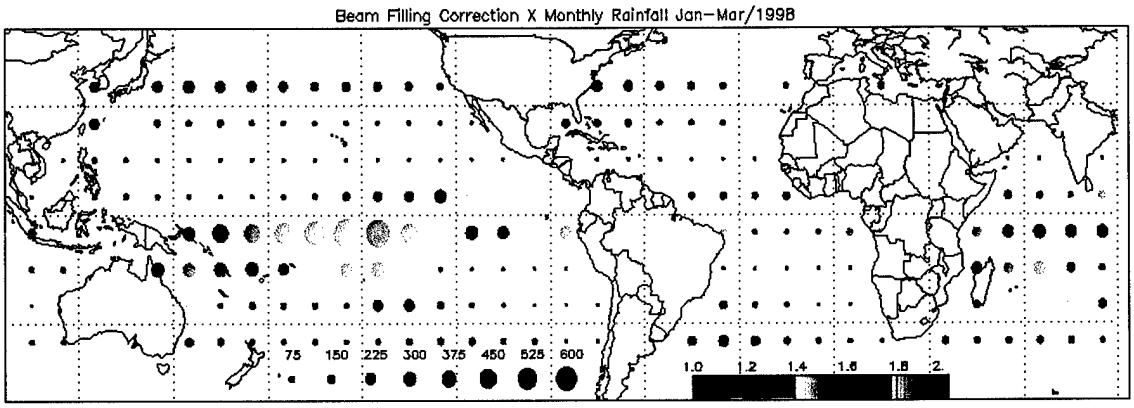

Figure 4.3: January-February-March 1998 beam-filling correction (color) and total rainfall in mm (circle size).

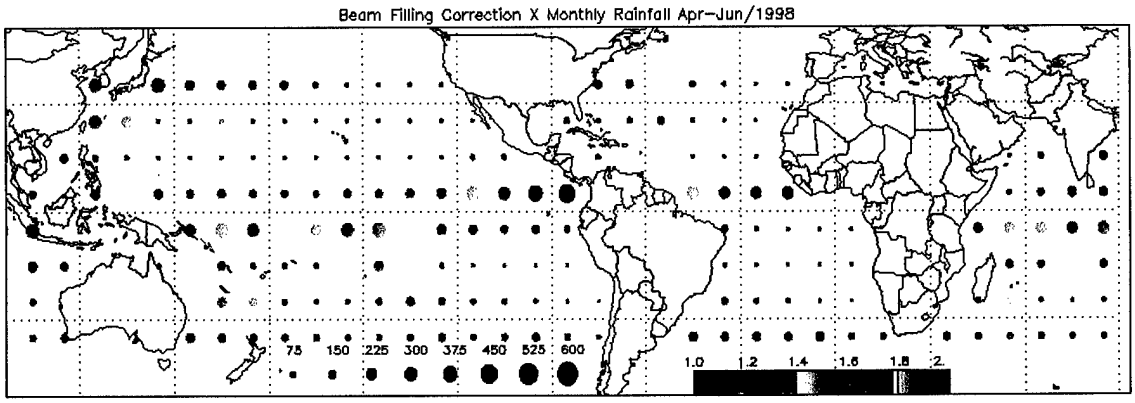

Figure 4.4: April-May-June 1998 beam-filling correction (color) and total rainfall in mm (circle size).

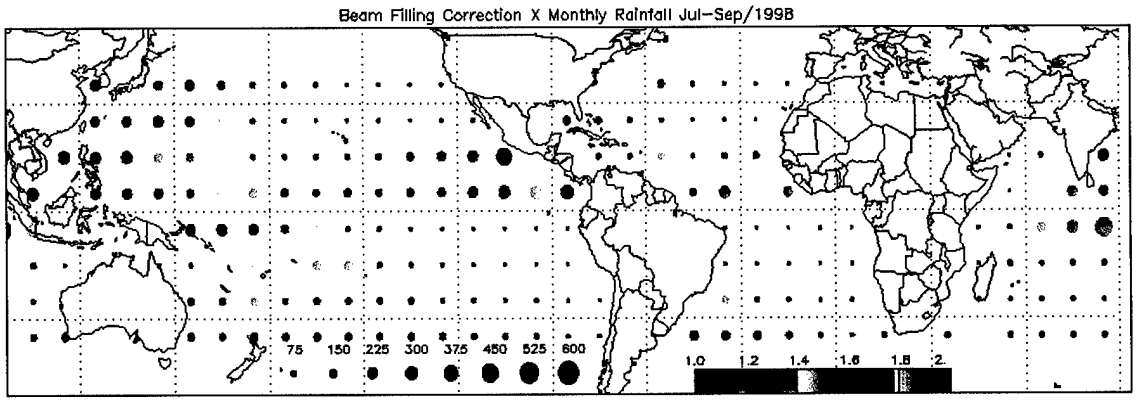

Figure 4.5: July-August-September 1998 beam-filling correction (color) and total rainfall in mm (circle size).

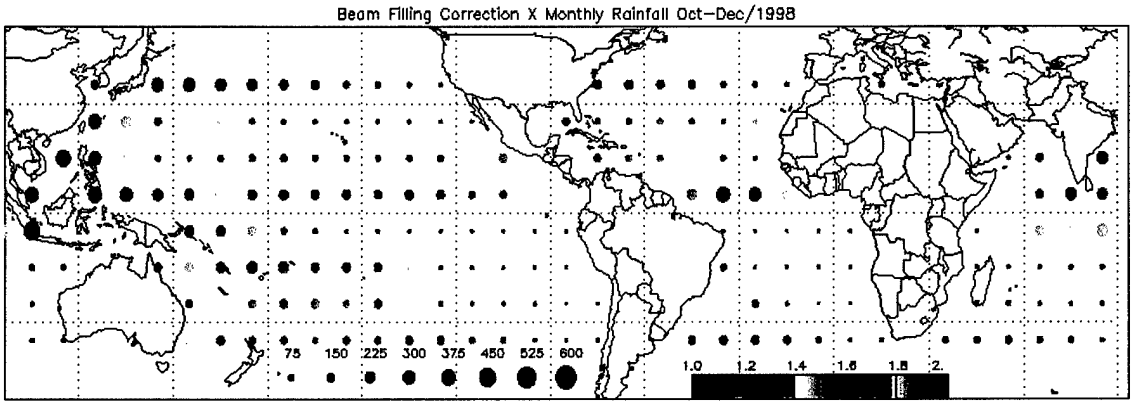

Figure 4.6: October-November-December 1998 beam-filling correction (color) and total rainfall in mm (circle size).

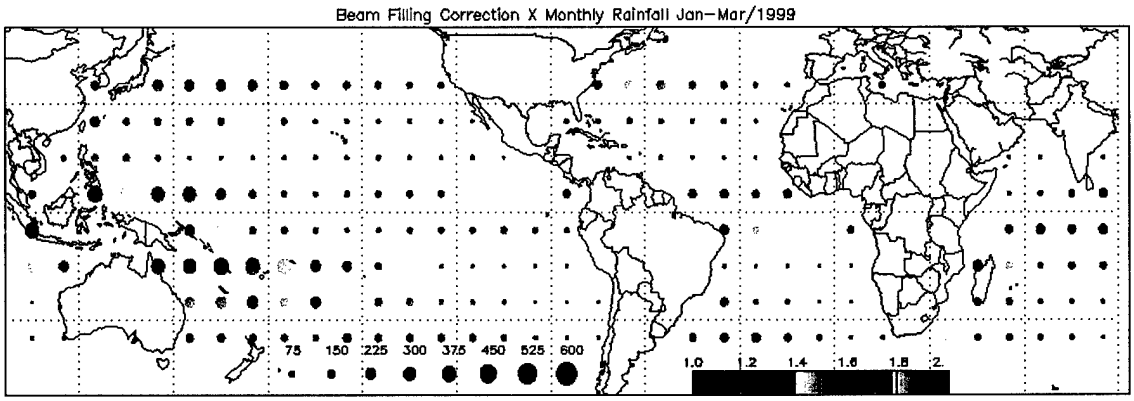

Figure 4.7: January-February-March 1999 beam-filling correction (color) and total rainfall in mm (circle size).

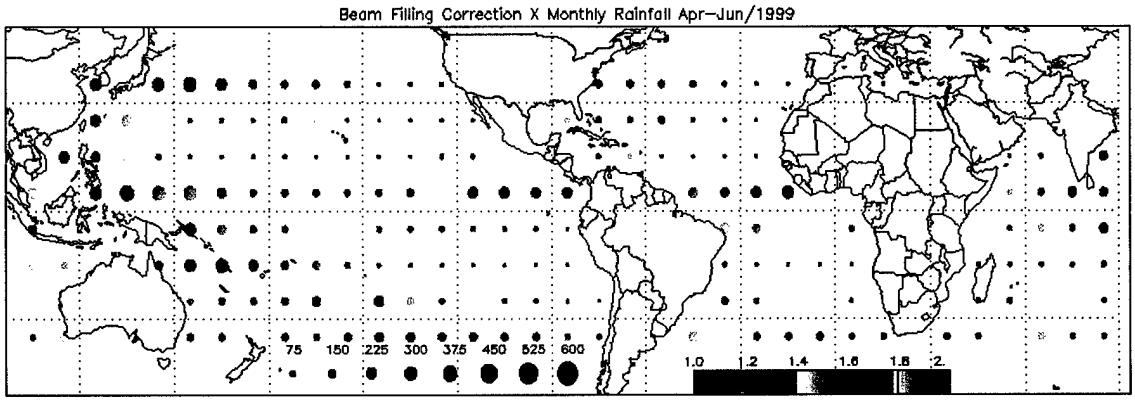

Figure 4.8: April-May-June 1999 beam-filling correction (color) and total rainfall in mm (circle size).

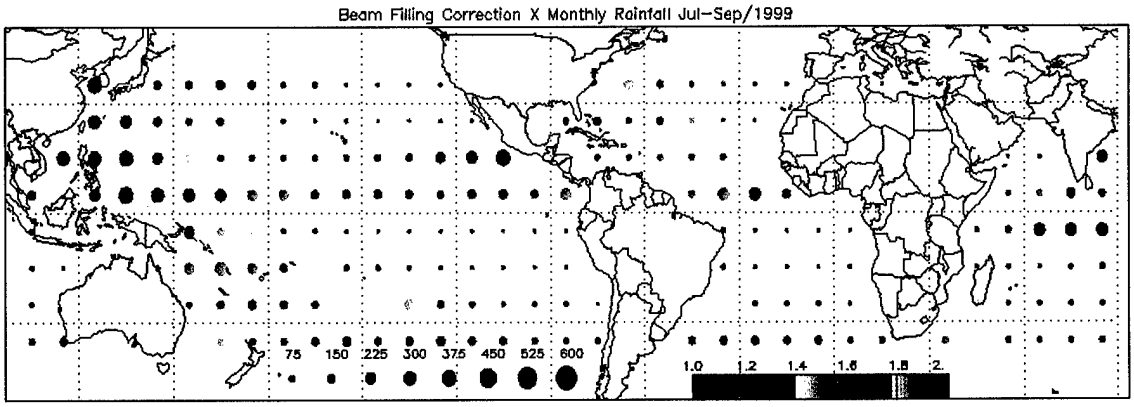

Figure 4.9: July-August-September 1999 beam-filling correction (color) and total rainfall in mm (circle size).

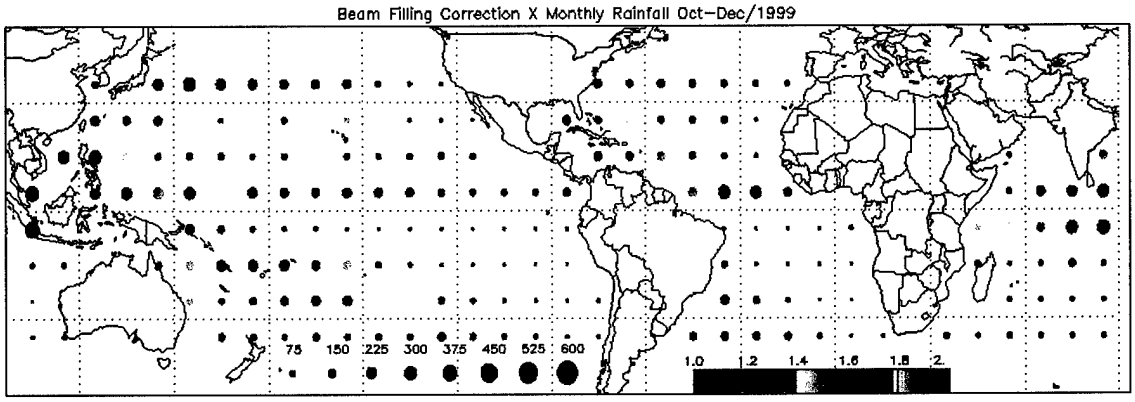

Figure 4.10: October-November-December 1999 beam-filling correction (color) and total rainfall in mm (circle size).

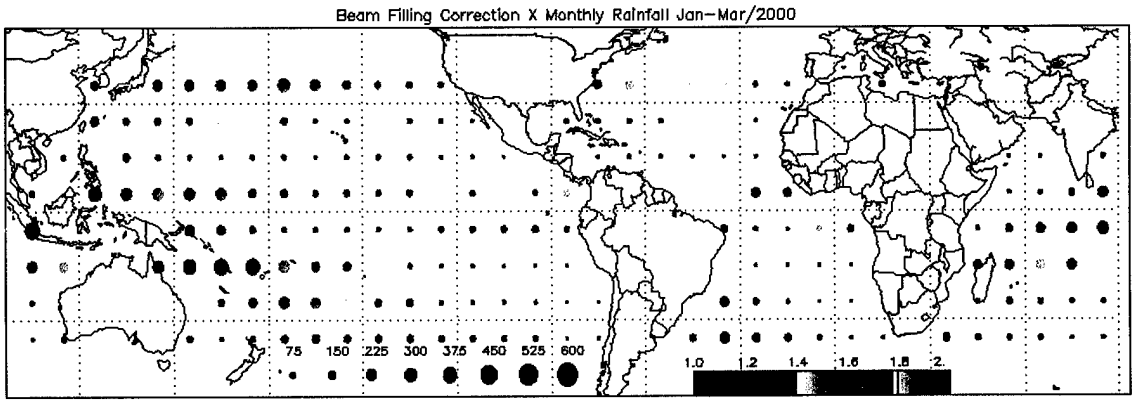

Figure 4.11: January-February-March 2000 beam-filling correction (color) and total rainfall in mm (circle size).

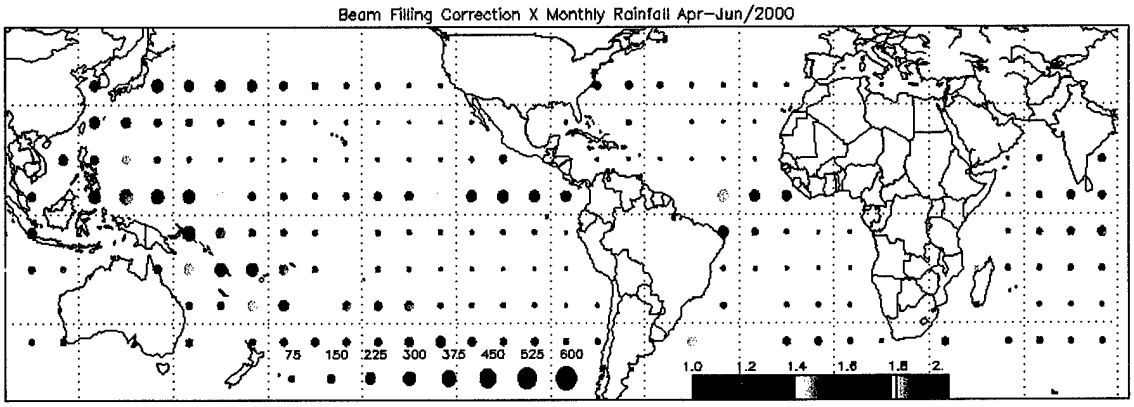

Figure 4.12: April-May-June 2000 beam-filling correction (color) and total rainfall in mm (circle size).

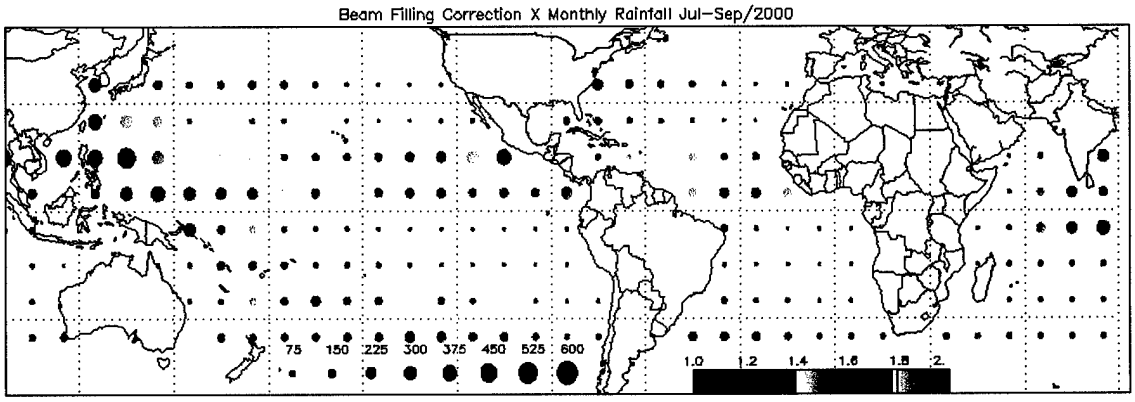

Figure 4.13: July-August-September 2000 beam-filling correction (color) and total rainfall in mm (circle size).

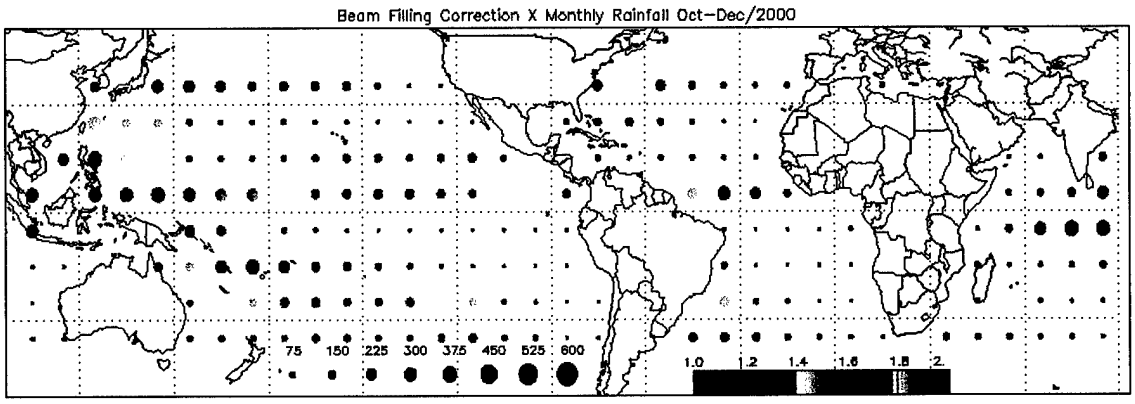

Figure 4.14: October-November-December 2000 beam-filling correction (color) and total rainfall in mm (circle size).

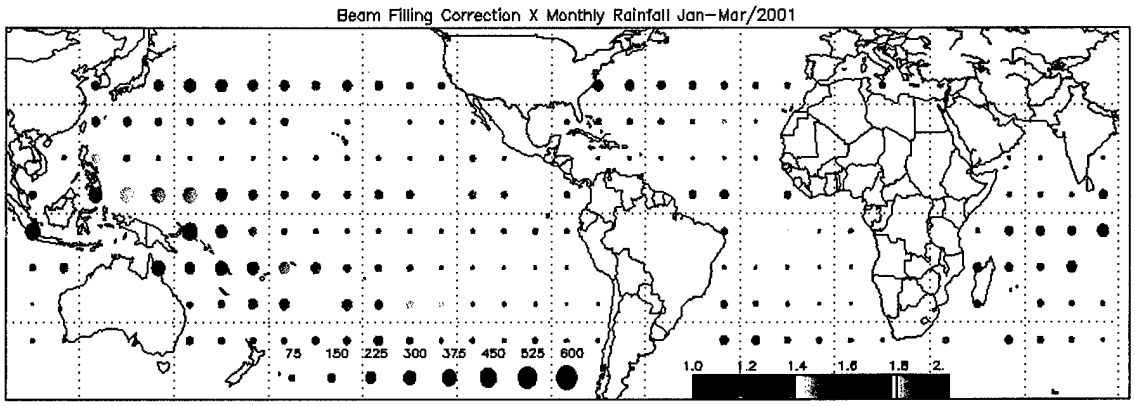

Figure 4.15: January-February-March 2001 beam-filling correction (color) and total rainfall in mm (circle size).

Some generalities can be quickly drawn from these maps. Areas of high inhomogeneity tend to concentrate in the west Pacific and Indian Oceans. Smaller areas occur near the ITCZ in the Central Atlantic and off the West Coast of Central America. Inhomogeneities are low over regions with cold ocean currents, as would be expected with the prevailing cloud types being stratiform.

It should also be noted that the inhomogeneities tend to decrease with higher latitudes. This may be a function of an increasingly unrealistic freezing level in the model, but it may also be a reflection of the lower fraction of convective clouds in mid-latitude systems as opposed to tropical systems.

Chapter 5

Sensitivity Studies

5.1 Effect of Ice Content on Model Results

As the 19 GHz channel used in this research can retrieve reasonably high rainfall rates before it begins to saturate, it was expected that the study results would not be greatly affected by the ice contents used in the atmospheric model. In order to verify this theory, the ice content used in the model rain cloud was varied and results were compared to the original model.

The methodology used for this study was straightforward, and closely follows that described in Chapter 3. Two new lookup tables were created using the Eddington RTE. In the first table, the RAINI ratios used in the original atmospheric model were doubled. In the second, the RAINI values were set to zero, essentially removing all ice. No other variables were changed. Once the new lookup tables were created, they were applied to the same data set described in Section 3.3. The beam-filling bias was again plotted as a function of inhomogeneity parameter, as originally seen in Figure 4.1.

The results are shown in Figure 5.1. It is fairly obvious that the lines practically overlap. Increasing the ice content increases the beam-filling bias slightly; removing the ice drops it. In general, however, the computed beam-filling correction at 19 GHz shows very little sensitivity to the ice content of the atmospheric model.

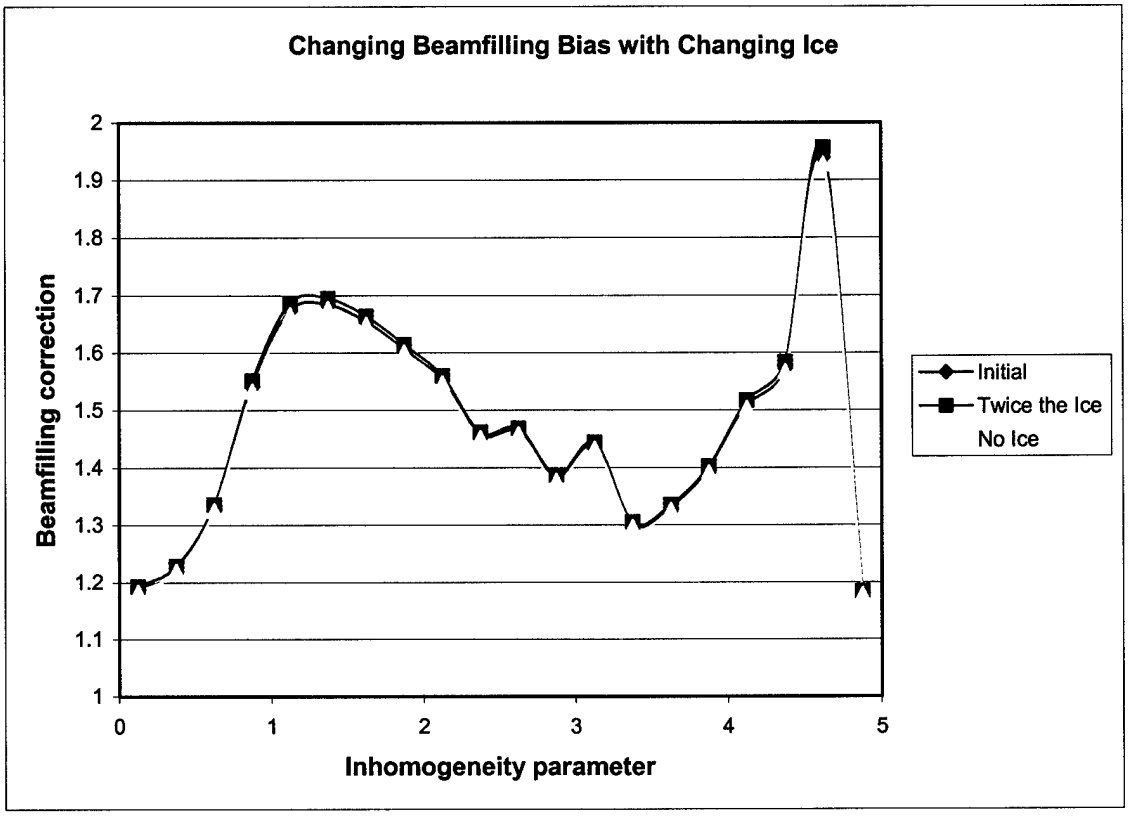

Figure 5.1: Beam-filling correction to inhomogeneity parameter relationship, with changing ice content

5.2 Ability of the 4-km Resolution Data to Capture the Full Rainfall Inhomogeneity

This study assumed that the 4-km resolution of the TRMM Precipitation Radar is high enough to capture actual global rainfall inhomogeneity. In order to test this theory, high-resolution radar data from the NOAA/ETL X-Band Doppler Radar at Wallops

Island, Virginia, and the NCAR S-Pol Radar during TRMM-LBA Brazil at Ji Parana, Rondonia, Brazil were used. Data from Wallops Island covered the period of March and April 2001. The TRMM-LBA data covered the period from mid-January through February of 1999. The data from both locations were of 0.25-km resolution.

The original data set used was from Wallops Island. Data were available as 25 by 25 km near surface CAPPI (Constant Altitude Plan-Position Indicator) images, with each image made up of 0.25 by 0.25 km grid boxes. A mean rain rate and standard deviation were calculated for a 20 by 20 km area of the image (the same as the size of the FOV studied), and from those an inhomogeneity parameter for the scene. After that the resolution of the data was artificially degraded by averaging the rain rates into 4 by 4 km boxes in order to simulate the TRMM PR resolution. Once those averages were completed, a new mean and standard deviation were calculated for the entire image based on this degraded resolution, and a new inhomogeneity parameter calculated for the scene.

The correlation between the original high-resolution inhomogeneity parameter and the new low-resolution results was very good. In fact, it was suspiciously good (Figure 5.2). It was concluded that the high correlation was mostly a function of the nature of precipitation over Wallops Island during the late winter-early spring. The majority of the precipitation events were stratiform in nature, with a naturally high degree of homogeneity. The sample size was also small, with only 14 events. It was decided that a larger sample size was needed with a wider variety of precipitation types.

TRMM/LBA Brazil data was used for that purpose. Data from this site offered a number of advantages, the greatest being that it was readily available. Thirty-two events

were identified using this data, significantly increasing the sample size. This data was analyzed in a similar manner to the Wallops Island information.

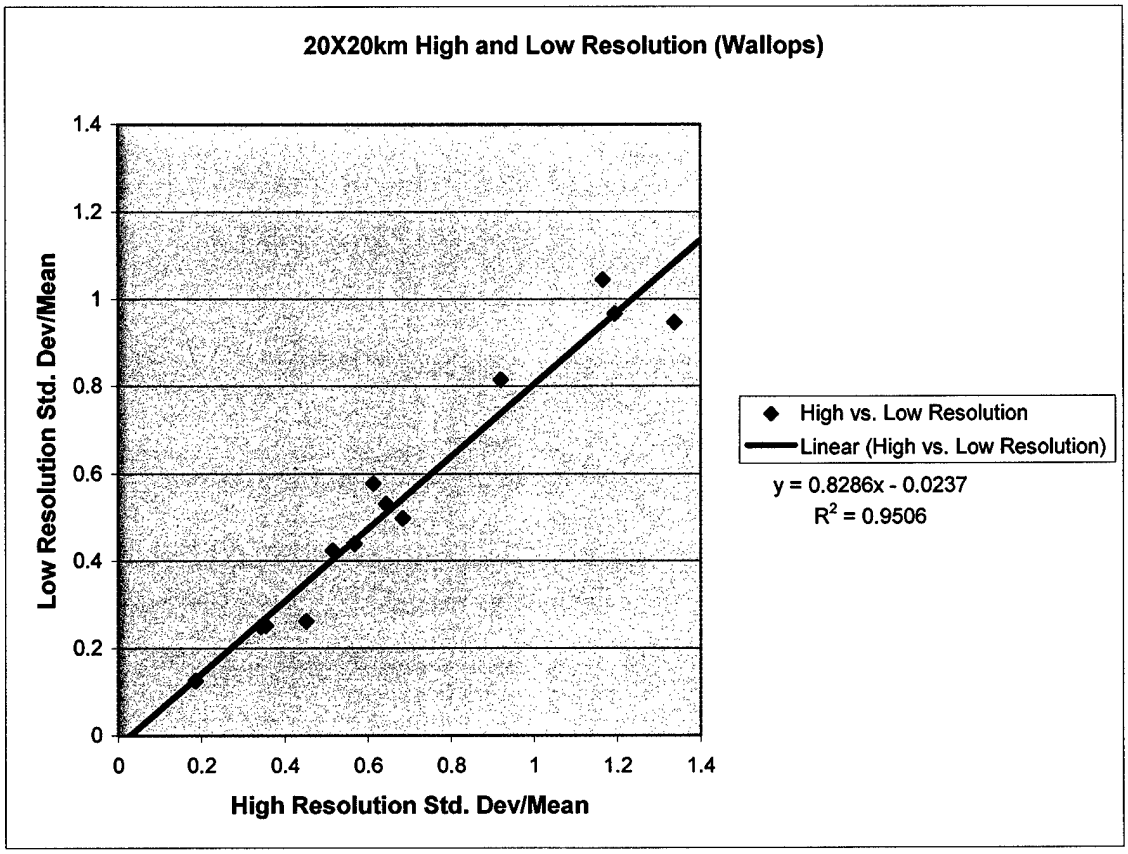

Figure 5.2: Correlation between inhomogeneity parameters calculated at high and low resolution for Wallops Island, March and April 2001.

Figure 5.3 shows the results of adding the Brazilian events to the correlation. The correlation changes slightly, and the root mean square error increases, but the data from both sites do tend to follow the same linear relationship. A number of interesting deductions and questions arise from this plot:

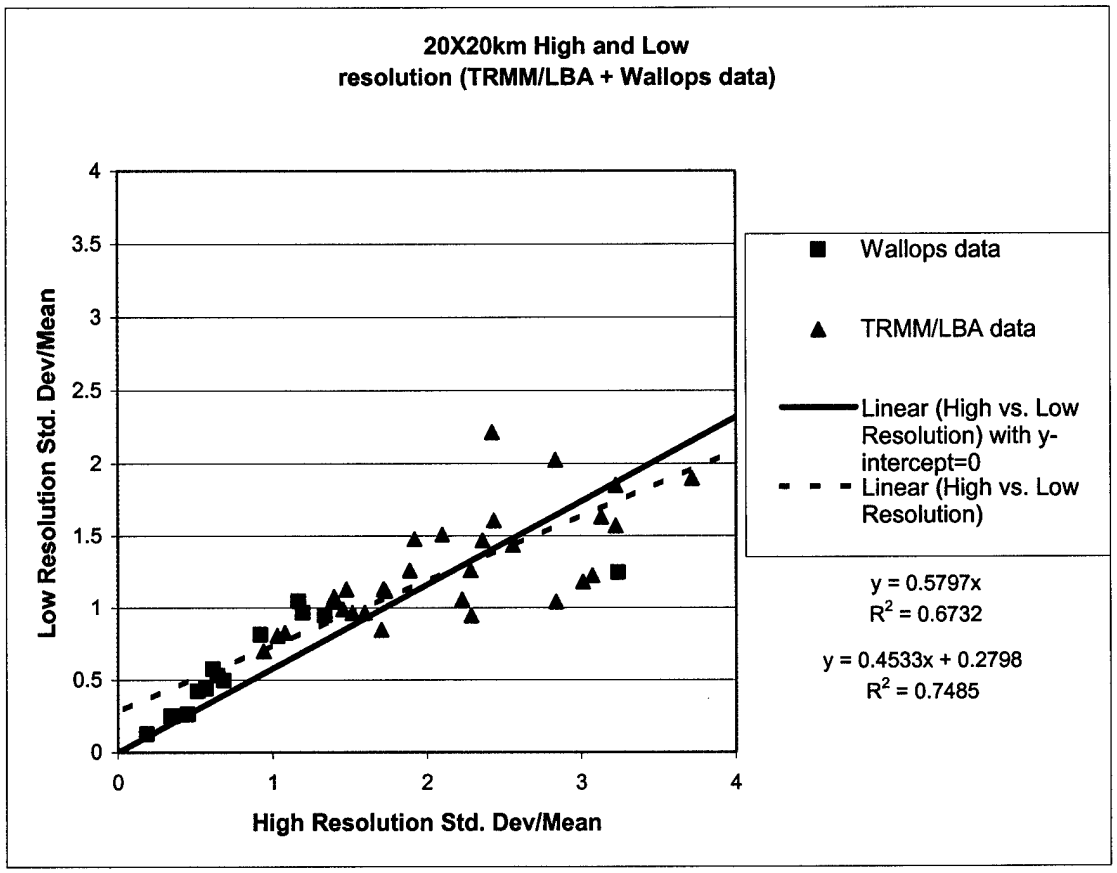

Figure 5.3: Correlation between inhomogeneity parameters calculated at high and low resolutions for Wallops Island, March and April 2001 and TRMM/LBA, January and February 1999.

a) Higher resolution data produces inhomogeneity parameters that are roughly the same as those produced by lower resolution data in areas of high homogeneity.

b) As inhomogeneity increases, lower resolution data underestimates the inhomogeneity parameters by as much as a factor of two. There may be a need for an additional correction factor to account for this sub-4 km inhomogeneity. With that data from such disparate locations yielding similar relationships between high- and low-resolution results, it may be possible to conclude that there may be some sort of global universality in the relationship. Further research would be needed in order to verify whether that idea has any validity.

In summary, at lower inhomogeneities the 4-km resolution data can be used to capture the true inhomogeneity well. Although that becomes less true at higher inhomogeneities, it is possible that a relationship between high- and low-resolution results could be established. If that relationship proves to be universal it may offer the opportunity to apply a simple standard correction to the rainfall estimate that would take into account the full inhomogeneity below the 4 km available from the PR.

Chapter 6

Summary and Conclusions

The accurate measurement of rainfall is necessary to properly deduce the contribution of latent heating to the global energy balance. It is also needed to properly verify the accuracy of GCMs. One of the largest contributors of uncertainty in rainfall estimates has been the beam-filling error, an error that is currently corrected with the use of a globally averaged correction factor. In this study, a climatology was developed of regionally dependent beam-filling corrections over a 42-month period. This climatology was based on beam-filling corrections developed from TRMM PR as a function of mean rain rate and scene inhomogeneity for a 20 by 20 km FOV, for a data set covering three December-January-February time periods over the eastern and western Pacific. A model atmosphere was stipulated that is fairly representative of the tropics. These corrections were then applied to actual TRMM precipitation radar estimates of rain rate and inhomogeneity, and monthly mean corrections were produced in 10 by 10 degree boxes over the TRMM observation region.

A number of issues become apparent upon study of the individual maps. Beam-filling corrections are shown to vary greatly across the globe, both on a spatial and

temporal scale. Values on these maps can vary anywhere from 1 to 2, depending on location and timeframe. Studies have shown that if a particular region were observed over a timeline, there are periods when the TRMM TMI rainfall estimate will be greater than that from the PR and some when it is less. It is possible that some of this bias variability can be accounted for when the variability in beam-filling correction is considered. Figure 6.1 shows the relationship between actual beam-filling corrections and the bias of rain estimated by TMI (using the Wilheit algorithm) relative to the PR. These plots were created using 3-month averages, with a negative NBias corresponding to an underestimation of rainfall by the TMI, and only includes data from the tropics (30N to 30S). In this plot, there appears to be a strong correlation between underestimation by the TMI and the requirement for a beam-filling correction that is higher than the average value of 1.58, and visa versa. Application of beam-filling corrections calculated from the PR to the TMI retrieval may be part of the solution in removing the bias between the TMI and PR. It is obviously not a cure-all though; this correlation breaks down at higher levels of overestimation, leading one to conclude that there are other factors involved as well (for example, details of the transfer function).

Overestimation or underestimation of the passive microwave retrievals led to another concern. The primary precipitation data set used by climatologists comes from the Global Precipitation Climatology Project (GPCP). This data set is compiled using precipitation observations from a variety of sources, including microwave estimates (Huffman et al., 1996). The microwave estimates used come from the SSM/I sensor, which use a Wilheit algorithm over oceans. The microwave data is then used to calibrate a GOES Precipitation Index (GPI) (a technique used to relate IR brightness temperatures

to rainfall amounts), and the microwave and GPI measurements are then combined. This data is then adjusted by rain gauge measurements, where they exist. The use of varying beam-filling corrections in the SSM/I retrievals would change the resulting rainfall estimation from the first step used to create the data set. This could have effects on the final products. The possibility exists that what a climatologist evaluates to be a climate signal may be nothing more than the effect of under- or overestimation of rainfall, first introduced by the microwave retrieval.

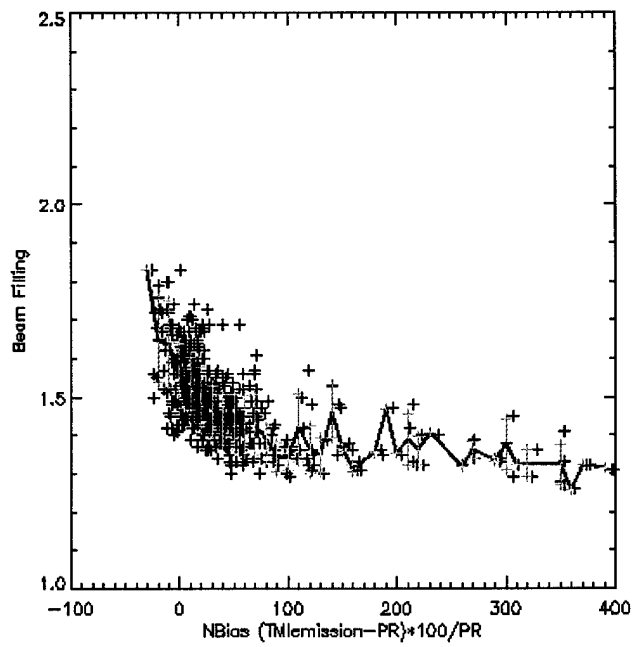

Figure 6.1 Relationship between actual beam-filling corrections and over/underestimation of rainfall by TMI vs. PR.

A simple experiment was conducted to verify how much of a variation in rainfall totals could be introduced by nothing more than the beam-filling correction variability. A rainfall-weighted average beam-filling correction was calculated from 30 N to 30 S for the months of January and May 1999. The resultant beam-filling correction for January was 1.39, while the correction had increased to 1.49 by May. This would indicate a 3.8%

increase in rainfall estimated due to the variation in beam-filling correction. As climate signals are often measured by variations of 5-10%, it would seem that beam-filling correction variability would distort a climatic analysis significantly.

At this point the core issue raised in the introduction should be addressed: does the rainfall variability seen in the observations used by Soden exist? This study only offers a partial answer to that question. Figure 6.2 shows the mean rainfall for the tropics between 20 N and 20 S. It compares the variations seen using the Wilheit algorithm with variations seen when using the new beam-filling corrections. It is obvious at first glance that the curves are similar, and that changing the beam-filling corrections didn't have much of an impact on the rainfall variability. The reason for this can be seen in Figure 6.3, where the impact of beam-filling correction variability is plotted against the effects of rainfall variability. The beam-filling correction may vary the rainfall totals by 3%

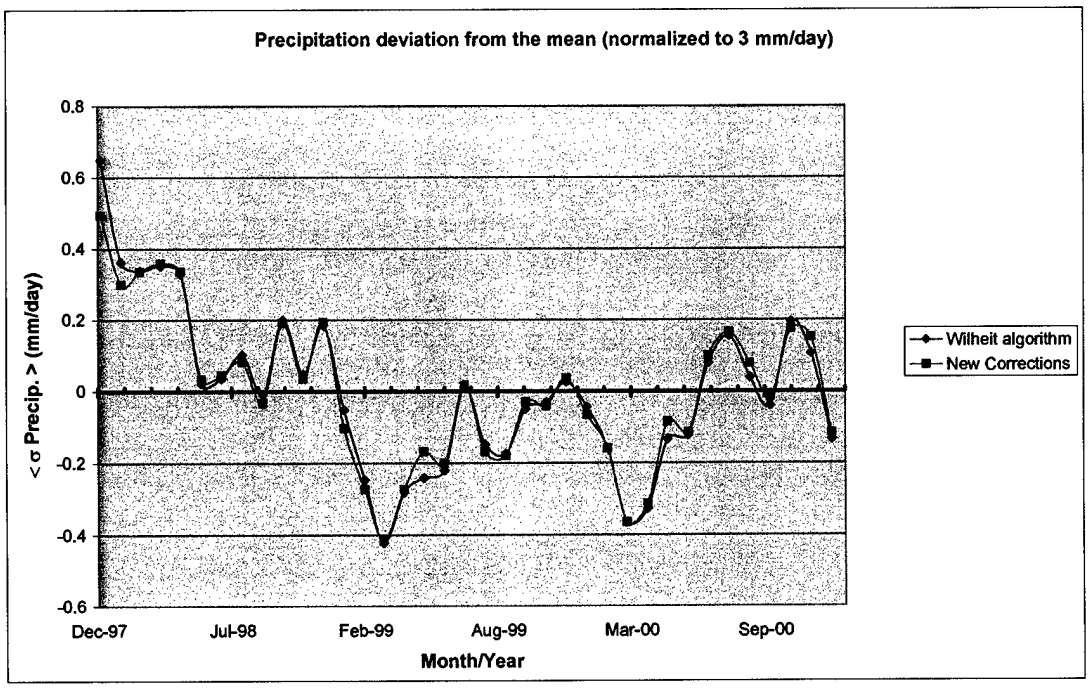

Figure 6.2 Precipitation deviation from the mean (normalized to 3 mm/day).

from month to month, while the overall mean rainfall can vary by 20%. It appears that natural rainfall variations are of a much greater scale than beam-filling variability could affect. This study can therefore conclude that rainfall inhomogeneity cannot cause artificial variation of a sufficient magnitude to force agreement between models and observations.

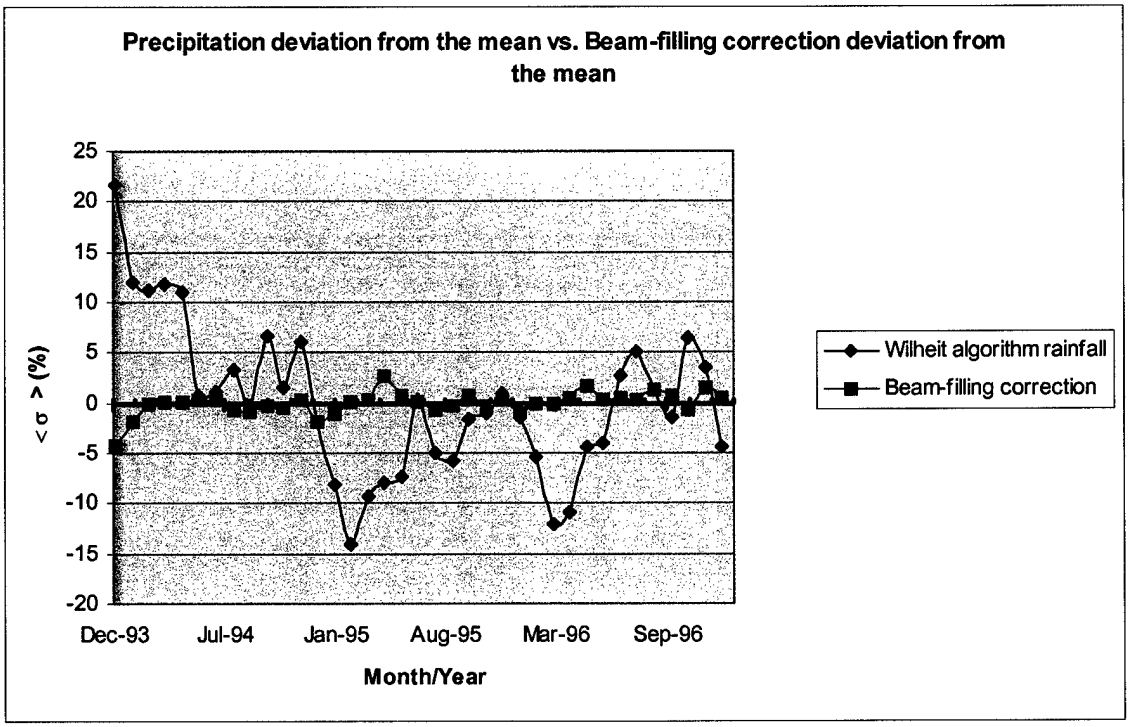

Figure 6.3 Precipitation deviation from the mean vs. Beam-filling correction deviation from the mean (%).

Even though changing the beam-filling corrections may not change rainfall variability from the mean on a global scale, it can affect total rainfall amounts calculated for different regions. For example, mean rainfall totals were calculated for the areas defined as the East and West Pacific in Figure 3.1. Application of the new corrections resulted in a drop in the estimated rainfall total in the West Pacific of about 6% (Figure 6.4). However, application of the new corrections over the East Pacific resulted in a drop of

about 16% (Figure 6.5). Obviously applying the new corrections will have a greater impact in some areas than in others. However, the conclusions that the Wilheit algorithm over-estimates rainfall totals should not be made at this point. If more accurate RTE models and atmospheric simulations were used, and results continued to show that trend, then at that time the statement might be made.

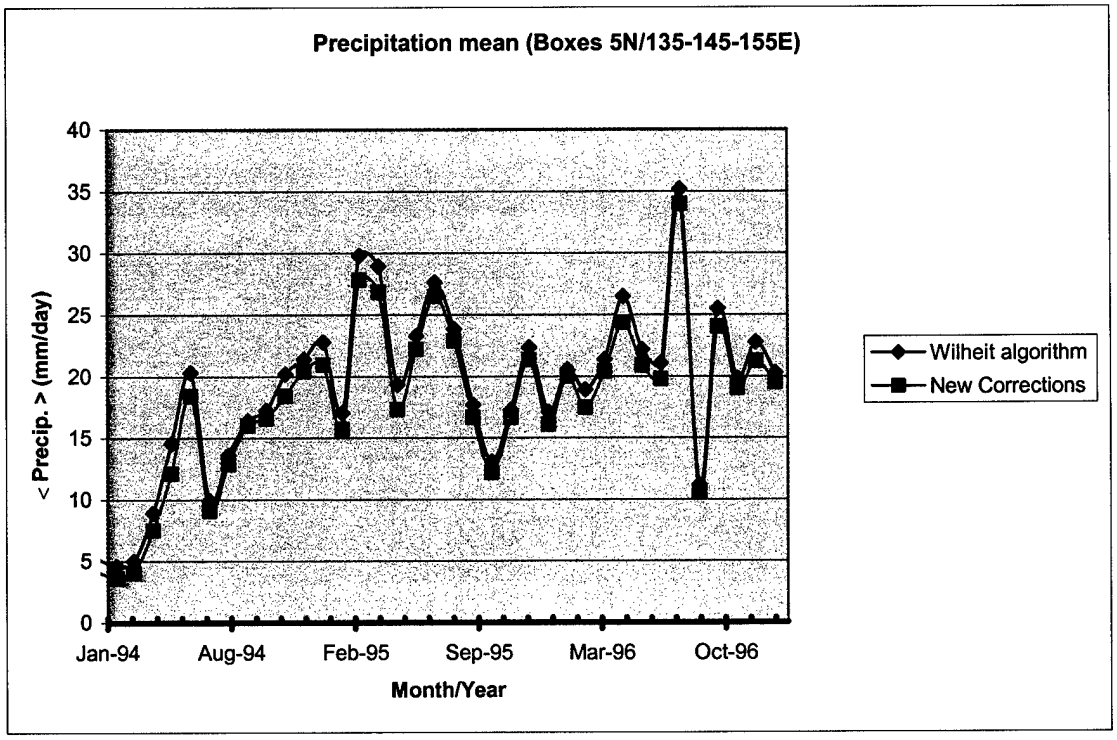

Figure 6.4 West Pacific precipitation mean (mm/day)

The regional variations are the result of the nature of the precipitation in those areas. A first guess would lead one to expect that high beam-filling corrections would occur in areas where highly heterogeneous convective rainfall was occurring, and low beam-filling corrections would occur where stratiform rainfall was occurring. This appears to be the case when a 3-month beam-filling correction map is compared with a convective rain volume fraction map, as shown in Figure 6.6.

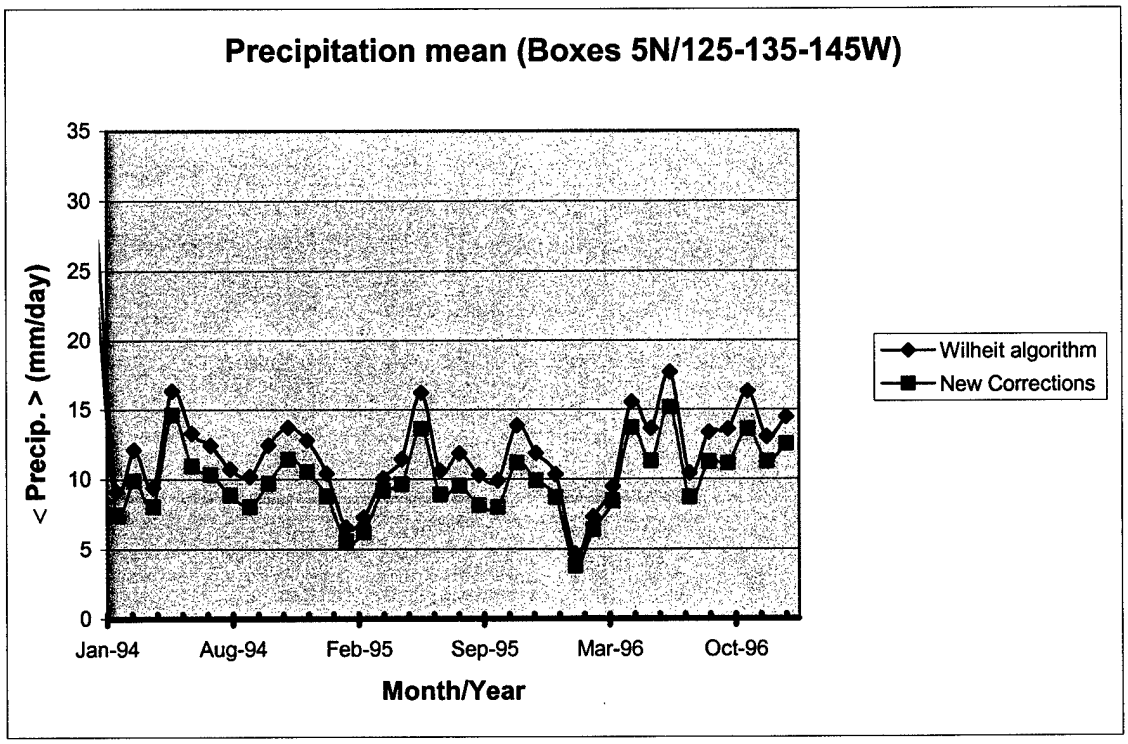

Figure 6.5 East Pacific precipitation mean (mm/day)

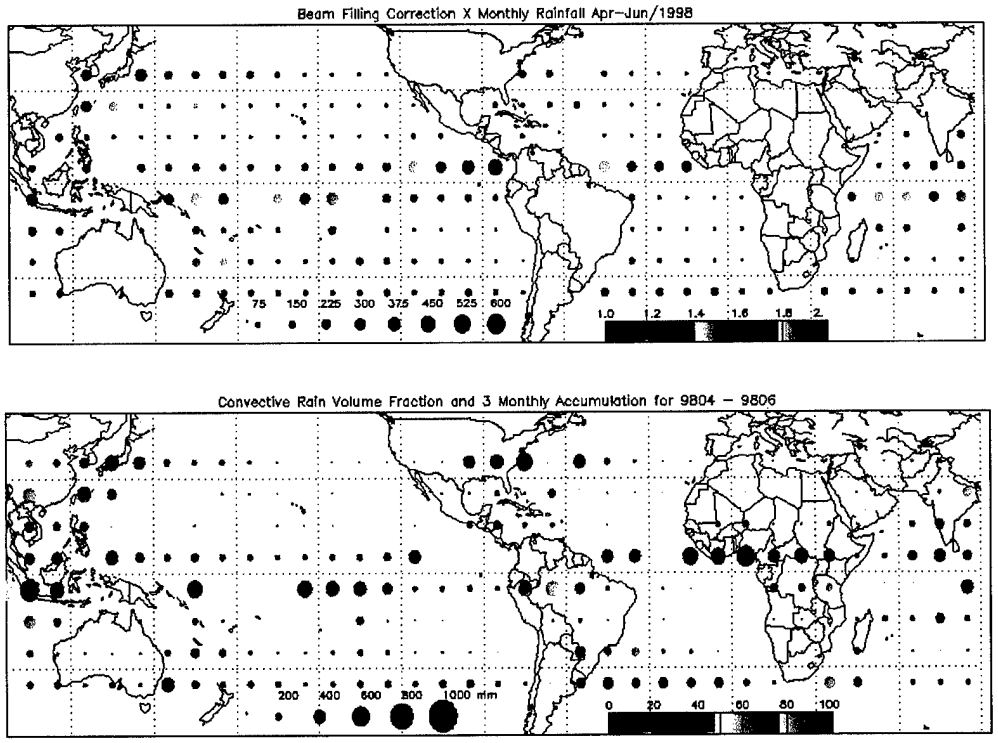

Figure 6.6 Beam-filling correction vs. convective rain fraction for Apr-Jun 1998.

Over the course of this study it became evident that further research could improve the beam-filling corrections beyond what was done here. As stated earlier, beam-filling correction is a function of both FOV and freezing level height. The research done in this study kept both variables constant. Previous research into the variation of beam-filling correction caused by varying the FOV could be used to create a climatology for any FOV. Current research is attempting to use the TRMM PR to estimate freezing levels, using the radar bright band as a proxy. Calculating mean freezing levels on the same scale as the beam-filling corrections would show areas where the corrections should be adjusted. Additional correction factors could be used to adjust the beam-filling correction calculated for a freezing level of 4 km to ones valid for the freezing levels calculated from the PR. This would have its greatest effect on the higher latitude areas of the maps, areas where the freezing level is undoubtedly below that of the model atmosphere used in this study. Previous research would indicate that the beam-filling corrections calculated during this study at the higher latitudes are higher than actual, due to the lower freezing level.

The sensitivity study regarding the correlation between high and low resolution rainfall inhomogeneity also deserves further research. The fact that this correlation remains consistent over two different regions and seasons leads to the possibility that there is some sort of universality in the nature of rainfall inhomogeneity. If the study of other radar locations proves that to be the case, inhomogeneities calculated at low resolutions could be adjusted to compensate for subresolution inhomogeneity. Beam-filling corrections could be recalculated that would take into account inhomogeneity down to the 250 meter scale.

Capturing this level of detail in the inhomogeneity of rainfall could be of great use to hydrologists. The inhomogeneity parameter defined in this study is called the coefficient of variation (CV) in hydrology, and is used to describe spatial inhomogeneity in a way similar to that done here. CV information is used in the development of runoff models, in the classification of rainfall regimes, and in a variety of other applications. Collection of this information has been hampered by the scarcity of rain gauges globally, as well as concern over the accuracy of rainfall measurements from surface radar. If the TRMM PR can be used to infer the CV down to 0.25-km resolution, this problem may be solved. It could provide even greater spatial coverage than that given by surface radar networks, and yet would eliminate one of the major sources of inaccuracy in surface radar measurements (poor or inconsistent calibration of the instrument).

Obviously there are many areas of the rainfall retrieval process that require more study. However, thanks to data available from space-based radar it is now possible to acquire actual measurements of rainfall inhomogeneity. With that information beam-filling corrections can be calculated that will lead to more accurate estimates of rainfall.

Bibliography

Atlas, D., and C. W. Ulbrich, 1978: Path- and area-integrated rainfall measurement by microwave attenuation in the 1-3 cm band. *J. Appl. Meteorol.*, **16**, 1322-1331.

Austin, P. L., and Geotis, S. G., 1978: Evaluation of the quality of precipitation data from a satellite-borne radiometer. *Final report under NASA Grant NSG 5024*, Massachusetts Institute of Technology, Cambridge, MA.

Bell, T. L., A. Abdullah, R. L. Martin, and G. R. North, 1990: Sampling errors for satellite-derived tropical rainfall: Monte Carlo study using a space-time stochastic model. *J. Geophys. Res.*, **95**, 2195-2206.

Chandrasekhar, S., 1960: Radiative Transfer. Dover Publications, New York, 393pp.

Chui, L. S., G. R. North, D. A. Short, and A. McConnell, 1990: Rain estimation from satellites: Effects of finite field of view. *J. Geophys. Res.*, **95**, 2177-2185.

Foot, C. B., and P. S. duToit, 1969: Terminal velocity of raindrops aloft. *J. Appl. Meteorol.*, **8**, 249-253.

Gunn, K. L. S., and T. U. R. East, 1954: The microwave properties of precipitation particles. *Quart. J. Royal Met. Soc.*, **80**, 522-545.

Hollinger, J. P., J. L. Pierce, and G. A. Poe, 1990: SSM/I instrument evaluation. *IEEE Trans. Geosci. Rem. Sens.*, **GE-28**, 781-790.

Huffman, G.J., R.F. Adler, P. Arkin, A. Chang, R. Ferraro, A. Gruber, J. Janowiak, A. McNab, B. Rudolf, and U. Schneider, 1996: The global precipitation climatology project (GPCP) combined precipitation data set. *Bull. Amer. Meteor. Soc.*, **78**, 5-20.

Intergovernmental Panel on Climate Change (IPCC), 2001: Climate Change 2001: The Scientific Basis, http://www.ipcc.ch/spm22-01.pdf, 3.

Jackson, J. D., 1962: Classical Electrodynamics. John Wiley and Sons Inc., New York, pp. 216-220.

Jung, H. J., 1980: The determination of rainfall rates from satellite measurements of the thermal microwave emission. *Contrib. Atmos. Phys.*, **53**, 366-388.

Kummerow, C., 1993: Radiative Transfer Model Comparisons for Passive Microwave Frequencies. *J. Geophys. Res.*, **98**, 2757-2765.

Kummerow, C., 1998: Beamfilling Errors in Passive Microwave Rainfall Retrievals. *J. of Appl. Meteor.*, **37**, 356-370.

Kummerow, C., and L. Giglio, 1994: A Passive Microwave Technique for Estimating Rainfall and Vertical Structure Information from Space, Part I: Algorithm Description. *J. Appl. Meteorol.*, **33**, 3-18.

Kummerow, C., R. A. Mack and I. M. Hakkarinen, 1989: A self-consistency approach to improve microwave rainfall estimates from space. *J. of Appl. Meteor.*, **28**, 869-884.

Marshall, J. S., and W. M. Palmer, 1948: The distribution of raindrops with size. *J. Meteor.*, **5**, 165-166.

Mie, G., 1908: Beiträge zur Optik Trüber Medien, speziell kolloidaler Metalösungen. *Ann. Phys.*, **26**, 597-614.

Mugnai, A., E. A. Smith, and G. J. Tripoli, 1993: Foundation of physical-statistical precipitation retrieval from passive microwave satellite measurements. Part II: Emission source and generalized weighting function properties of a time dependent cloud-radiation model. *J. Appl. Meteor.*, **32**, 17-39.

Olson, W. S., 1989: Physical retrieval of rainfall rates over the ocean by multispectral radiometry: Application to tropical cyclones. *J. Geophys. Res.*, **94**, 2267-2280.

Roberti, L., J. Haferman and C. Kummerow, 1994: Microwave Radiative Transfer Through Horizontally Inhomogeneous Precipitating Clouds. *J. Geophys. Res.*, **99**, 16707-16718.

Rodgers, E. B., H. Siddalingaiah, A. T. C. Chang, and T. T. Wilheit, 1979: A statistical technique for determining rainfall over land emplying Nimbus 6 ESMR measurements. *J. Appl. Meteorol.*, **18**, 978-991.

Soden, B. J., 2000: The sensitivity of the tropical hydrologic cycle to ENSO, *J. Climate*, **13**, 538-549.

Smith, E. A., X. Xiang, A. Mugnai, and G. Tripoli, 1994: Design of an inversion-based precipitation profile retrieval algorithm using an explicit cloud model for initial guess microphysics. *Meteorol. Atmos. Phys.*, **54**.

Wang, S., A., 1996: Modeling the beamfilling correction for microwave retrieval of oceanic rainfall; Ph.D. Thesis, Department of Meteorology, Texas A&M University.

Weinman, J. A., and P. J. Guetter, 1977: Determination of rainfall distributions from microwave radiation measured by the Nimbus 6 ESMR. *J. Appl. Meteorol.*, **16**, 437-442.

Wilheit, T. T., 1986: Some comments on passive microwave measurement of rain. *Bull. Amer. Meteor.*, **67**, 1226-1232.

Wilheit, T. T., A. T. C. Chang, M. S. V. Rao, E. B. Rodgers, and J. S. Theon, 1977: A satellite technique for quantitatively mapping rainfall rates over the ocean. *J. Appl. Meteor.*, **16**, 551-560.

Wilheit, T. T., A.T.C. Chang and L.S. Chiu, 1991: Retrieval of monthly rainfall indices from microwave radiometric measurement using probability distribution functions. *J. Atmos. Oceanic. Technol.*, **8**, 118-136.

Wu, R., and J. S. Weinman, 1984: Microwave radiances from precipitating clouds containing aspherical ice, combined phase, and liquid hydrometeors. *J. Geophys. Res.*, **89**, 7170-7178.

Appendix A

Monthly Beam-filling Correction Maps

This appendix contains beam-filling correction vs. total rainfall maps broken down by month from January 1998 through August 2001. Each map can be read in the same manner as the 3-month composite maps seen in Chapter 4.

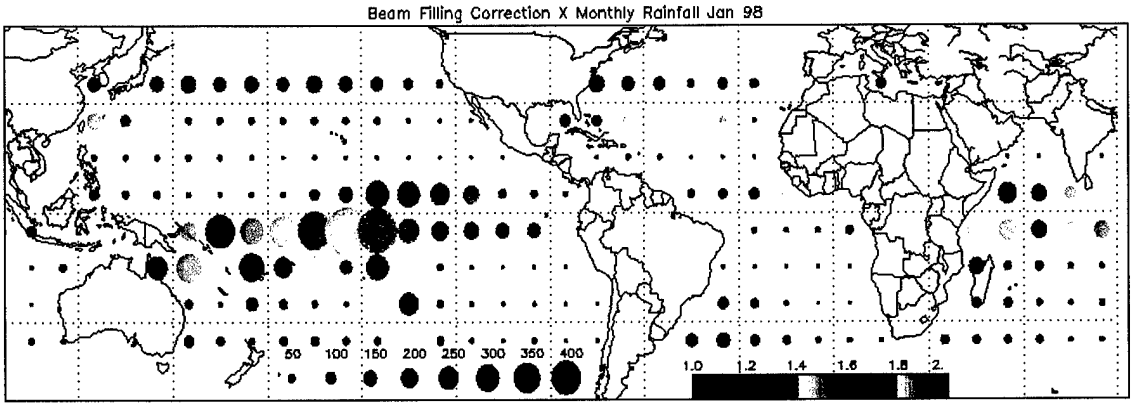

Figure A.1: January 1998 beam-filling correction (color) and total rainfall in mm (circle size).

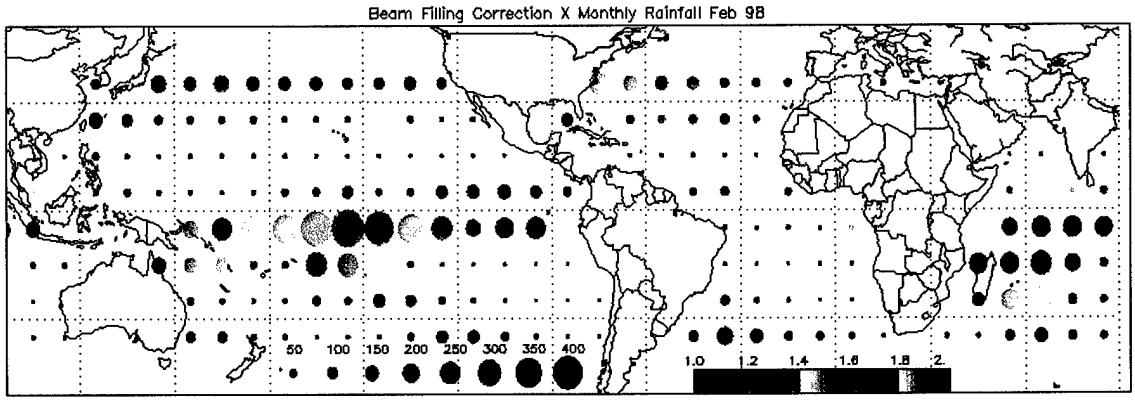

Figure A.2: February 1998 beam-filling correction (color) and total rainfall in mm (circle size).

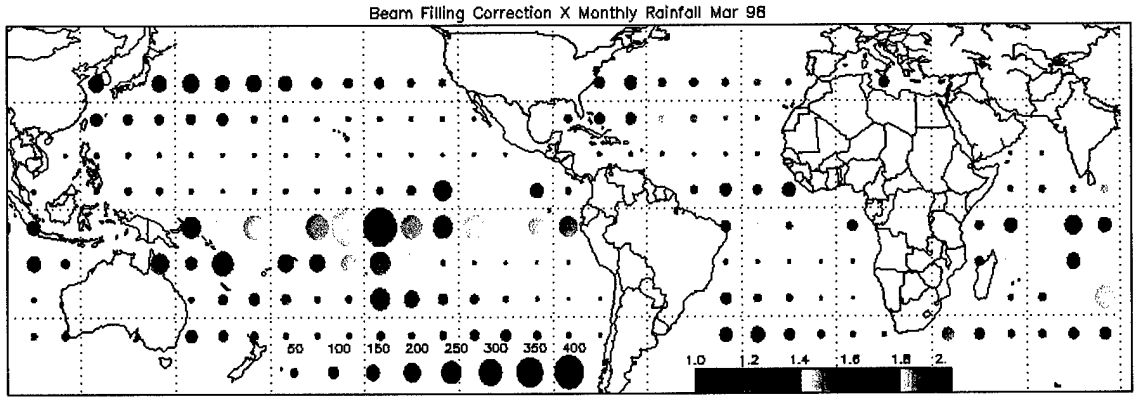

Figure A.3: March 1998 beam-filling correction (color) and total rainfall in mm (circle size).

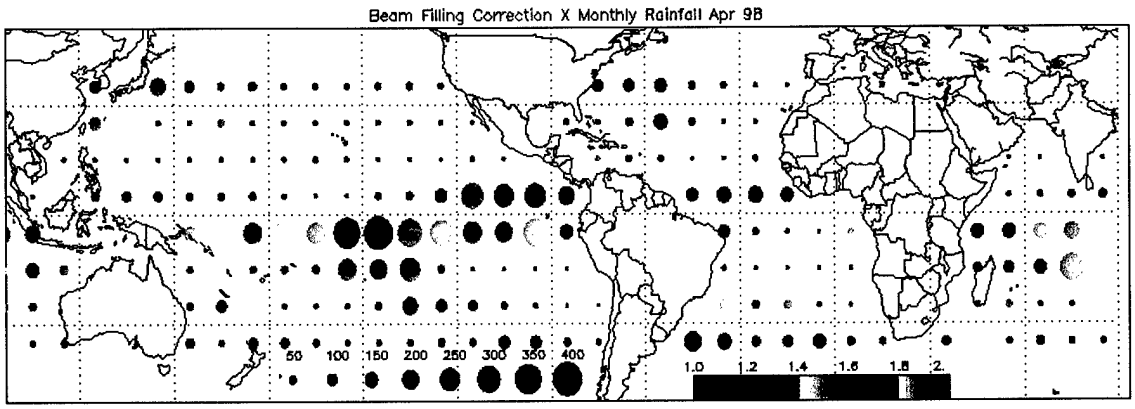

Figure A.4: April 1998 beam-filling correction (color) and total rainfall in mm (circle size).

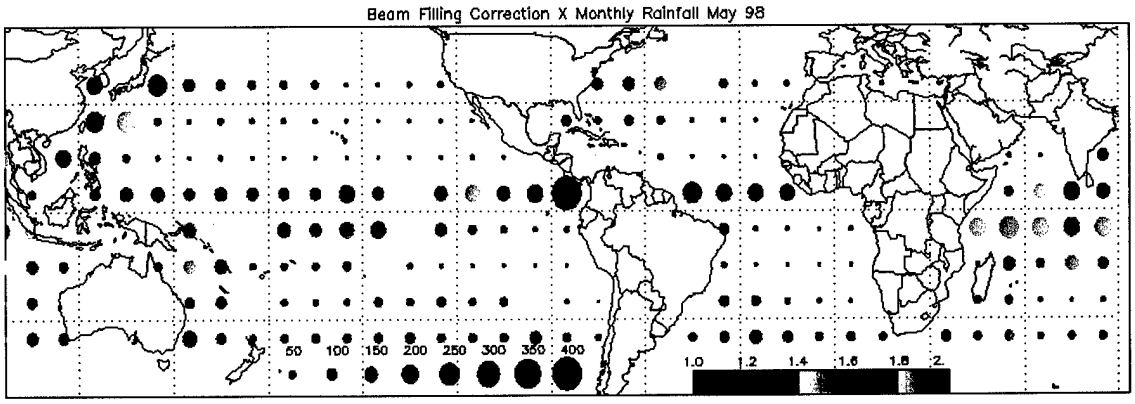

Figure A.5: May 1998 beam-filling correction (color) and total rainfall in mm (circle size).

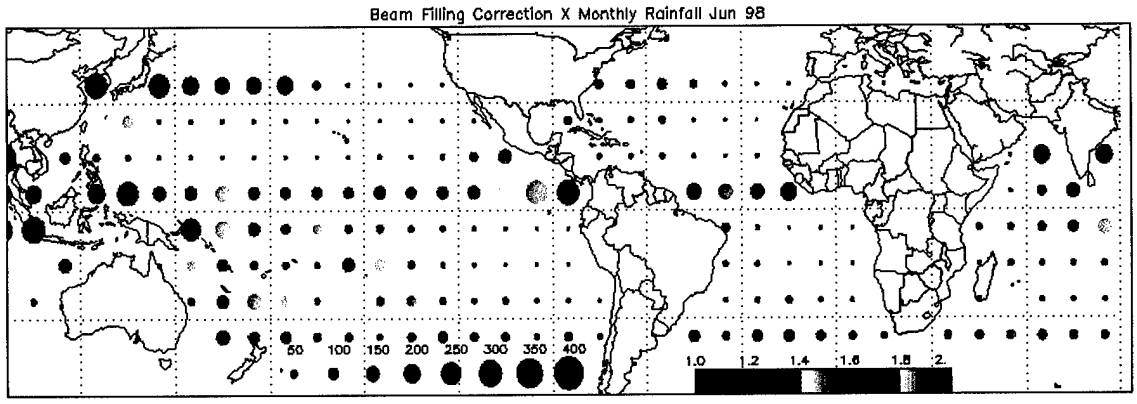

Figure A.6: June 1998 beam-filling correction (color) and total rainfall in mm (circle size).

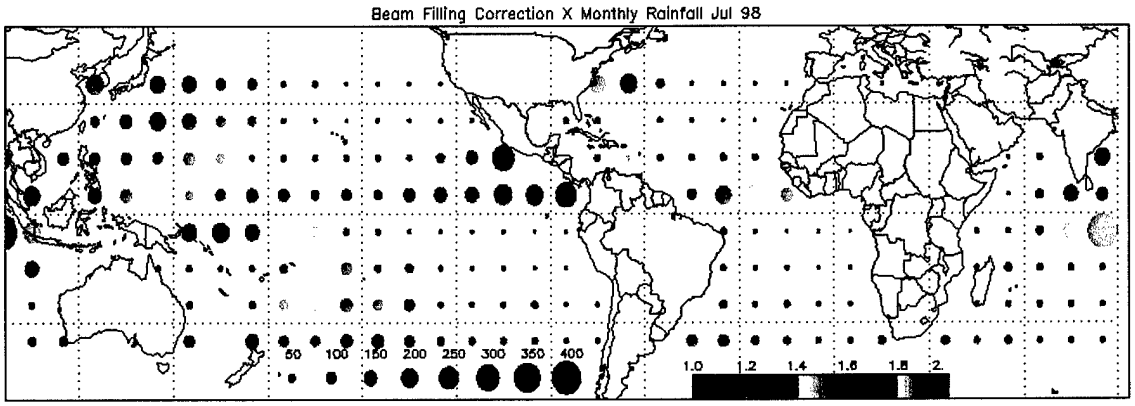

Figure A.7: July 1998 beam-filling correction (color) and total rainfall in mm (circle size).

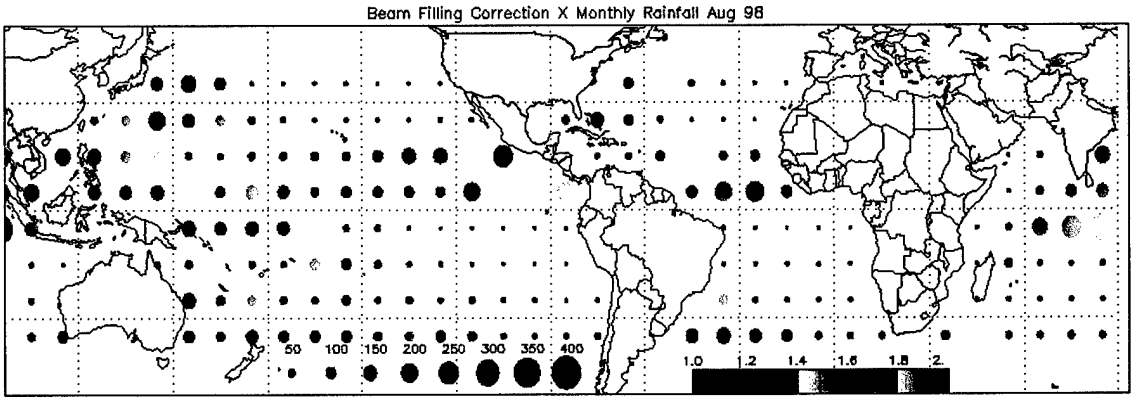

Figure A.8: August 1998 beam-filling correction (color) and total rainfall in mm (circle size).

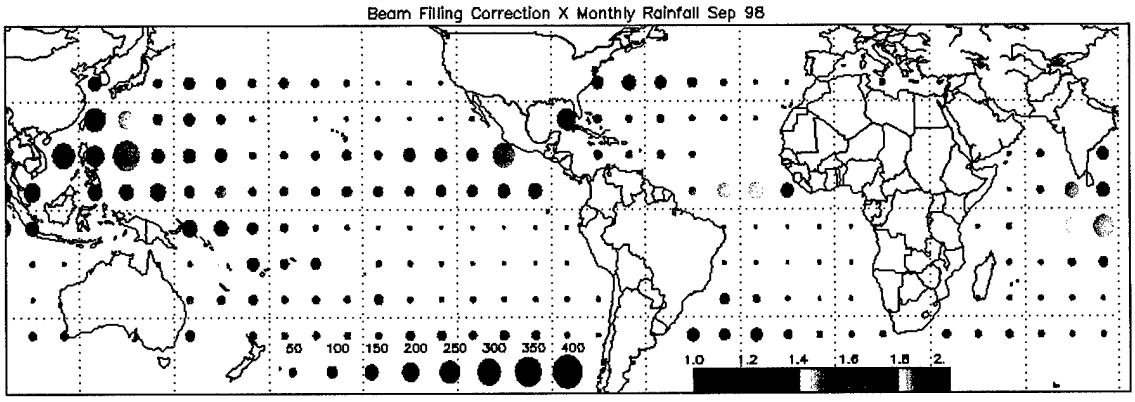

Figure A.9: September 1998 beam-filling correction (color) and total rainfall in mm (circle size).

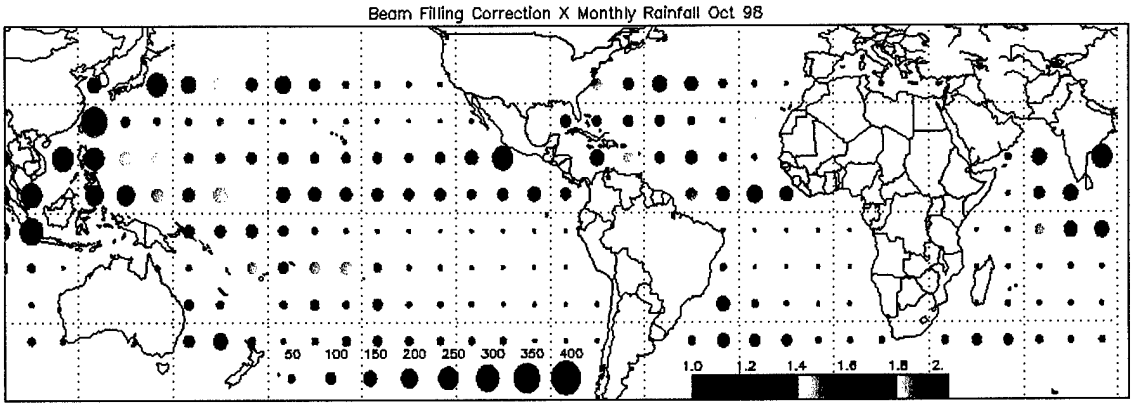

Figure A.10: October 1998 beam-filling correction (color) and total rainfall in mm (circle size).

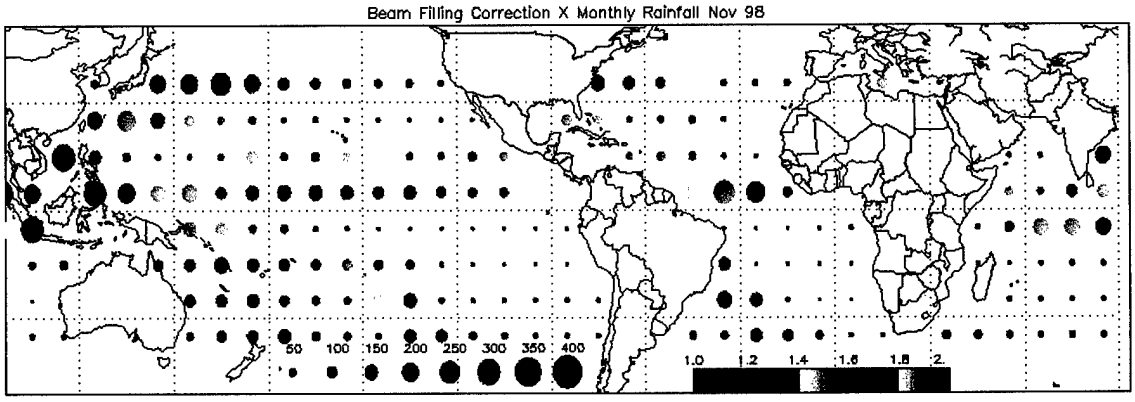

Figure A.11: November 1998 beam-filling correction (color) and total rainfall in mm (circle size).

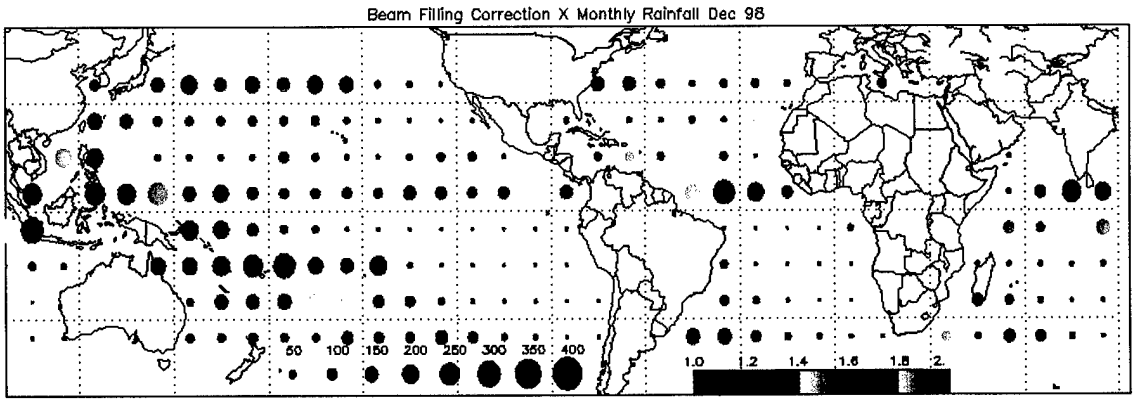

Figure A.12: December 1998 beam-filling correction (color) and total rainfall in mm (circle size).

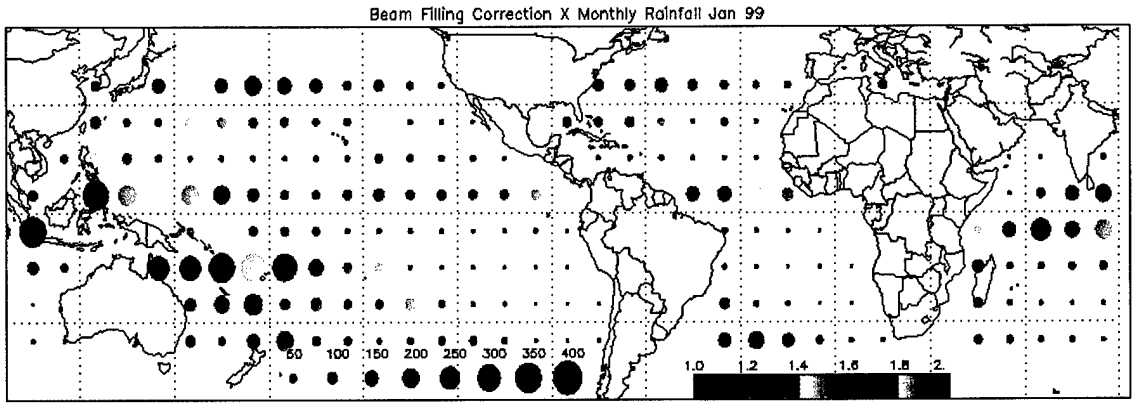

Figure A.13: January 1999 beam-filling correction (color) and total rainfall in mm (circle size).

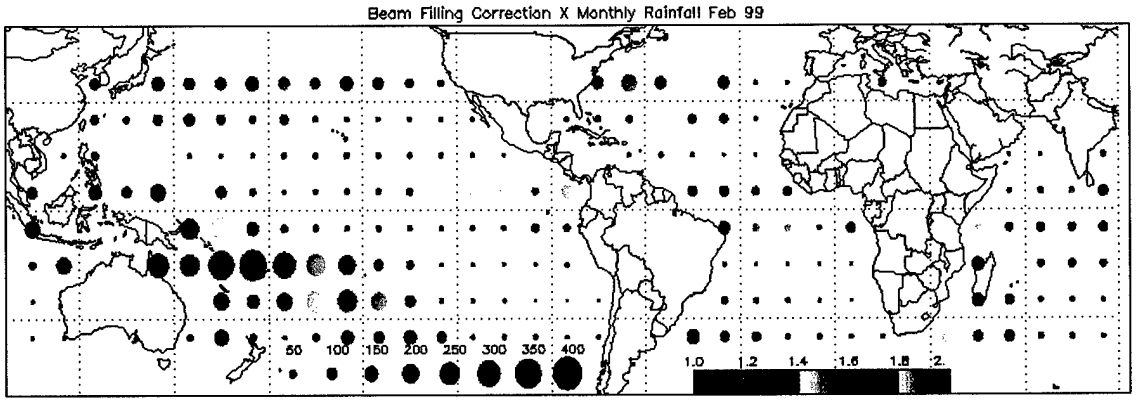

Figure A.14: February 1999 beam-filling correction (color) and total rainfall in mm (circle size).

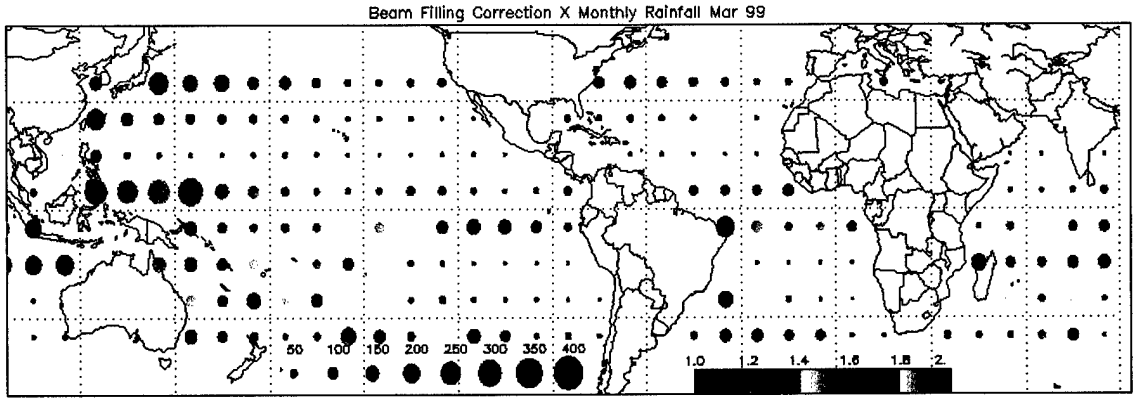

Figure A.15: March 1999 beam-filling correction (color) and total rainfall in mm (circle size).

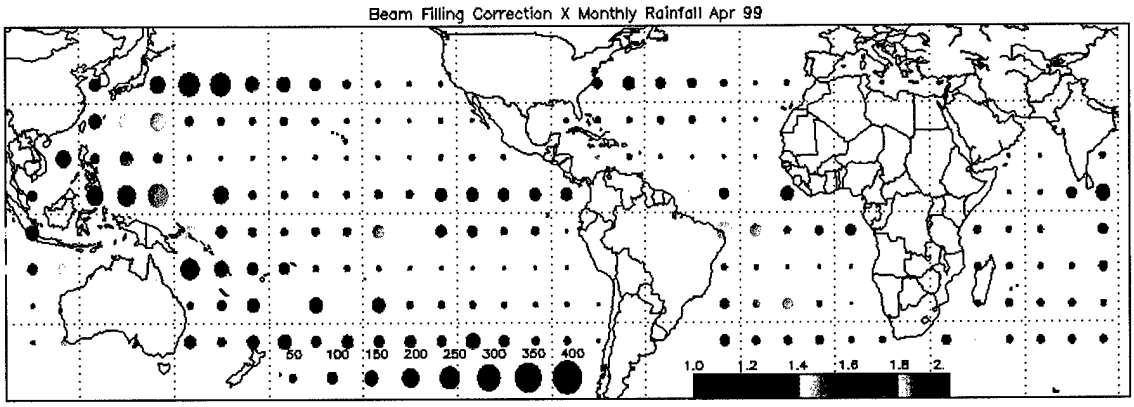

Figure A.16: April 1999 beam-filling correction (color) and total rainfall in mm (circle size).

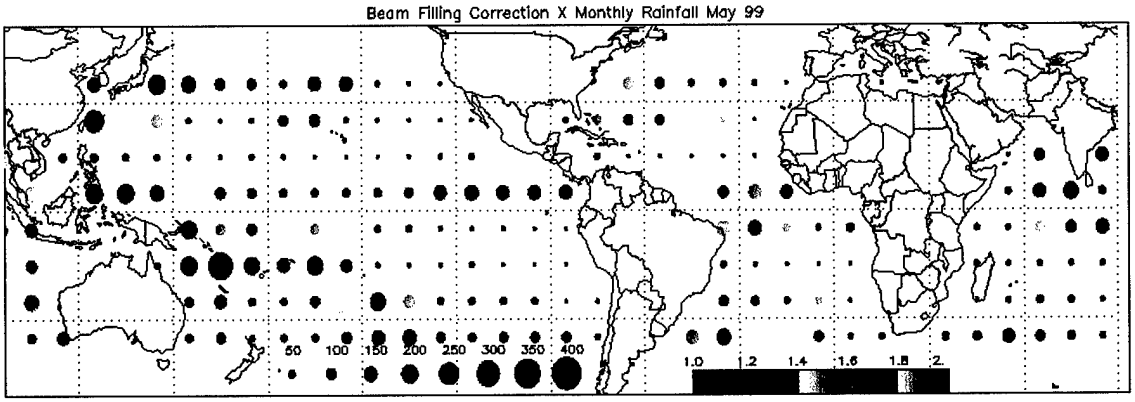

Figure A.17: May 1999 beam-filling correction (color) and total rainfall in mm (circle size).

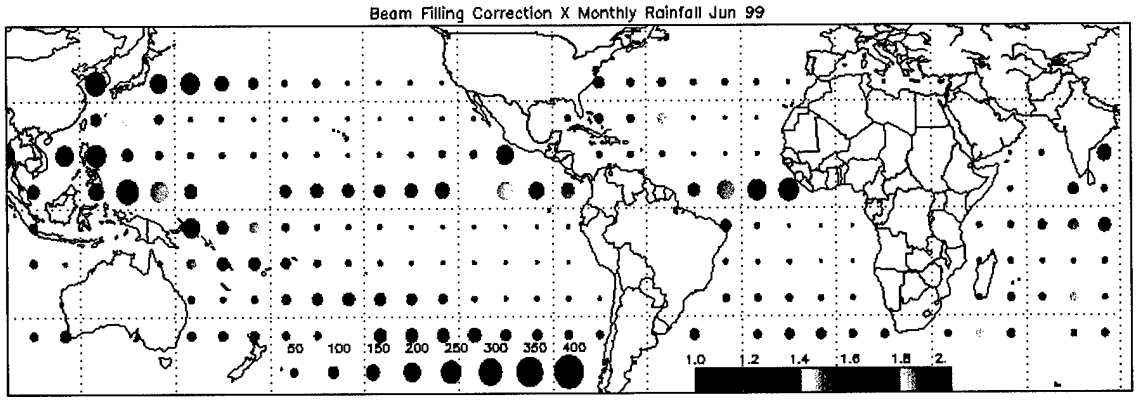

Figure A.18: June 1999 beam-filling correction (color) and total rainfall in mm (circle size).

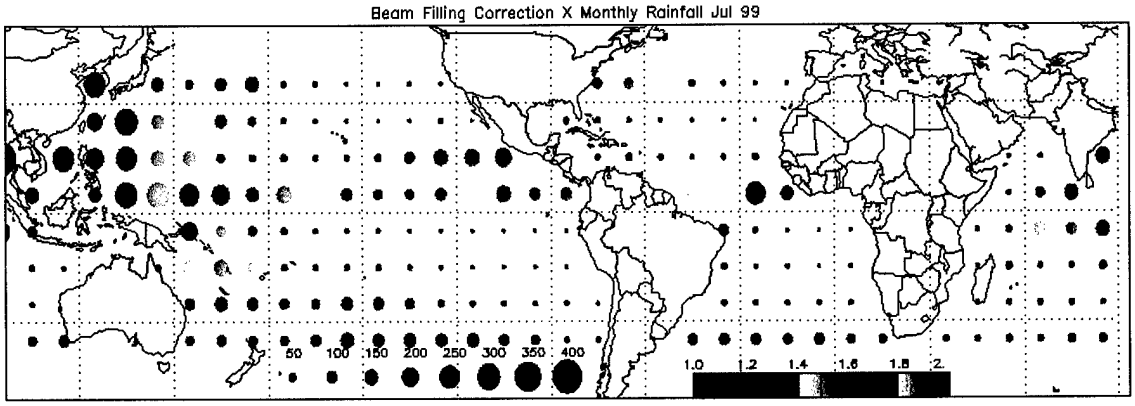

Figure A.19: July 1999 beam-filling correction (color) and total rainfall in mm (circle size).

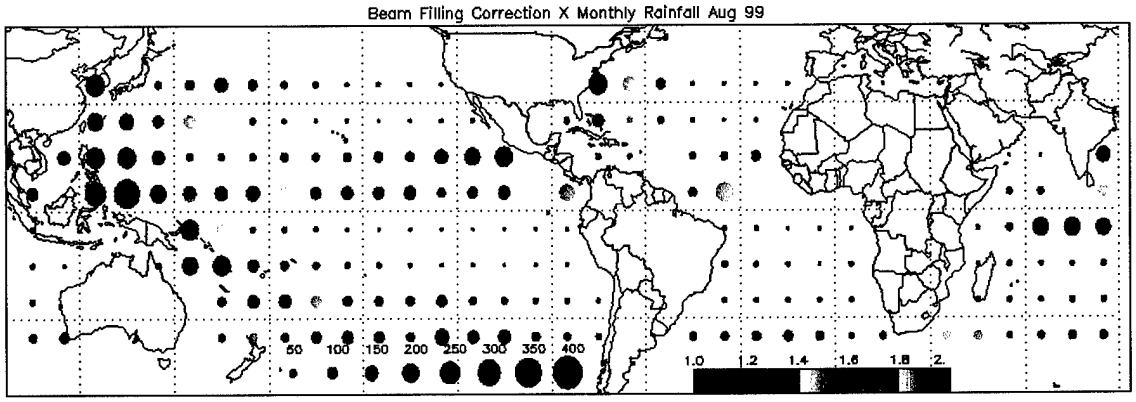

Figure A.20: August 1999 beam-filling correction (color) and total rainfall in mm (circle size).

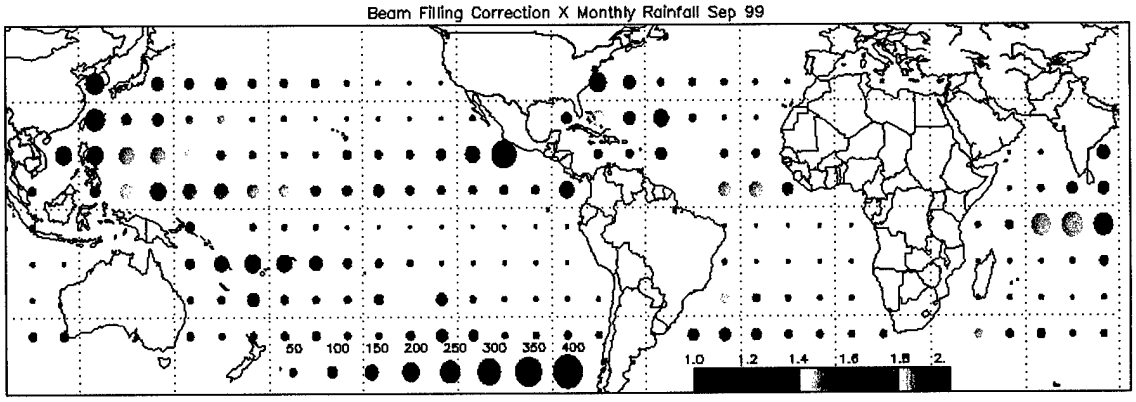

Figure A.21: September 1999 beam-filling correction (color) and total rainfall in mm (circle size).

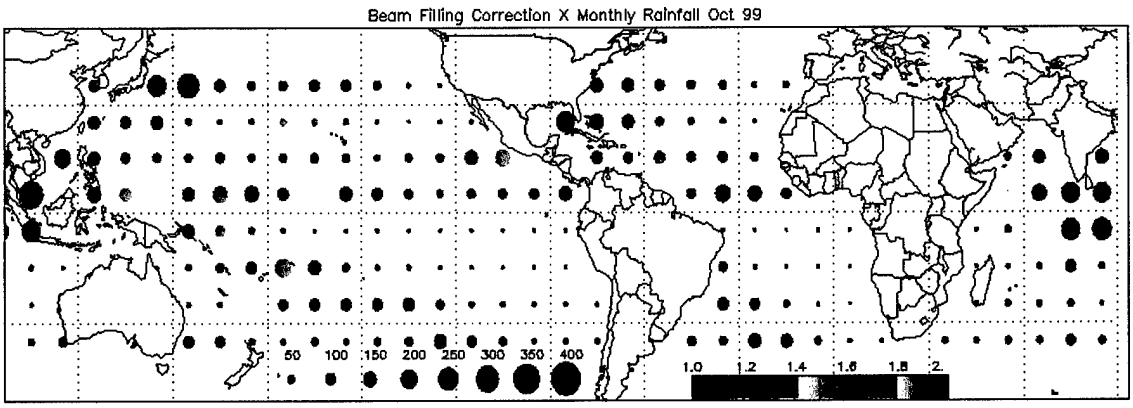

Figure A.22: October 1999 beam-filling correction (color) and total rainfall in mm (circle size).

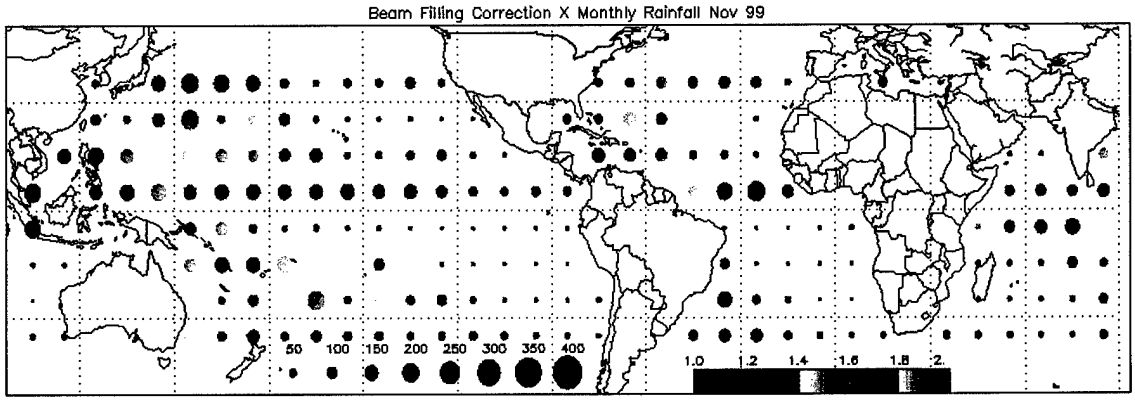

Figure A.23: November 1999 beam-filling correction (color) and total rainfall in mm (circle size).

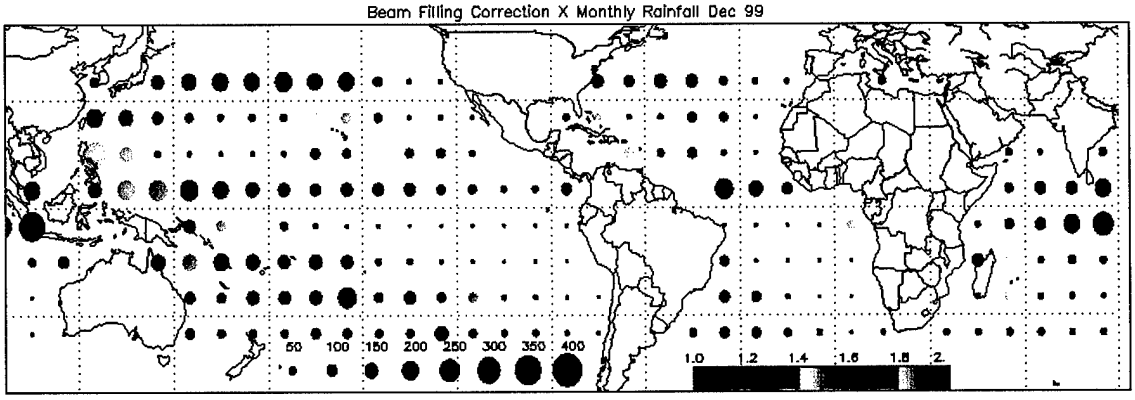

Figure A.24: December 1999 beam-filling correction (color) and total rainfall in mm (circle size).

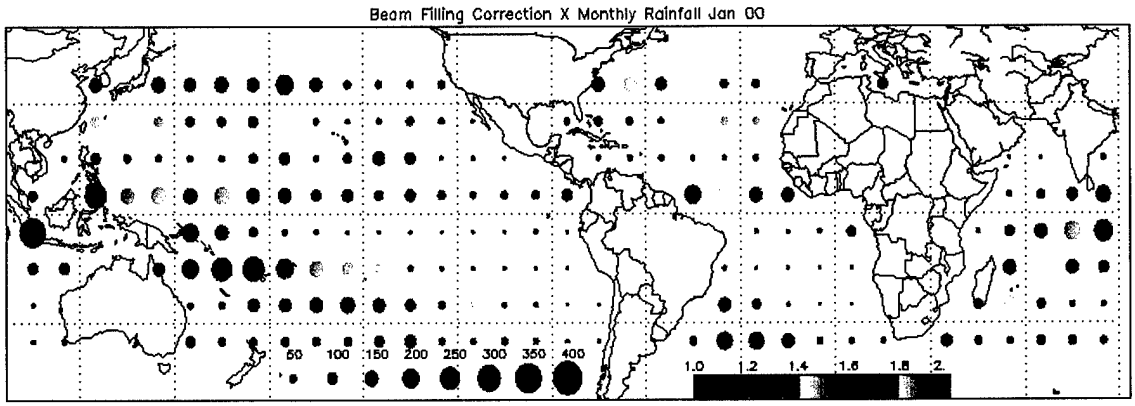

Figure A.25: January 2000 beam-filling correction (color) and total rainfall in mm (circle size).

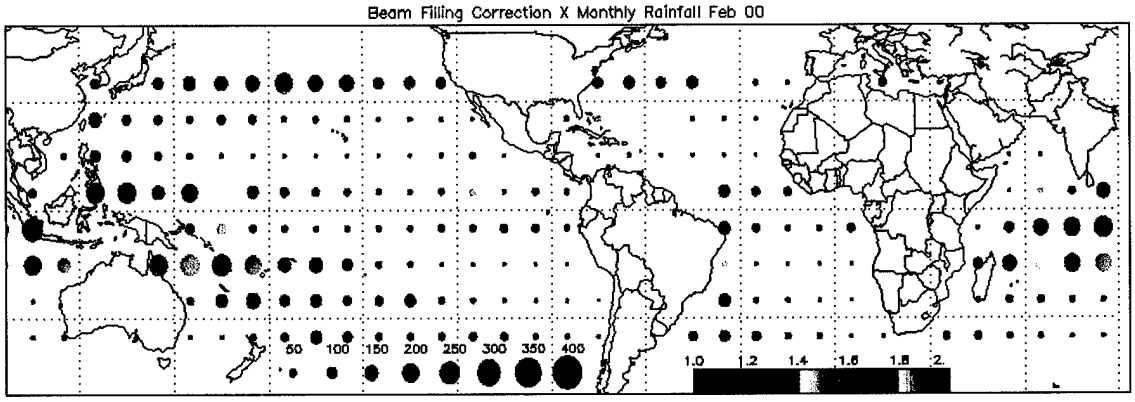

Figure A.26: February 2000 beam-filling correction (color) and total rainfall in mm (circle size).

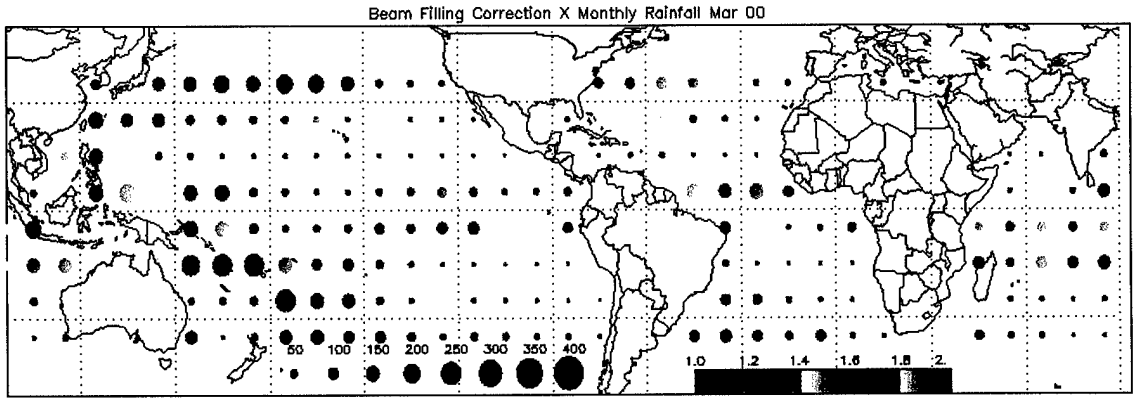

Figure A.27: March 2000 beam-filling correction (color) and total rainfall in mm (circle size).

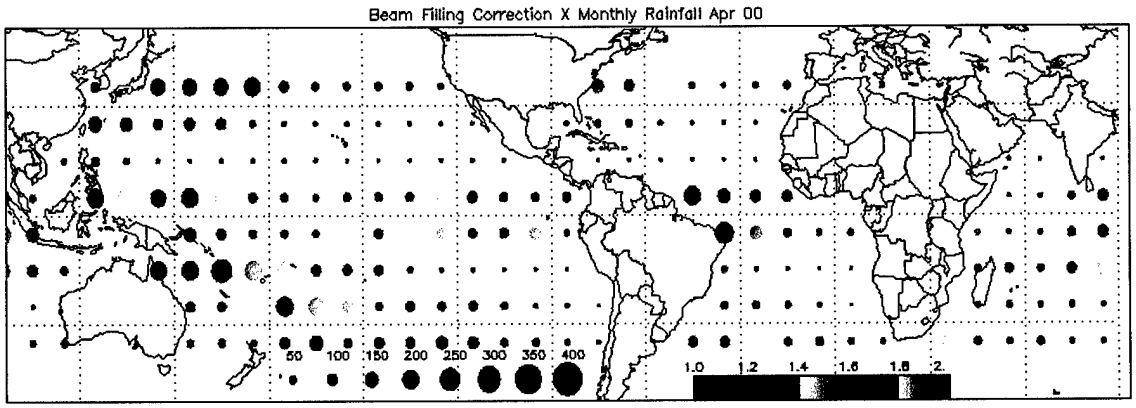

Figure A.28: April 2000 beam-filling correction (color) and total rainfall in mm (circle size).

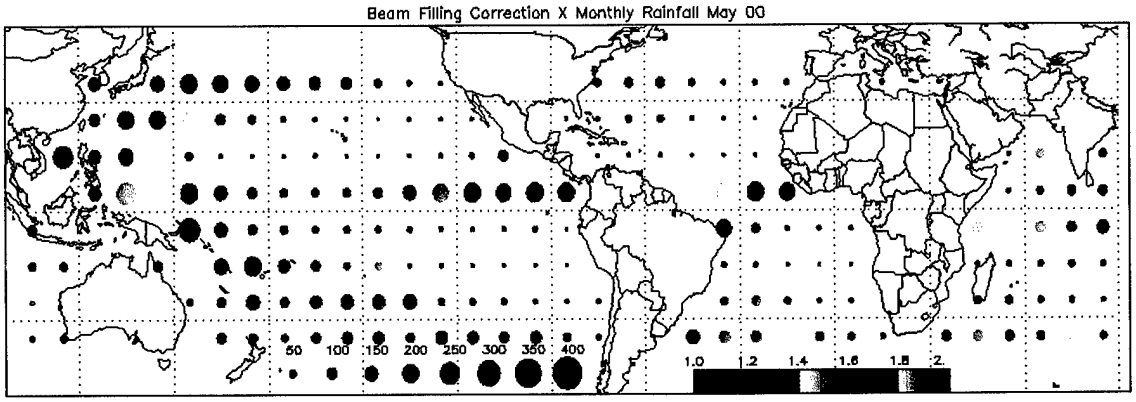

Figure A.29: May 2000 beam-filling correction (color) and total rainfall in mm (circle size).

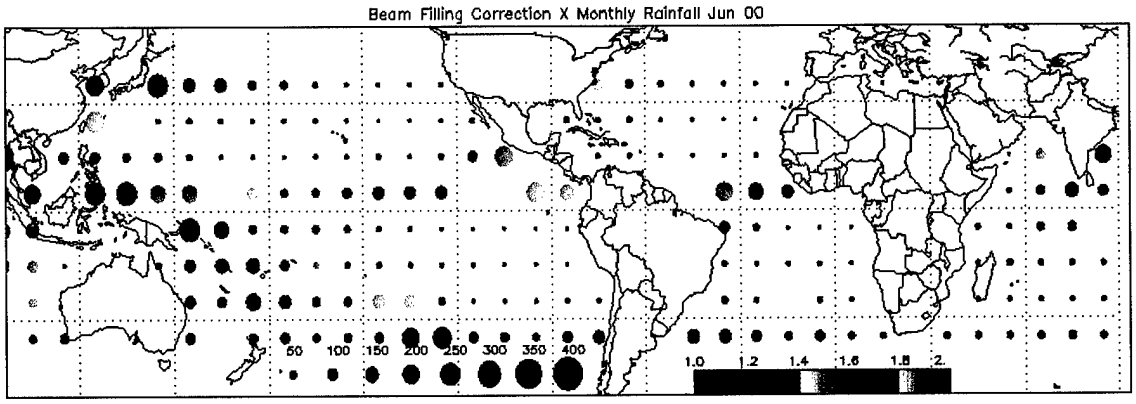

Figure A.30: June 2000 beam-filling correction (color) and total rainfall in mm (circle size).

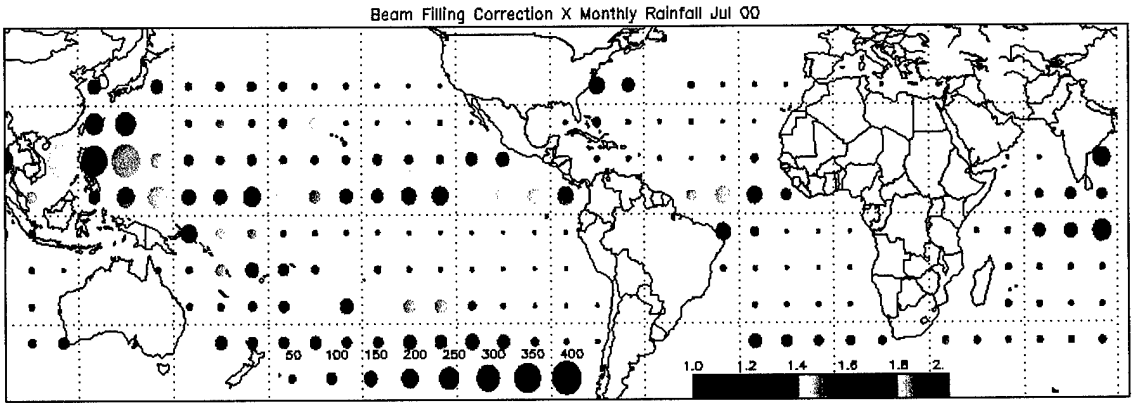

Figure A.31: July 2000 beam-filling correction (color) and total rainfall in mm (circle size).

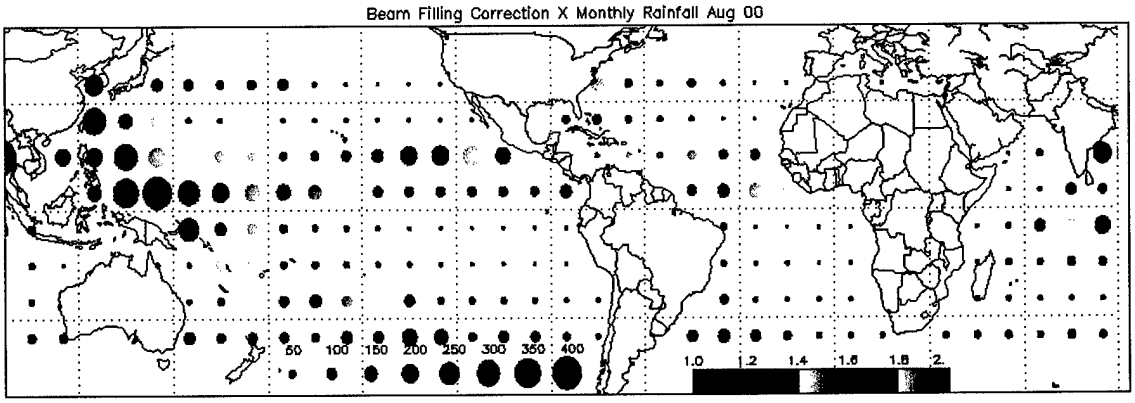

Figure A.32: August 2000 beam-filling correction (color) and total rainfall in mm (circle size).

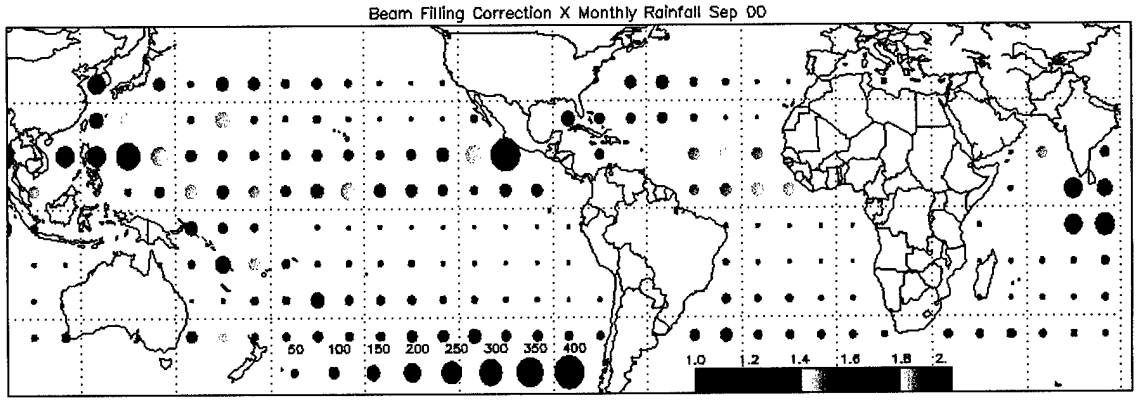

Figure A.33: September 2000 beam-filling correction (color) and total rainfall in mm (circle size).

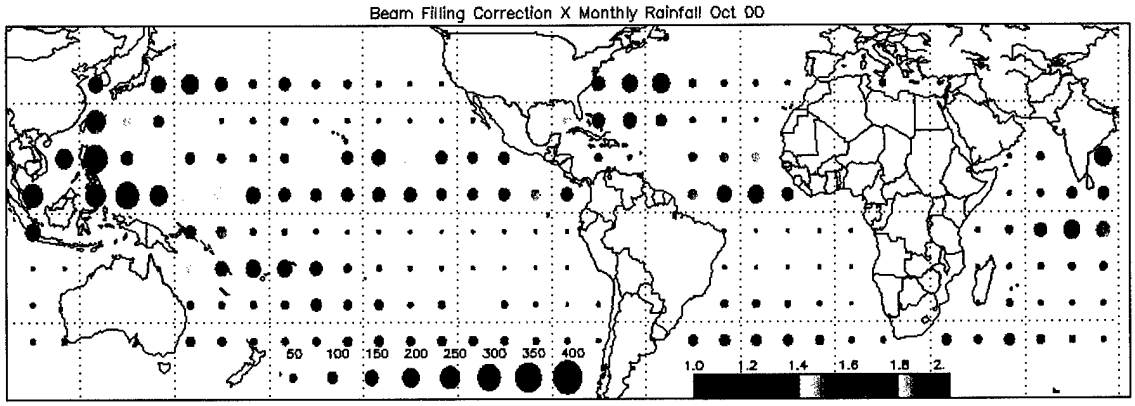

Figure A.34: October 2000 beam-filling correction (color) and total rainfall in mm (circle size).

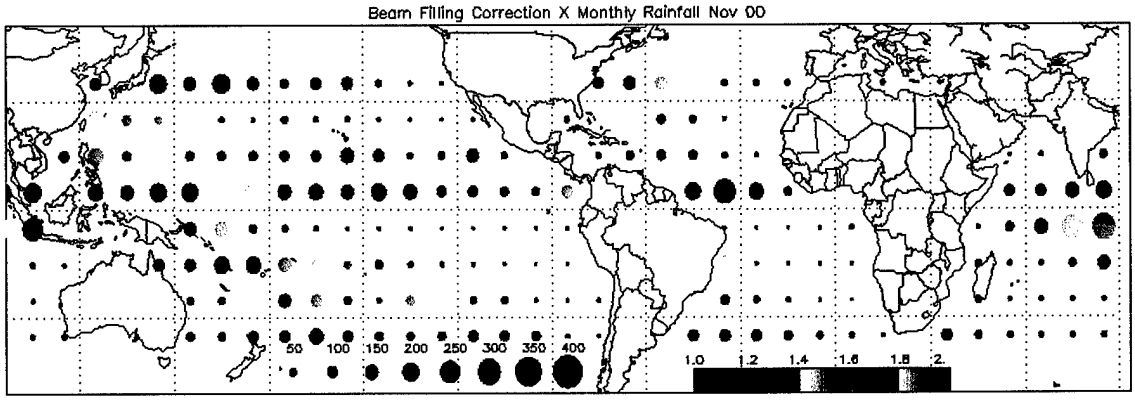

Figure A.35: November 2000 beam-filling correction (color) and total rainfall in mm (circle size).

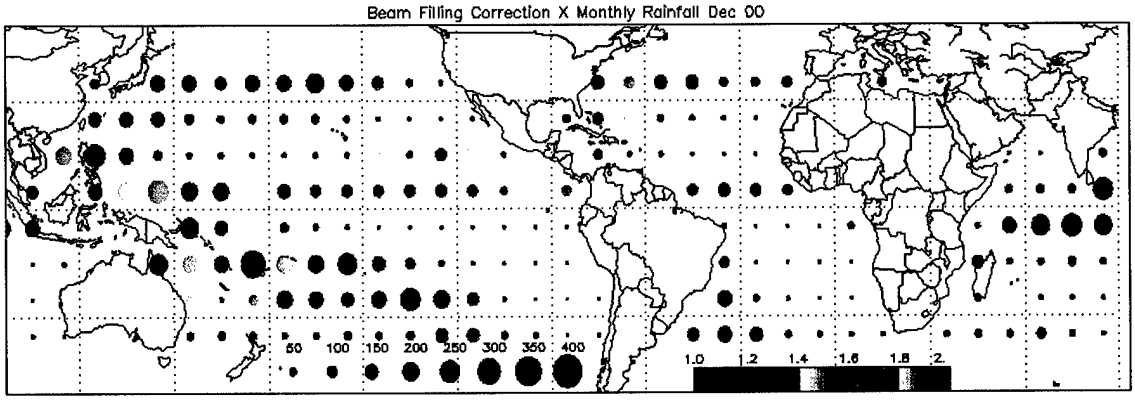

Figure A.36: December 2000 beam-filling correction (color) and total rainfall in mm (circle size).

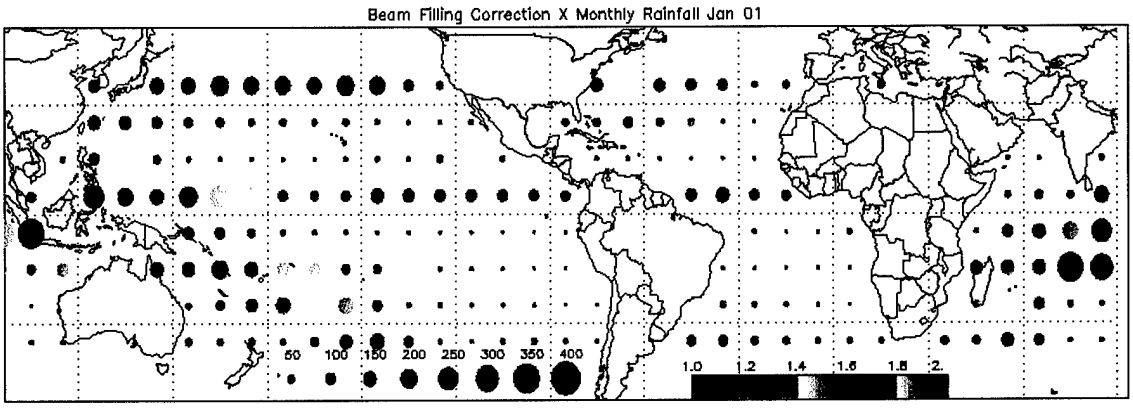

Figure A.37: January 2001 beam-filling correction (color) and total rainfall in mm (circle size).

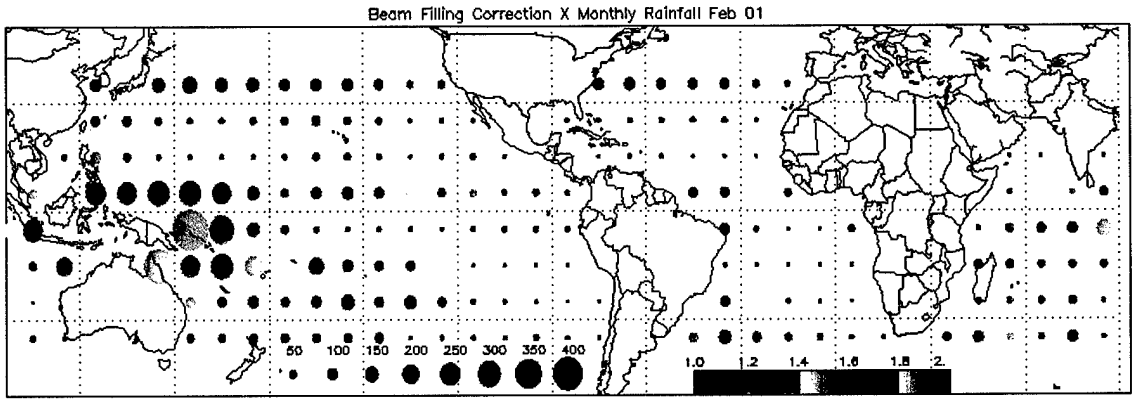

Figure A.38: February 2001 beam-filling correction (color) and total rainfall in mm (circle size).

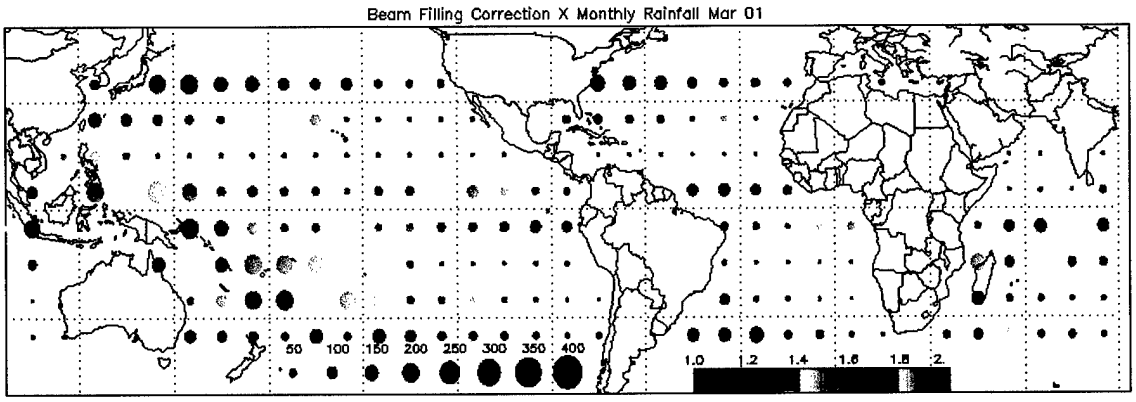

Figure A.39: March 2001 beam-filling correction (color) and total rainfall in mm (circle size).

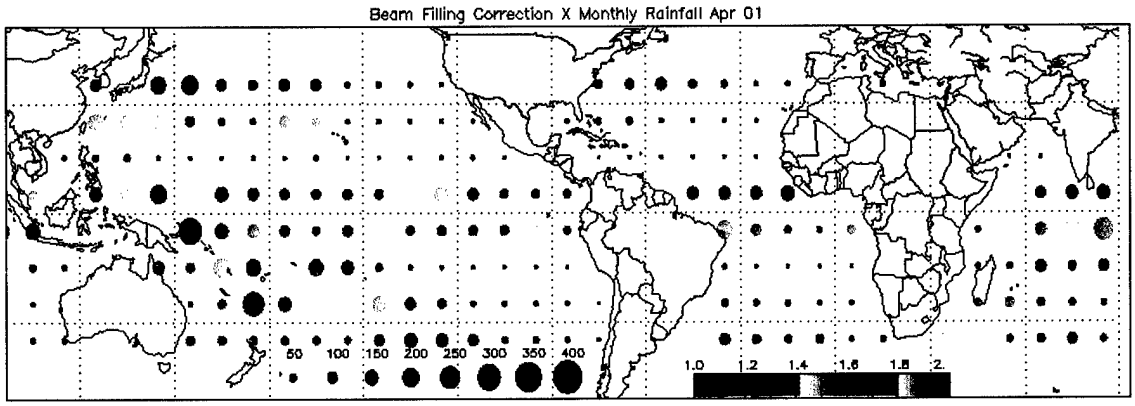

Figure A.40: April 2001 beam-filling correction (color) and total rainfall in mm (circle size).

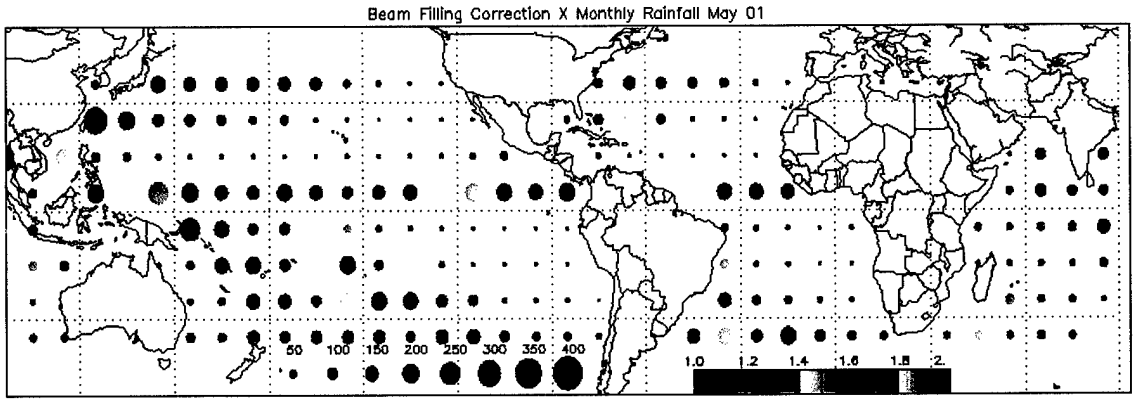

Figure A.41: May 2001 beam-filling correction (color) and total rainfall in mm (circle size).

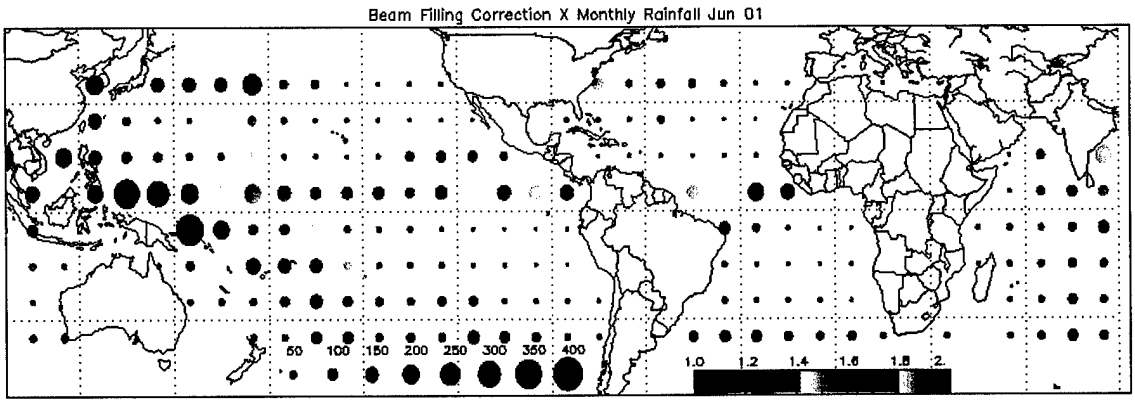

Figure A.42: June 2001 beam-filling correction (color) and total rainfall in mm (circle size).

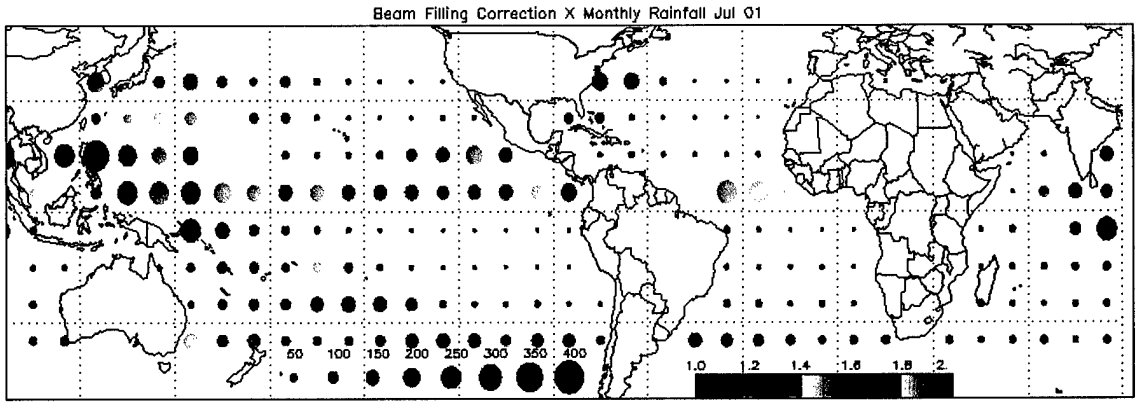

Figure A.43: July 2001 beam-filling correction (color) and total rainfall in mm (circle size).

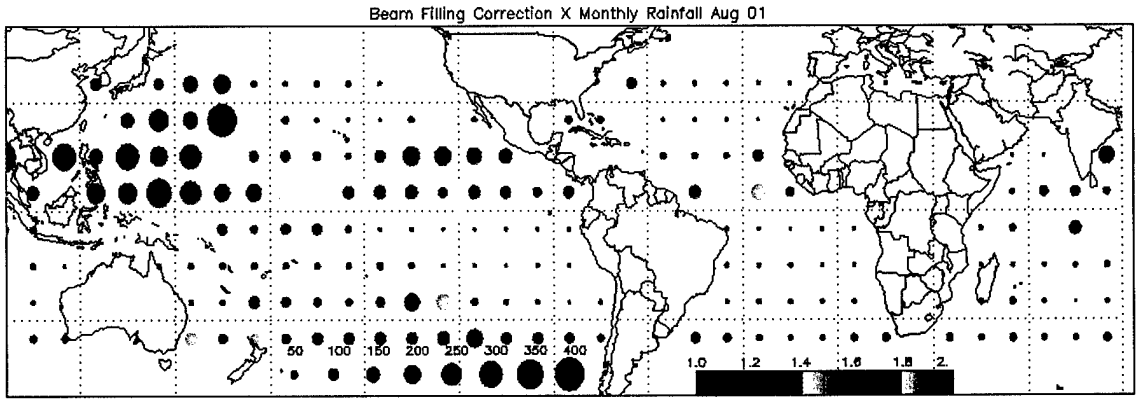

Figure A.44: August 2001 beam-filling correction (color) and total rainfall in mm (circle size).